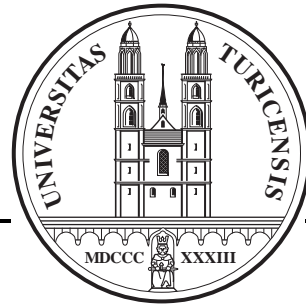




WISSENSCHAFTLICHER JAHRESBERICHT April 2000 - März 2001



PHYSIK-INSTITUT
DER UNIVERSITÄT ZÜRICH



WISSENSCHAFTLICHER JAHRESBERICHT
April 2000 - März 2001

The picture on the cover shows David Lindelöf of the Zürich ATHENA group with the antihydrogen detector

Sekretariat	01 635 5721	secret@physik.unizh.ch
Prof. C. Amsler	01 635 5784 022 767 2914	amsler@cern.ch
Prof. R. Engfer	01 635 5720	engfer@physik.unizh.ch
Prof. H.-W. Fink	01 635 5801	fink@physik.unizh.ch
Prof. H. Keller	01 635 5748	keller@physik.unizh.ch
Prof. P.F. Meier	01 635 4016	meier@physik.unizh.ch
Prof. J. Osterwalder	01 635 5827	osterwal@physik.unizh.ch
Prof. U.D. Straumann	01 635 5768	strauman@physik.unizh.ch
Prof. P. Truöl	01 635 5777	truoel@physik.unizh.ch

Begleitwort

Der Jahresbericht des Physik-Instituts für das Jahr 2000 belegt die reichhaltige Forschungstätigkeit in den beiden Schwerpunktsbereichen Physik der kondensierten Materie und Elementarteilchenphysik. Für einmal verzichte ich darauf besonders bedeutende Ereignisse herauszugreifen. Stattdessen möchte ich die Persönlichkeit und auch die Forschungstätigkeit des im Februar 2001 zurückgetretenen, langjährigen Mitglieds und Direktors des Physik-Instituts *Prof. Dr. Roland Engfer* würdigen.

Ich habe, vor 35 Jahren, an der Scuola di Fisica *Ettore Majorana* in Varenna am Comer See, an die ich als Doktorand geschickt wurde, Roland Engfer das erste Mal zuhören dürfen - muonische Atome waren das Thema seines enthusiastischen Vortrages, etwas was seine Darmstädter Gruppe am Europäischen Kernforschungszentrum CERN in Genf gerade untersuchte. Muonische Atome sind eine exotische Spezies von Atomen, bei denen ein negativ geladenes Muon mit dem Kern ein wasserstoffähnliches System bildet. Die Spektroskopie solcher Atome lehrt uns, wie im Atomkern Ladungen und magnetische Momente verteilt sind. Den Muonen ist er mit gutem Grund treu geblieben, wie uns die Arbeiten seiner Gruppe in diesem Bericht zeigen.

Neun Jahre später, 1975, nach der Habilitation in Darmstadt, wo sein Lehrer und Mentor Peter Brix tätig war, nach dem Wechsel zum Schweizerischen Institut für Nuklearforschung, dem heutigen Paul-Scherrer Institut, und der Umhabilitation an die ETH wurde Roland Engfer an unsere Universität berufen, als Nachfolger von Hans Staub.

Wir haben ihn seitdem in vielen Rollen kennengelernt - traditionell einem Professor gebührende und auch ungehörliche, und immer gelang es ihm irgendetwas aus der einen Rolle in die andere hinüber zu retten. Einige dieser Rollen sollen erwähnt werden.

Velorennen fuhr der junge Roland - vor wenigen Jahren sogar noch im Aargauer Senioren-Circuit - und dies bescherte ihm ein grosses Herz, medizinisch nicht unbedingt ein Vorteil, ausser man ist als Institutsdirektor für viele zuständig, wie er das während sieben Jahren war. Mit dem Mountainbike demonstrierte er auf Hörsaaltreppen Biomechanik in der grossen Vorlesung. Als Vorsitzender des Betriebsausschuss Universität Zürich Irchel kämpfte er erfolgreich für mehr Veloständer, aber auch, nicht ganz so erfolgreich, gegen Verwaltungswillkür wie weiland sein Namenspatron für mehr Freiheitsrechte unter kaiserlicher Obhut.

Der Bergsteiger Engfer nutzte seine Fertigkeiten und liess sich von der Hörsaaldecke herab abseilen, und redete dabei über Reibung, Energiesatz und Wärmeentwicklung. Das Berlin der Vor- und Nachkriegszeit prägte den jungen Roland, sprachlich und anderweitig, preussisches Umfeld zwar, das an Pflicht gemahnt, aber auch, mit seinem Humor ironische Distanz erlaubt, ein Umfeld aber auch, das ein soziales Gewissen fördert und autoritäres Verhalten meidet, Eigenschaften, die einem Institutsdirektor wohl anstehen.

Wie der Velofahrer Engfer gerne ignorierte, dass Ampeln auch einmal auf rot geschaltet sein können, widmete der Experimentator Engfer der Frage, ist Verbotenes wirklich verboten, oder anders ausgedrückt, ist Null wirklich null. Hier komme ich auf das Muon zurück. Es ist eine nützliche Erfahrung der Teilchenphysik, dass die Zahl der zur Muonfamilie gehörenden Leptonen und die Zahl der zur Elektronfamilie gehörenden Leptonen in einer Reaktion erhalten sind. Diese Erfahrung ist theoretisch nicht begründbar. Als Engfer in Zürich begann, wusste man, dass wenn ein Muon in zwei Elektronen und ein Positron zerfällt, etwas was also nach dem obigen Satz verboten ist, dies höchstens mit einer Wahrscheinlichkeit von 10^{-8} passiert. Heute liegt die Obergrenze dank Engfer bei 10^{-12} . In einen anderen Prozess erreichte Engfer's Gruppe die noch tiefere Grenze 5×10^{-13} . Ich denke, dass wir noch einmal 25 Jahre werden warten müssen, bevor wir eine signifikante Verbesserung dieser Grenzen erleben werden.

Zu seinem 60. Geburtstag haben seine Mitarbeiter Roland Engfer eine Imkerausrüstung geschenkt. Dies ist eine der Rollen, die er wohl nach seinem Rücktritt spielen wird. Eine weitere zeichnete sich im vorletzten Sommer ab. Da erlebten ihn seine Freunde auf einem Berg in der Nähe von München in der Rolle des Hobbyastronomen, des Sonnenfinsterniserhellers. Müssen wir dies als Vorbereitung auf seine neue Rolle als Druide nach der Pensionierung sehen? Ich glaube nicht. Roland Engfer ist jemand, dem die Fähigkeit zum Staunen geblieben ist, etwas was alle guten Physiker jung erhält. Seine Begeisterung für die Astronomie und die Astrophysik hatte auch für unsere Fakultät ihre Konsequenzen. Roland Engfer hat zusammen mit dem Schweizerischen Wissenschaftsrat vor langen Jahren eine Tagung im Engadin organisiert, die die Zukunft der Astrophysik in der Schweiz zum Thema hatte. Mit der absehbaren Berufung eines Astrophysikers in der theoretischen Physik an der Universität und einer komplementären Berufung eines experimentellen Astrophysikers an der ETH werden seine Visionen in Kürze Realität.

Ich denke wir können Roland in Dankbarkeit für seine Zukunft alles Gute wünschen, und hoffen, dass er sein Versprechen, den Kontakt zum Institut zu wahren, nicht vergisst.

Das Institut verlor 2000 altersbedingt zwei langjährige, verdiente Mitarbeiter. Herr *Albert Streuli* war ein sehr geschätztes Mitglied der mechanischen Werkstatt. Unter seinen Händen sind einige bemerkenswerte Detektorbauteile für die Hochenergiephysik entstanden. Ebenfalls die Altersgrenze erreichte der Chef der elektronischen Werkstatt, *Karl Esslinger*, der alle Entwicklungen der Detektor- und Leistungselektronik vom Röhren-, über das Transistorzeitalter bis hin zu den *Surface Mounted Devices* mitgestaltete. Ihm gebührt besonderer Dank, und die von ihm konzipierten Hochfrequenzsysteme werden noch eine Weile in unseren Apparaturen aktiv bleiben. Auch diesen beiden wünschen wir einen gefreuten Ruhestand.

Schliesslich gibt es ein weiteres, für die Forschungsförderung wichtiges Ereignis des Jahres 2000 zu vermelden. Der Entdecker der Hochtemperatur-Supraleitung *Prof. Dr. Dr. hc. mult. K. Alex Müller*, Physik-Nobelpreisträger 1987 und Honorarprofessor der Universität Zürich, hat eine massgebliche Stiftung zur Förderung der Forschung am Physik-Institut errichtet. Die Stiftung will am Physik-Institut arbeitende Forschungsgruppen bei der Anschaffung von Apparaten, bei der Anstellung von Mitarbeitern insbesondere von akademischem Nachwuchs, in der Realisation internationaler Zusammenarbeit und bei der wirtschaftlichen Nutzung von Forschungsergebnissen unterstützen.

Prof. Müller will mit seiner grosszügigen Geste auch verdanken, dass man ihm als jungen in der Industrie arbeitendem Physiker an der Universität Zürich unbürokratisch schnell die Möglichkeit gab zu lehren, Kontakt zur Hochschule und Studierenden zu wahren, und ihm auch jetzt noch, nach Emeritierung die Möglichkeit bietet, sich aktiv an der Forschung zu beteiligen. Die andauernde Präsenz in den Seminarien, der offene Zugang, den Forschende und Studierende jederzeit zu K. Alex Müller für Diskussionen und Ratschläge finden, und seine weitreichenden Kontakte bereichern das intellektuelle Leben im Institut ungemein.

Der Jahresbericht¹ ist in englischer Sprache abgefasst. Dies erleichtert die Kommunikation innerhalb internationalen Kollaborationen, und erlaubt es, Teile dieses Bericht den forschungsfördernden Instanzen und ihren Gutachtern als Rechenschaftsbericht vorzulegen.

Zürich, im April 2001

Prof. Dr. Peter Truöl



¹Der Jahresbericht ist auch über das Internet einsehbar: <http://www.physik.unizh.ch/jb/>

Contents

Physics of Fundamental Interactions and Particles	1
1 Measurement of the Gravitational Constant G	1
2 Measurement of the Neutrino Magnetic Moment at the Bugey Nuclear Reactor	4
3 Search for μ-e Conversion with SINDRUM II	8
4 Rare Kaon Decays	11
5 Meson Spectroscopy at LEAR with the Crystal Barrel	13
5.1 Annihilation at 900 MeV/c	13
5.2 Analysis and results	14
6 Production and Spectroscopy of Antihydrogen	17
6.1 Introduction	17
6.2 Antihydrogen detector	18
6.3 Performance of undoped CsI at low temperature	21
6.4 First results with antiprotons	22
7 Particle Physics at DESY/HERA (H1)	25
7.1 Electron proton collisions at 300 to 320 GeV center of mass energy	25
7.2 Summary of activities	27
7.2.1 Central inner proportional chamber construction	27
7.2.2 CIP Electronics	27
7.3 A new era of tracking at H1	29
7.4 Results from recent analyses	31
7.4.1 Beauty production	31
7.4.2 Update on high Q^2 data	34
8 Particle Physics at DESY/HERA (HERA-B)	38
9 High-precision CP-violation Physics at LHCb	41
9.1 Introduction	41
9.2 CP – Violation in the B Meson system: recent developments	41
9.3 Development of an inner tracking detector for LHCb	42
9.3.1 Triple GEM option	42
9.3.2 Silicon microstrip option	44
9.4 Other collaboration activities	46
9.4.1 Hardware developments	46
9.4.2 Software	46

10 Particle Physics with CMS	48
10.1 Introduction	48
10.2 Test of irradiated pixel sensors	49
10.2.1 Guard ring design	50
10.2.2 Pixel design	50
10.2.3 Oxygenated silicon pixels	51
10.2.4 Beam tests	51
10.3 Tracking at CMS: the combinatorial forward Kalman filter	52
Condensed Matter Physics	55
11 Superconductivity and Magnetism	55
11.1 Introduction	55
11.2 Studies of oxygen isotope effects	55
11.2.1 Oxygen isotope effects in manganites	55
11.2.2 Oxygen isotope effects in cuprates	56
11.3 Thermal and transport studies	61
11.3.1 New developments in instrumentation	61
11.3.2 Electrical transport in doped manganites	62
11.3.3 Phase transition of the vortex lattice in cuprates	63
11.4 Spectroscopic studies of cuprates (not related to isotope effects)	64
11.4.1 NMR and NQR studies	64
11.4.2 μ SR studies of ruthenocuprates	65
11.4.3 EPR studies of cuprates	66
11.5 Experiments with low-energy muons	67
12 Surface Physics	70
12.1 Fermi surfaces of the two-dimensional surface states on vicinal Cu(111)	71
12.2 Surface states and the stability of adsorbate periodicities: O/Mo(110)	72
12.3 Tunneling across hexagonal boron nitride films on Ni(111)	73
12.4 Interface states in a metal-insulator heterojunction	74
12.5 Co intercalation underneath hexagonal boron nitride films on Ni(111)	75
12.6 Status of COPHEE, the COmplete PHotoEmission Experiment	76
12.6.1 Electron optics	77
12.6.2 Data acquisition hard- and software	77
12.7 Near node photo-electron holography	78
12.8 Surface Patterson functions from medium-energy electron diffraction	79
12.9 Construction of an electron gun for time resolved low-energy electron diffraction	79
13 Physics of Biological Systems	82
13.1 Overview	82
13.2 Interfacing bio-molecules to silicon structures	82
13.3 Mechanical manipulation of DNA molecules in the liquid phase	83
13.4 Structural biology of single proteins.	84
13.5 Field-ion microscopy and field-emission studies of single C60 clusters in tungsten tips.	84

14 Computer Assisted Physics	85
14.1 Electronic structure of high- T_c materials	85
14.1.1 Transferred hyperfine fields	85
14.1.2 Influence of dopants on the electronic structure of high- T_c materials .	86
14.1.3 Local distortions in doped La_2CuO_4	88
14.2 Time series analysis of EEG	89
Infrastructure and Publications	91
15 Mechanical Workshop	91
16 Publications	94
16.1 Research group of Prof. C. Amsler	94
16.2 Research group of Prof. R. Engfer	97
16.3 Research group of Prof. H.-W. Fink	97
16.4 Research group of Prof. H. Keller	98
16.5 Research group of Prof. P. F. Meier	103
16.6 Research group of Prof. J. Osterwalder	106
16.7 Research group of Prof. U. Straumann	110
16.8 Research group of Prof. P. Truöl	112

1 Measurement of the Gravitational Constant G

St. Schlamminger and E. Holzschuh

The goal of this experiment is a precision measurement of the gravitational constant G with a projected uncertainty of 10 ppm. The experiment is located at the Paul-Scherrer-Institute (PSI). All major parts are set up and are functioning. Descriptions may be found in previous annual reports or in more detail in the dissertation of F. Nolting [1]. The measurements of G , which he made, demonstrated the potential of the method but the size of his systematic error (200 ppm) also indicated the need for further developments.

During the last year we have made extensive investigations of possible systematic effects. Also solutions had to be found for the necessarily large improvements. Below we will describe what we have achieved so far. Unfortunately, our work at PSI had to be stopped at the end of September. This is because the building at PSI, where the experiment is located, is being reconstructed. We received first information about this plan in July 2000 and the final decision by PSI was made on 16. August. Hence we could do little changing our experimental plans. The reconstruction is still in progress.

The essential components of the experiment are a single-pan beam balance (Mettler Toledo, type AT1006), two test masses and two large field masses. The test masses (1 kg each) are suspended with thin tungsten wires and alternately connected to the balance. The difference of their weights is measured and defined to be the signal. The field masses (two stainless steel vessels, filled with 6.7 tons of mercury) are moved between two positions and their gravitational force on the test masses modulates the signal.

The key measuring device of the experiment is thus the balance, and in fact, the dominant systematic uncertainties of the early measurements of G were related to the balance. Therefore, our work concentrated on understanding and reducing external disturbances, lowering the noise of the balance, and improving the calibration procedure.

The balance's reading is directly affected by variations of temperature or tilt. We have installed highly sensitive tilt meters with a resolution of $0.1 \mu\text{rad}$ or 0.02 arc seconds in two orthogonal directions. Observations made so far indicate a slow drift (of order $10 \mu\text{rad}$ per week) and a day-night modulation with a typical amplitude of $2 \mu\text{rad}$. It seems that at least the periodic change of the tilt is induced by changes of the ambient temperature. To first order a change of tilt shifts the zero point of the balance which if cancelled by taking differences. We foresee no problems here.

The temperature of the balance is of prime importance. In last year's report we have described the design of an elaborate stabilisation system. After some minor modifications

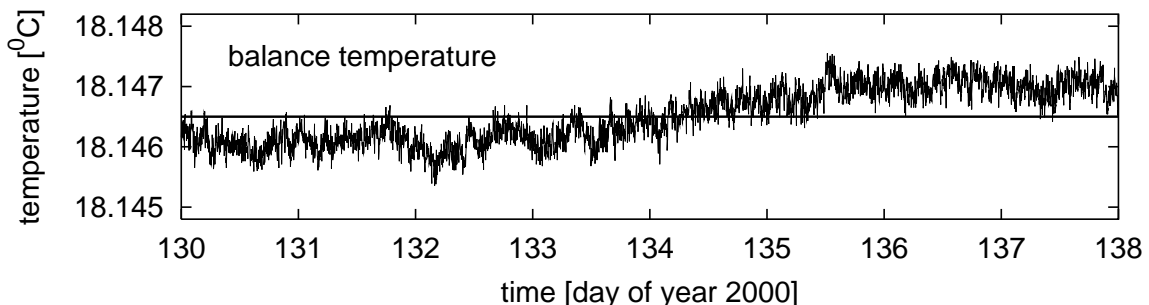


Figure 1.1: *Temperature of the balance during an eight day period in 2000.*

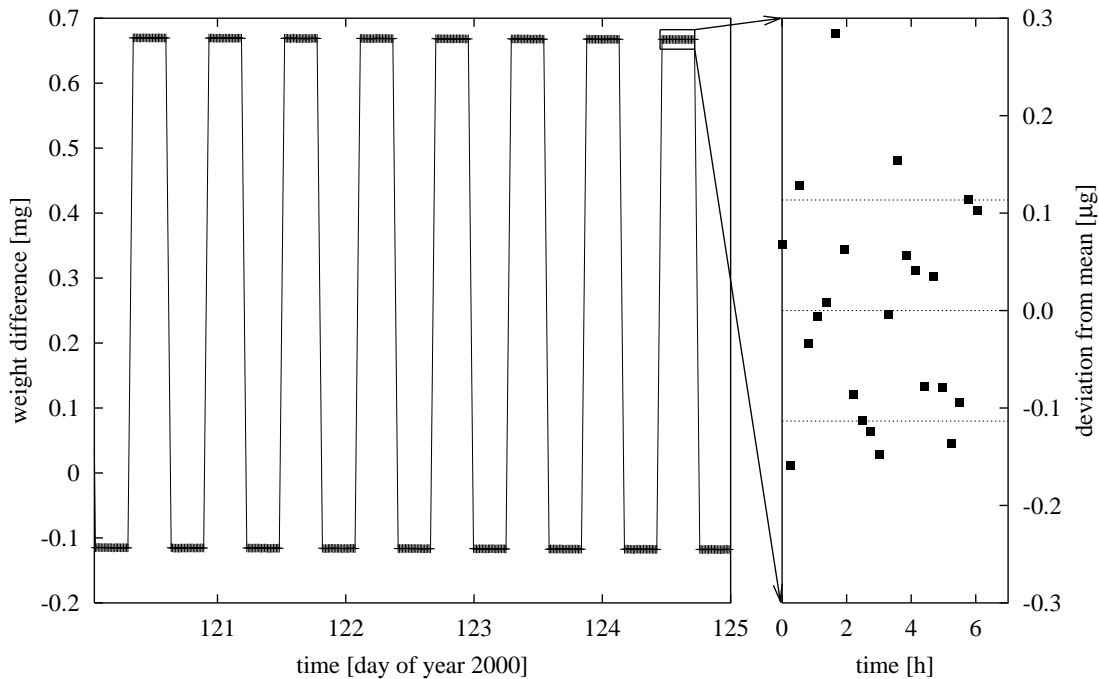


Figure 1.2: *Signal (measured weight difference) from five days of data during 2000. The right part shows the last half-cycle expanded by a factor 700.*

the system now works well. On long time scales the balance's temperature can be kept constant to within about one milli-Kelvin while the ambient temperature changes by several degrees. This is illustrated in figure 1.1 showing data from an eight day run in 2000.

The stable temperature allowed us to investigate the properties of the balance more closely as it was possible before. We found that the zero-point has a linear drift with a slope of $12 \mu\text{g}$ per day. The cause of the drift could not yet be identified. It may have its origin either in the mechanics or the electronics of the balance. A linear drift of the zero-point is of course no problem as it cancels precisely for the weight difference. The calibration of the balance also has a linear drift, with a slope of order $0.1 \mu\text{g}$ per gramme and per day. This should also be no problem as the balance can be re-calibrated several times a day.

We have made measurements to investigate and improve the noise of the balance. An example is given in figure 1.2 showing the measured signal (weight difference of the test masses) as a function of time. The signal is modulated by the gravitational force of the field masses. The root mean square deviation is 110 ng . This is sufficient. A further reduction of the required total measuring time is however still possible as the time for one data point in figure 1.2 was dominated by the time needed to exchange the test masses. With some modifications of the exchange mechanics and a new procedure we hope to achieve a reduction by a factor of about three. This work is in progress.

The balance must be calibrated with standard weights. Conversion to force is done using the value of local gravity (g) which we know to eight decimal places. For the required accuracy (5 ppm), a standard weight must be at least 0.2 g which is much larger than the signal amplitude ($785 \mu\text{g}$). If the response of the balance should not be strictly linear, a serious systematic error may result. We found a simple solution for this problem. It is based on the fact that we need only relate the average slope of the balance's response as determined by a standard weight with the average slope over the signal amplitude. This can be accomplished

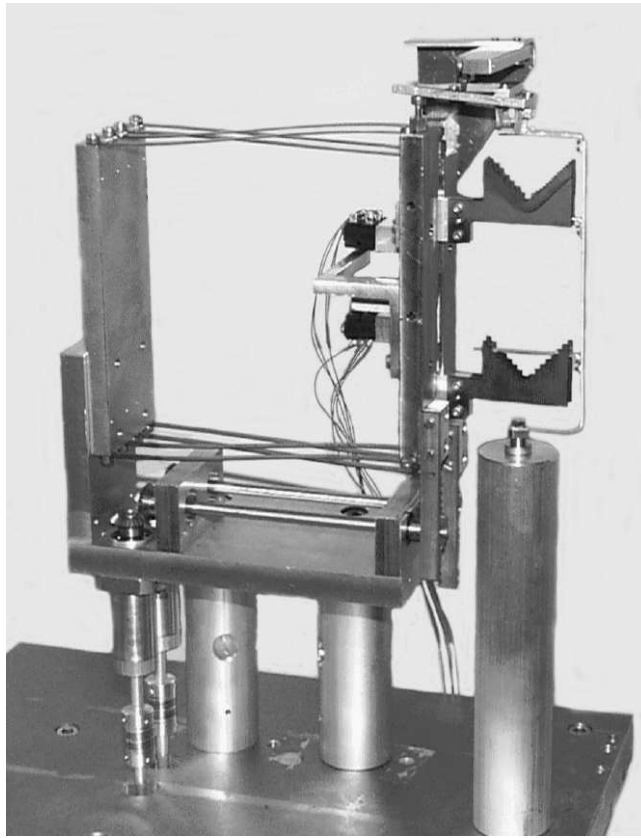


Figure 1.3: *The calibration device, mounted on a test stand.*

by placing a large number of small auxiliary weights on balance and forming an average over the range of the calibration. A device for doing so, in vacuum and under computer control, has been built. A photograph is shown in figure 1.3. The auxiliary weights were made from stainless steel wire and form two sets with 16 pieces each. The masses in one set have nominal values equal to the signal amplitude ($785 \mu\text{g}$) while the masses of the other set are 16 times larger. All pieces have been adjusted such that the deviations from the nominal values do not exceed $3 \mu\text{g}$. By combination we can thus change the auxiliary mass on the balance in 256 approximately equal steps. The auxiliary masses will initially rest on the two V-shaped supports seen on the right in figure 1.3. The supports can be moved in the vertical direction using stepper motors, thereby placing the auxiliary masses in a small frame which will be mounted on the balance's beam.

Initially there were some problems due to adhesive forces, but now the device seems to work well and will be built into the experiment shortly. Provided, the reconstruction at PSI will be finished in due time, we should be able to restart our measurements in the near future.

We thank the PSI for its hospitality and Mettler Toledo for the high precision balance and the calibration of various weights. We are grateful to metrotec engineering for close collaboration. The experiment was supported by the Swiss National Science Foundation, the Dr. Tomalla Foundation, and the Scientific Research Foundation of the University of Zürich.

References

- [1] F. Nolting, Dissertation, Uni. Zürich 1998.

2 Measurement of the Neutrino Magnetic Moment at the Bugey Nuclear Reactor

C. Amsler, O. Link and H. Pruis

in collaboration with:

Institut des Sciences Nucléaires (Grenoble), Université de Neuchâtel, Università di Padova

(MUNU Collaboration)

The aim of the MUNU experiment is to measure the magnetic moment of the electron neutrino. In the standard model the neutrino acquires a magnetic moment proportional to its mass. With the present upper limit on the mass of the electron neutrino the magnetic moment is of the order of $10^{-18} \mu_B$. An experimental upper limit of $1.9 \times 10^{-10} \mu_B$ (95% confidence level) was reported from a reactor experiment [1]. The Superkamiokande experiment obtained an upper limit of $1.5 \times 10^{-10} \mu_B$ (90% confidence level) after 823 days of running [2]. Astrophysical upper limits, e.g. from SN1997A, are two orders of magnitude lower, but with the restriction that neutrinos are Dirac particles.

The experimental evidence for a large magnetic moment would mean new physics beyond the standard model. Extensions of the standard model, e.g. left-right symmetric models, predict that the neutrino should have a large magnetic moment. With a finite magnetic moment the spin of a left-handed neutrino may flip due to the electromagnetic interaction, and become a “sterile” right-handed state which does not interact, and hence is experimentally invisible. The precession of the magnetic moment offers an alternative explanation to the more fashionable MSW effect for the deficit of solar neutrinos: taking the uncertainties in the strength of the magnetic field inside the sun into account, one estimates that a magnetic moment in the range $\mu_\nu = 10^{-10} - 10^{-12} \mu_B$ may explain the observed solar neutrino deficit.

The MUNU experiment actually measures the magnetic moment of anti-neutrinos $\bar{\nu}_e$ from a nuclear reactor, using the elastic scattering reaction $\bar{\nu}_e e^- \rightarrow \bar{\nu}_e e^-$. This process is very sensitive to the magnetic moment of the $\bar{\nu}_e$, because it is a pure leptonic and theoretically well understood weak process. The weak cross-section increases linearly with neutrino energy, but the electromagnetic contribution of the finite magnetic moment increases logarithmically. It is therefore advantageous to measure μ_ν at low neutrino energies, e.g. with neutrinos from a nuclear reactor. MUNU uses a time projection chamber (TPC) which offers two advantages: (i) we measure both the angle and the energy of the recoil electron - and hence can calculate the neutrino energy -, (ii) we measure simultaneously the signal and the background, since electrons cannot be scattered in the backward hemisphere. A finite neutrino magnetic moment leads to an excess of low energy electrons scattered at large angles (near 90°), where the energy becomes very small. The MUNU experiment detects scattered electrons with a low energy threshold of 300 keV.

The TPC (gaseous CF_4 at 3 bar) is located in a stainless steel tank, filled with liquid scintillator to guard against cosmic muons and Compton scattering of low energy γ 's. The photomultipliers of the anti-Compton scintillator operate at the level of one photo-electron. The detection efficiency is 97% for γ energies above 100 keV. It also reduces the cosmic muon rate of 65 Hz to 0.1 Hz. A detailed description of the apparatus can be found in ref. [3] and in previous annual reports.

In 1999 we replaced the oxisorb filters purifying the TPC gas by smaller, low background ones. Activity measurements confirmed that zeolites in the oxisorb contained much higher quantities of uranium than foreseen. The counting rate of electrons with energies higher than 300 keV in the TPC then dropped by a factor of 100, from 10 Hz to 0.1 Hz. For the α 's

from the gas, the counting rate dropped by a factor 10^5 , from 35 to 5×10^{-3} Hz. However, the counting rate from α 's emerging from the cathode side remained constant, at about 0.05 Hz. This background was traced to the presence of ^{214}Bi (from the decay chain of radon) implanted on the high voltage cathode surface. This nuclide decays into stable ^{206}Pb through a chain of delayed α and β emission which generates background electrons in the TPC.

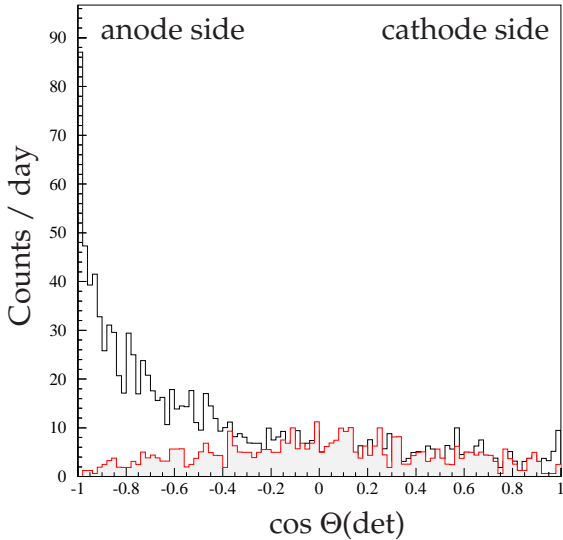


Figure 2.1: *Angular distribution of background electrons during a reactor off period. The angle $\theta(\text{det})$ is measured with respect to the z-axis of the TPC. The open histogram refers to 300 keV threshold, the shaded histogram to 700 keV.*

The high voltage cathode was replaced during a 3 months period in summer 2000. After replacement the α counting rate associated with the cathode dropped by a factor 10^2 , to an acceptable 5×10^{-4} Hz. The angular distribution of background electrons during a reactor off period and after the replacement of the cathode is shown in Fig. 2.1. There is no electron excess from the cathode side, but the number of electrons from the anode side remains unpleasantly high. Above 700 keV (shaded histogram) the background distribution is fairly flat. We do not have any explanation so far for the observed excess of low energy electrons.

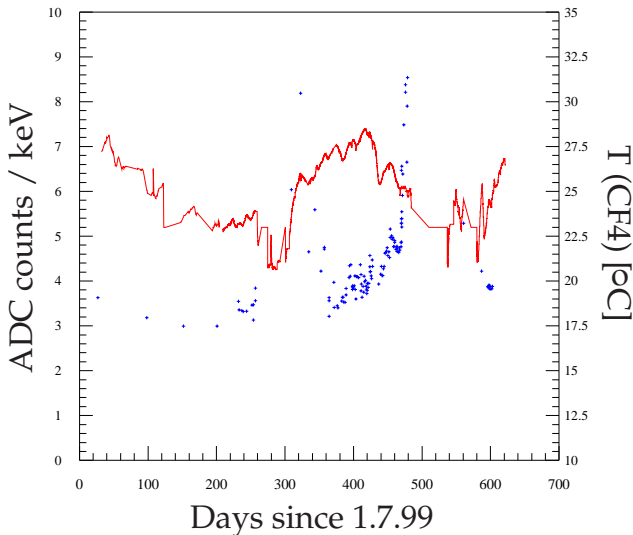


Figure 2.2: *TPC gain (dots) and temperature (curve) as a function of time. The cathode was replaced on day 300.*

Unfortunately a new problem arose from a leak in the acrylic structure of the TPC. After replacing the cathode we filtered a few ml of liquid scintillator every week from the gas cool trap. The contamination of the TPC gas with scintillator vapour led to strong fluctuations

in the anode signal gain. The gain is shown in Fig. 2.2 as a function of time (the TPC was calibrated with cosmic muons and a Mn source). Strong fluctuations are observed around days 400-480, when a leak from the anti-Compton shield was discovered.

Then in autumn 2000 an anode wire broke, inducing a short circuit with the neighbouring readout plane. The anode was probably damaged because of the strong amplification at day 480 (see Fig. 2.2). The detector was opened and the damaged anode repaired. Actually, we exchanged the complete anode plane to avoid the risk of breaking further wires. The work was completed in February 2001 and the detector again operated routinely at a CF_4 pressure of 3 bar. The TPC high voltage is -37 kV (grid potential - 2000 V) and the maximum drift time of $63 \mu\text{s}$ corresponds to a drift velocity of $2.5 \text{ cm}/\mu\text{s}$. Figure 2.3 shows the improvement in the data collection efficiency in 1999 and 2000.

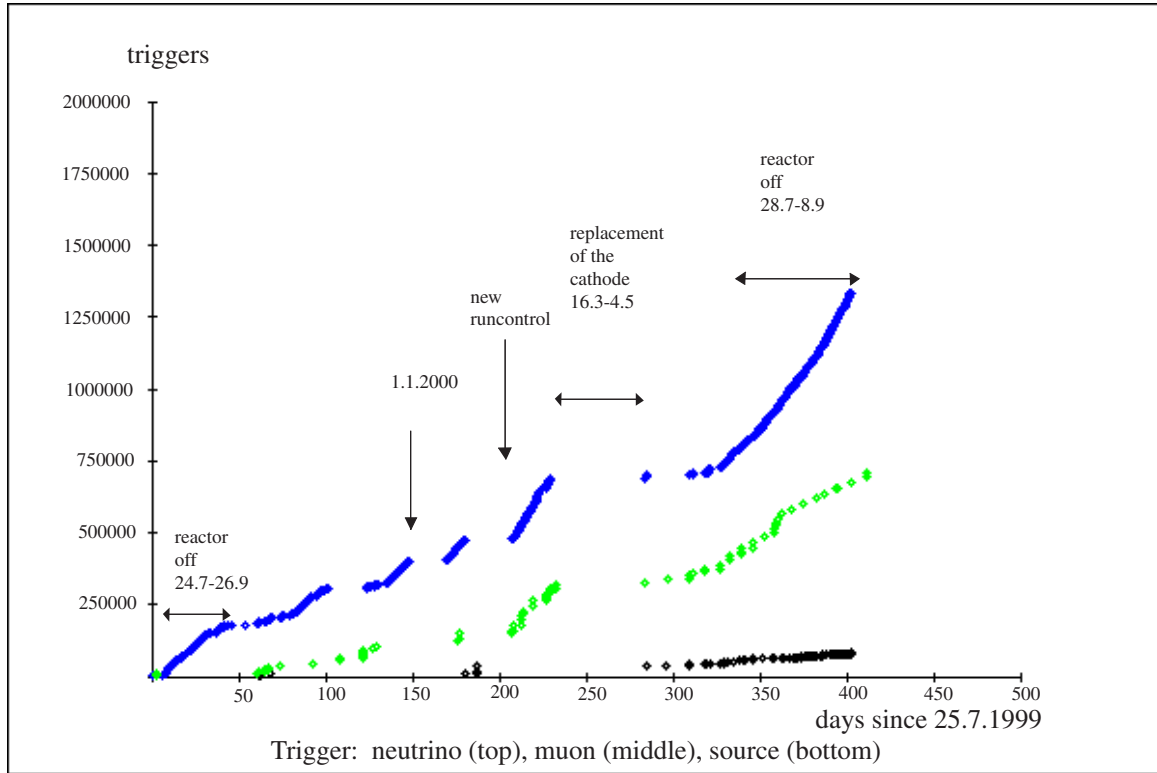


Figure 2.3: *Triggers accumulated during the last 400 days.*

The background was studied in a 2 months reactor shutdown in summer 2000, within which we collected 319,000 background events. The typical rate reductions by the online trigger and off-line analyses are as follows: without filtering the counting rate of the TPC is about 65 Hz, mainly due to cosmic muons which are still numerous below the reactor after 20 m of water equivalent. The counting rate drops to 0.15 Hz after the muon and the anti-Compton veto. With an energy threshold of 300 keV the counting rate from background electrons is 14 mHz, using a fiducial volume cut applied to reduce β -radioactivity from the walls of the TPC.

Electron events with no associated low energy photon converted in the anti-Compton are then scanned by eye. The angular distribution is shown in Fig. 2.4 as a function of recoil angle θ . This distribution is not corrected for acceptance and efficiency. The shaded region around $\cos \theta = 1$ is the region in which neutrino-electron scattering events would be expected during a reactor on run. The shaded events were obtained by requiring the measured electron angle

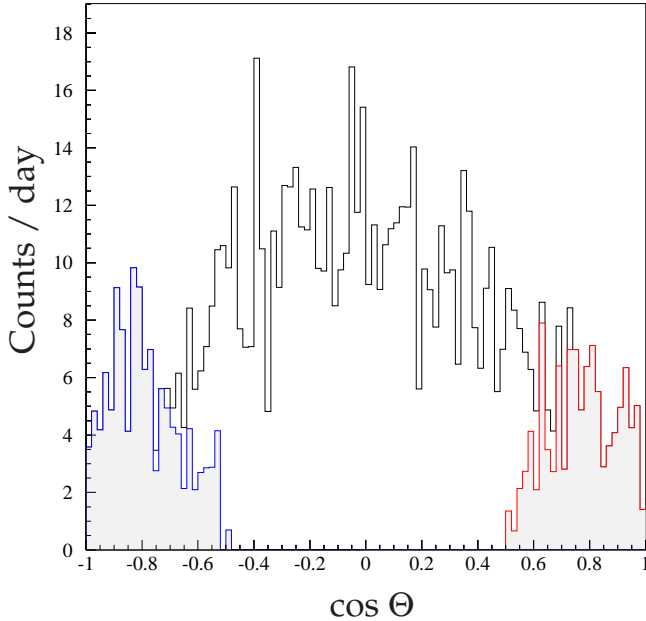


Figure 2.4: *Angular distribution of background electrons during a reactor off period. The angle $\theta = 0$ corresponds to electrons emitted in the direction opposite to the reactor core. The shaded histogram contains events with the kinematical condition that $E_\nu > 0$ (see text). The energy threshold for the electron was 300 keV.*

and energy to be consistent with a positive neutrino energy, pretending that these events were induced by neutrinos from the reactor ($\theta = 0$) or from the direction opposite to the reactor ($\theta = 180^\circ$).

We have so far scanned 10% of the reactor off period, corresponding to a 57 hours dead-time corrected run. In the forward direction one finds 106.9 ± 6.6 , in the backward direction 120.2 ± 7.0 electrons/day. The excess of backward events is visible in Fig. 2.4. The background seems to be anisotropic, larger in the backward direction, but more statistics and acceptance corrections are needed.

During summer 2000 we also collected 243,000 events with reactor on, of which about 11% were analyzed so far (corresponding to a 62 hours run). One finds 113.2 ± 5.7 events/day in the forward direction and 109.3 ± 5.6 events / day in the backward direction. The latter agrees with reactor off. Larger statistics samples are of course needed. From Monte Carlo simulations one expects 8.8 neutrino-electron events/day at 3 bar, with a threshold of 300 keV and assuming $\mu_\nu = 0$. The counting rate increases to 13.1 events / day with a finite magnetic moment of $\mu_\nu = 1.0 \times 10^{-10} \mu_B$. Our background over signal ratio is therefore about 10:1. Note that in ref. [1] the upper limit on the neutrino magnetic moment was derived with a much worse background over signal ratio of 100:1.

The analysis of the data collected after the replacement of the high voltage cathode is very promising as the contaminating background was decreased by a factor of 100. During the year 2001 we hope to collect neutrino data for 200 days after which we could reach an upper limit for μ_ν of a few $10^{-11} \mu_B$. Data taking for this experiment should be completed by the end of 2001.

References

- [1] A. I. Derbin et al., JETP Lett. 57 (1993) 768
- [2] J.F. Beacom and P. Vogel, Phys. Rev. Lett. 83 (1999) 5222
- [3] C. Amsler et al., Nucl. Instr. Meth. in Phys. Res. A 396 (1997) 115

3 Search for μ -e Conversion with SINDRUM II

R. Engfer, E.A. Hermes, T. Kozłowski, G. Kurz, F. Rosenbaum,
A. van der Schaaf, P. Wintz, I. Zychor

in collaboration with:

III. Phys. Institut der RWTH Aachen and PSI Villigen

SINDRUM II

Observations on solar and atmospheric neutrinos indicate that neutrinos mix so lepton flavor would not be conserved. SINDRUM II tests lepton-flavor conservation by a search for μ e conversion in muonic atoms. The process would result in electrons at fixed momentum (depending on atomic number) around 100 MeV/c.

In recent years a dedicated beamline was brought into operation in the π E5 area at PSI. The major element is a 9 m long superconducting magnet. In spring 2000, after a long series of modifications, reliable operation of this PMC magnet was obtained. In the following months data were taken on gold. Conversion on a heavy nucleus might be enhanced relative to a medium Z target, such as titanium [1].

See Fig. 3.1 and Fig. 3.2 for a description of the experimental setup.

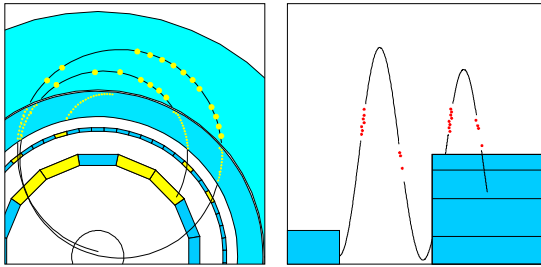


Figure 3.1: *Traces left by a 100 MeV/c electron. The particle made two full turns before reaching an endcap detector. Fits to the particle trajectory are indicated.*

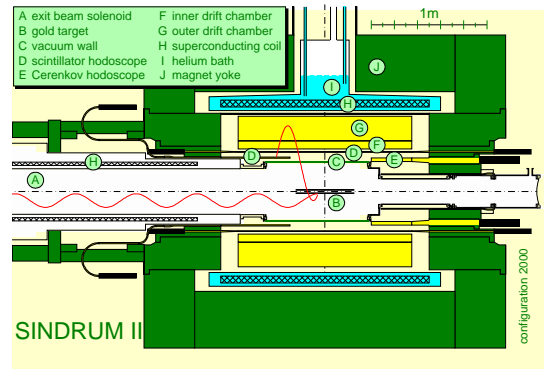


Figure 3.2: *The SINDRUM II spectrometer during the year 2000 measurements. Muons are transported to the gold target with the help of a 9 m long superconducting solenoid coupled directly to the spectrometer magnet.*

Radiative pion capture (RPC), followed by e^+e^- pair production, can be a major source of background. A pion reaching the gold target has a chance of order 10^{-5} to produce an electron in the energy region of interest, so the pion stop rate must be below one every ten minutes. At the PMC entrance the beam contains similar amounts of muons and pions. Since the pion range in matter is about half as large as the corresponding muon range the pion contamination can be reduced strongly with the help of a moderator at the PMC entrance. Only one out of 10^6 pions may cross this moderator. Typically 99.9% of them would decay before reaching the target. The requirement puts strong constraints on the high-momentum tail transported by the beam line which could be met after a careful optimization of the beam settings. Figure 3.3 shows muon range distributions before and after the optimization procedures. The dramatic reduction of the tails in the range distribution was achieved at the cost of $\approx 30\%$ loss in beam intensity.

The target (see Fig. 3.4) was produced in a galvanic process to ensure the high purity required to suppress background from μ decay in orbit in low- and medium-Z contaminations.

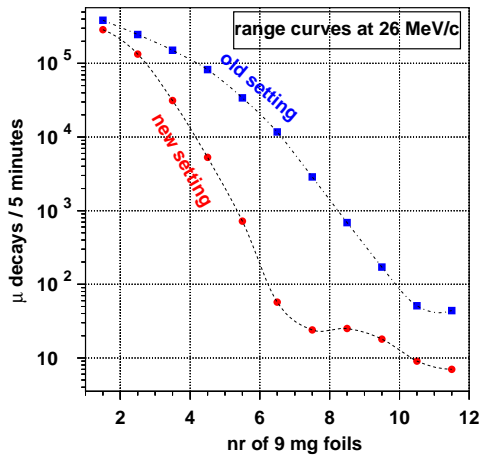


Figure 3.3: Muon range curves at 26 MeV/c nominal beam momentum. Stopped muons were monitored through their decay electrons. Note a dramatic improvement in the slope obtained with the new beam setting.

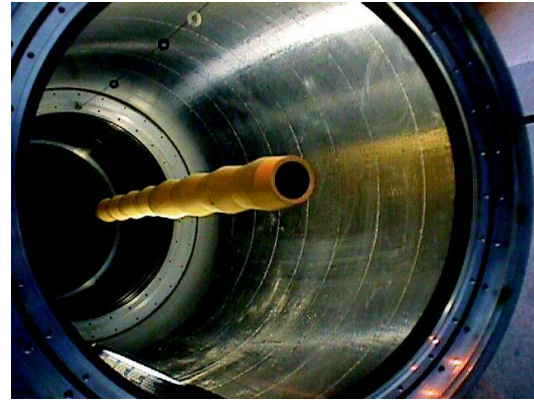


Figure 3.4: The hollow gold target (wall thickness 30 microns only).

Due to the lower muon binding energy such background reaches beyond the energy of the hypothetical μe conversion electrons in gold (95.6 MeV).

During an effective measuring period of 75 days about 4×10^{13} muons stopped in the gold target. Figure 3.5 shows as a preliminary result various momentum distributions. The main spectrum, taken at 53 MeV/c, shows the steeply falling distribution expected from muon

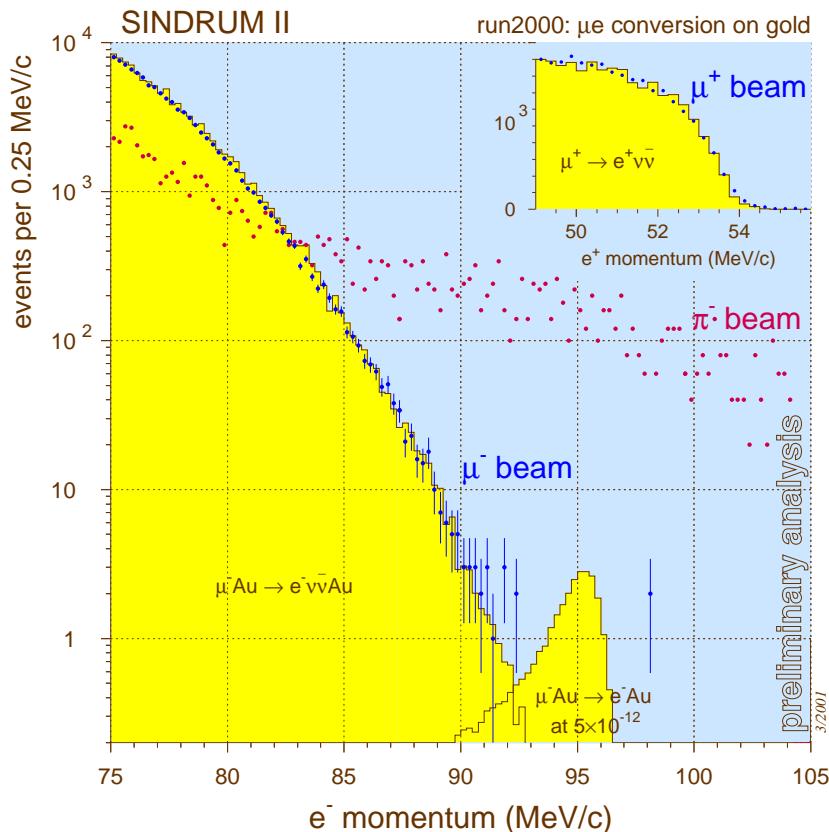


Figure 3.5: Momentum distributions for three different beam momenta and polarities:

- (i) 53 MeV/c negative, optimized for μ^- stops
- (ii) 63 MeV/c negative, optimized for π^- stops
- (iii) 48 MeV/c positive, for μ^+ stops.

The 63 MeV/c data were scaled to the different measuring times. The μ^+ data were taken at reduced spectrometer field.

decay in orbit. Two events were found at higher momenta, but just outside the region of interest. The agreement between measured and simulated positron distributions from μ^+ decay gives us confidence in the momentum calibration. At present we have no hints about the nature of the two high-momentum events: they might be induced by cosmic rays or RPC, for example. Both processes result in flat momentum distributions such as shown by the data taken at 63 MeV/c (see Fig.3.5).

Presently we are still studying the various rates and efficiencies that enter the calculation of the new limit on the branching ratio. As a preliminary result we obtain a single-event sensitivity slightly below 2×10^{-13} which corresponds to a 90% C.L. upper limit below 5×10^{-13} . This constitutes an improvement by two orders of magnitude of the previous best result on a heavy target [2].

References

- [1] T.S. Kosmas, Z. Ren and A. Faessler, Nucl.Phys. **A665** (2000) 183, and references therein.
- [2] SINDRUM II Collaboration, W. Honecker *et al.*, Phys.Rev.Lett. **76** (1996), 200.

4 Rare Kaon Decays

A. Sher and P. Truöl

in collaboration with:

J. Egger, W. D. Herold, H. Kaspar, and H. Weyer, Paul-Scherrer-Institut, CH-5234 Villigen
 Brookhaven National Laboratory, Upton, NY-11973, USA, University of New Mexico, Albuquerque, NM-87131, USA, University of Pittsburgh, Pittsburgh, PA-15260, USA, Yale University, New Haven, CT-06511, USA, Institute for Nuclear Research, Academy of Sciences, 117 312 Moscow, Russia

Experiment E-865 at Brookhaven AGS

Experiment E865 at the Brookhaven AGS [1] was set up primarily to search for the lepton flavor violating decay $K^+ \rightarrow \pi^+ \mu^+ e^-$ ($K_{\pi\mu e}$) [2] with more than an order of magnitude increased sensitivity. The flexibility of the apparatus allowed also to obtain high statistics event samples on the following final states, where existing data were scarce:

$$\begin{aligned} & \pi^+ e^+ e^- (K_{\pi ee}) [3] \\ & \pi^+ \mu^+ \mu^- (K_{\pi\mu\mu}) [4] \\ & \pi^+ \pi^- e^+ \nu_e (K_{e4}) \\ & \mu^+ e^+ e^- \nu_\mu, e^+ e^+ e^- \nu_e (K_{\ell\nu\gamma^*}) \end{aligned}$$

From the $K_{\pi\mu\mu}$ and the K_{e4} samples we have also extracted considerably reduced upper limits for other lepton flavor violating modes like $\pi^+ e^+ \mu^-$, $\pi^- \mu^+ e^+$, $\pi^- \mu^+ \mu^+$, and $\pi^- e^+ e^+$ [5].

The analysis of the $K_{\ell\nu\gamma^*}$ data is still in progress. Preliminary results indicate, that we will be able to determine for the first time separately the electroweak vector and axialvector kaon formfactors F_V and F_A , while previous experiments [6] with real photons in the final state were sensitive to $|F_A + F_V|$ only.

Though considerable progress in the reduction of the immense amount of data has been made last year (Thesis A. Sher, University of Zürich), the analysis of the final $K_{\pi\mu e}$ data set taken in 1998 has not been completed yet. We expect however to improve the sensitivity by at least a factor of three beyond our published limit of 2.8×10^{-11} [2].

The analysis of the K_{e4} data, performed by S. Pislak, has been completed and lead to the new, quite precise value for the s -wave $\pi\pi$ scattering length [7]:

$$a_0^0 = 0.228 \pm 0.012 \text{ (stat.)} \pm 0.003 \text{ (syst.)},$$

which agrees well with the latest prediction from chiral perturbation theory (ChPT) [9]:

$$a_0^0 = 0.220 \pm 0.005 .$$

Figure 4.1 shows the phase shift difference $\delta_0^0 - \delta_1^1$ as a function of the $\pi^+ \pi^-$ invariant mass extracted from our data in comparison to those from an older experiment [8] with twelve times less statistics, which measured $a_0^0 = 0.26 \pm 0.05$. Aside from the scattering length we have extracted the momentum transfer dependence of the axialvector and vector decay form factors, which are an essential ingredient for the determination of the coefficients of the ChPT Hamiltonian to order $\mathcal{O}(p^4)$ [10]. A recent theoretical calculation by Colangelo *et al.* [12] already made use of our data, and of higher energy $\pi\pi$ scattering data to constrain the isotensor $\pi\pi$ -channel through a reanalysis of the Roy equation [11]. The goal was to determine the size of the quark condensate $\langle 0|\bar{u}u|0 \rangle$, which enters the Gell-Mann, Oakes and Renner (GOR) formula:

$$M_\pi^2 \approx (m_u + m_d) |\langle 0|\bar{u}u|0 \rangle| / F_\pi^2 .$$

The new precise value for the scattering length limits the range of possible values for the quantity ℓ_3 , which is one of the coupling constants occurring in the effective chiral Lagrangian at order p^4 . It relates the quantities in the GOR-expression, and confirms it nicely.

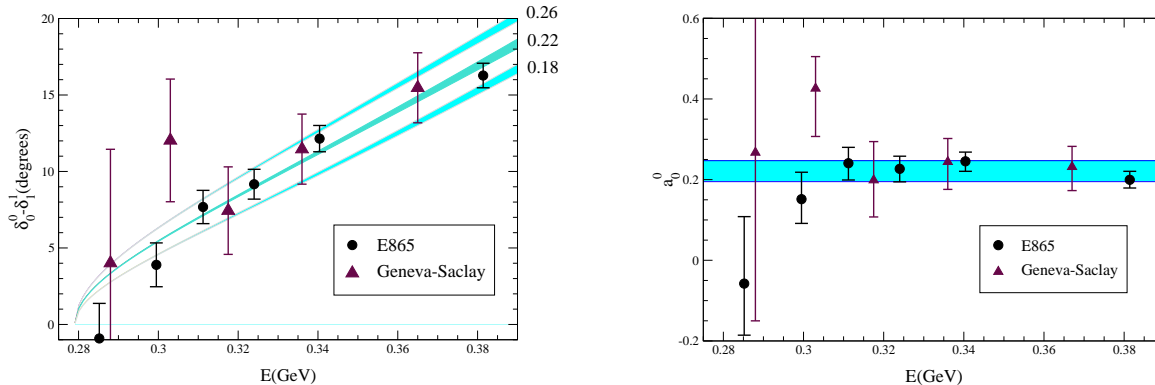


Figure 4.1: *Left: Phase shift difference $\delta_0^0 - \delta_1^1$ as a function of the $\pi^+\pi^-$ invariant mass. The curves show calculations [11] for three values of the S-wave scattering length a_0^0 . The uncertainty band comes from experimental input at higher energies used in the Roy equations. Right: each phase shift value has been converted into a value for the scattering length. The horizontal band indicates the statistical average. Figures taken from [12]. (Geneva-Saclay: ref. [8]).*

References

- [1] R. Appel *et al.*, submitted to Nucl. Instr. & Meth. (Jan. 2001).
- [2] R. Appel *et al.*, Phys. Rev. Lett. **85** (2000), 2450.
- [3] R. Appel *et al.*, Phys. Rev. Lett. **83** (1999), 4482.
- [4] H. Ma *et al.*, Phys. Rev. Lett. **84** (2000), 2580.
- [5] R. Appel *et al.*, Phys. Rev. Lett. **85** (2000), 2877.
- [6] S. Adler *et al.*, Phys. Rev. Lett. **85** (2000), 2256; S. Heintze *et al.*, Nucl. Phys. **149** (1979), 365.
- [7] S. Pislak *et al.*, to be published; M. Zeller, Proc. Chiral Dynamics 2000, TJNL, Newport News, VA (July 2000); P. Truöl, Proc. Int. Conf. Heavy Quarks at Fixed Target (HQ2K), Rio de Janeiro, Oct. 2000, hep-ex/0012012.
- [8] L. Rosselet *et al.*, Phys. Rev. **D15** (1977), 574.
- [9] G. Colangelo *et al.*, Phys. Lett. **488** (2000), 261.
- [10] G. Amoros *et al.*, Phys. Lett. **B480** (2000), 471; Nucl. Phys **B585** (2000), 293.
- [11] B. Ananthanarayan, G. Colangelo, J. Gasser, and H. Leutwyler, hep-ph/0005297, Phys. Rep. (2001), in print.
- [12] G. Colangelo, J. Gasser, and H. Leutwyler, hep-ph/0103063.

5 Meson Spectroscopy at LEAR with the Crystal Barrel

M. Heinzemann and C. Amsler

in collaboration with:

Academy of Science (Budapest); Universities of Bochum, Bonn, Hamburg, Karlsruhe, München, Paris VI; CERN; Carnegie Mellon University; CRN-Strasbourg); RAL; UC-Berkeley

(CRYSTAL BARREL COLLABORATION).

The Crystal Barrel detector was dismantled at the end of 1996, following the closure of the Low Energy Antiproton Ring. Our activities were completed with the submission of the last two theses [1, 2]. For full details on the results achieved with Crystal Barrel, we refer to previous annual reports and to a review article [3].

5.1 Annihilation at 900 MeV/c

In 2000 we finalized the analysis of $\bar{p}p$ annihilation in flight at 900 MeV/c into three neutral pseudoscalars, $\pi^0\pi^0\pi^0$, $\pi^0\pi^0\eta$ and $\pi^0\eta\eta$, leading to six detected photons [2, 4]. We were motivated by a search for radial excitations of scalar and tensor mesons, and also by the controversy around the quark content of the $f_0(1710)$ [5, 6, 7]. The analysis is based on 17.9 million events which were taken with the all-neutral trigger during the last data taking run of Crystal Barrel at LEAR. The offline analysis required complete reconstructed events with exactly six clusters and no charged tracks.

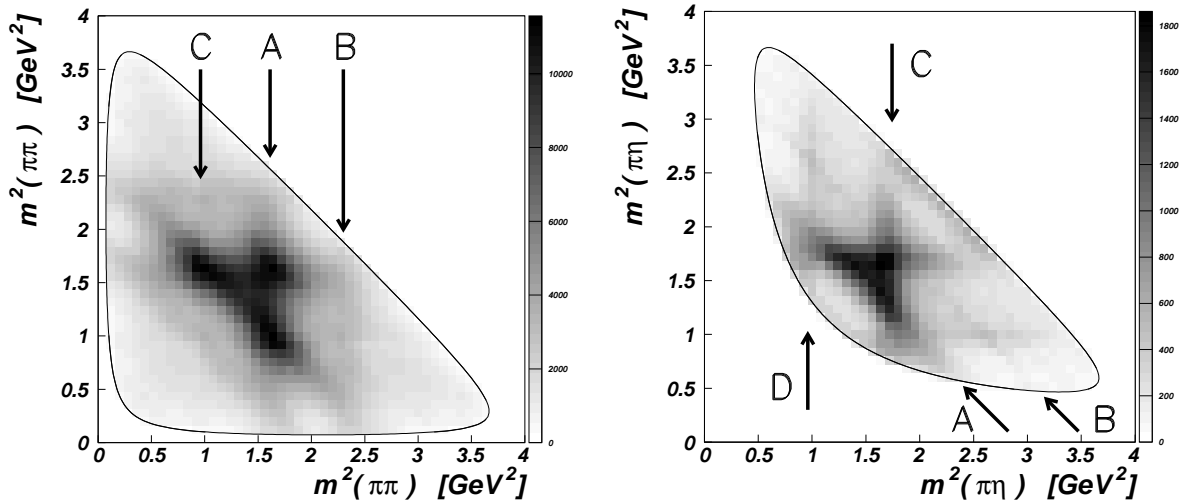


Figure 5.1: *Left: Dalitz plot for $\bar{p}p \rightarrow \pi^0\pi^0\pi^0$ (six entries per event) with $f_2(1270)$ (A), $f_0(1500)$ (B), $f_0(980)$ (C). Right: Dalitz plot for $\bar{p}p \rightarrow \pi^0\pi^0\eta$ (two entries per event) with $f_2(1270)$ (A), $f_0(980)$ (B), $a_2(1320)$ (C) and $a_0(980)$ (D).*

The three annihilation channels were selected by applying kinematic fits requiring also three pairs of 2γ invariant masses to match the π^0 or η masses. For measurements in flight the annihilation vertex of neutral events was not observed and had therefore to be determined by the kinematic fit. The feedthrough from one channel to the other was determined to be less than 0.7 %. The reaction $\bar{p}p \rightarrow \omega\pi^0$ ($\omega \rightarrow \pi^0\gamma$), with a missing γ , was the dominating background channel for $\pi\eta\eta$ and $\pi^0\pi^0\eta$. Background contributions of 13 % and 3 %, respectively, were estimated from the data. This background was simulated and taken into account in the partial wave analysis. The background in the $3\pi^0$ channel was negligible.

We obtained 600,962 $3\pi^0$, 161,158 $\pi^0\pi^0\eta$ and 18,419 $\pi^0\pi^0\eta$ events with a detection and reconstruction efficiency of about 27 %.

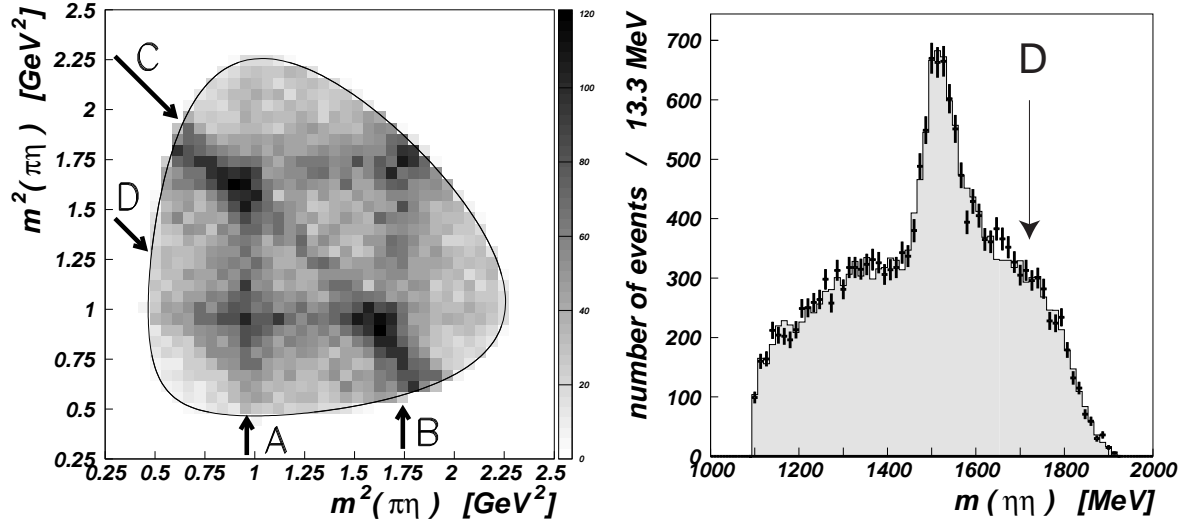


Figure 5.2: Left: Dalitz plot for $\bar{p}p \rightarrow \pi^0\eta\eta$ (two entries per event) with $a_0(980)$ (A), $a_2(1320)$ (B), $f_0(1500)/f_2'(1525)$ (C). The arrow D shows the expected location of the relatively narrow $f_0(1710)$. Right: $\eta\eta$ mass projection showing the $f_0(1500)/f_2'(1525)$. The long tail is due to the new $f_2(1870)$. The shaded histogram is the fit discussed in the text.

The symmetrised $3\pi^0$ Dalitz plot is shown in Fig. 5.1 (left). One observes the $f_2(1270)$ and $f_0(1500)$. A faint dip in the 1500 MeV band around 1000 MeV corresponds to the $f_0(980)$ interfering destructively with the structure at 1500 MeV. Figure 5.1 (right) shows the Dalitz plot for $\pi^0\pi^0\eta$. One observes the $f_2(1270)$, $f_0(980)$, $a_2(1320)$ and $a_0(980)$. The symmetrised $\pi^0\eta\eta$ Dalitz plot and the $\eta\eta$ mass projection are shown in Fig. 5.2. One observes the $a_2(1320)$, $f_0(1500)/f_2'(1525)$ and a band around 1000 MeV from the $a_0(980)$. In the region of the $f_0(1710)$, only the interference of the two $a_0(980)$ bands can be observed and no signal is present (arrow D).

5.2 Analysis and results

An amplitude analysis of the above Dalitz plots (based on the K-matrix formalism) was performed. While annihilation at rest in liquid hydrogen proceeds mainly from S-states ($J=0$ or 1), more initial states are contributing with increasing energies. The $J=4$ contributions to the data sets was found to be less than 5 % and contributions from $J \geq 4$ were therefore neglected. The following initial partial waves were included in the analysis of the present data: 1S_0 , 3P_1 , $^3P_2 + ^3F_2$, 1D_2 , and 3F_3 . Since there are four independent kinematic variables, we performed a maximum likelihood fit. The $\pi\pi$, $\pi\eta$ and $\eta\eta$ S-waves were described with our parameterization from the at rest data [8]. To fit the $3\pi^0$ and $\pi^0\eta\eta$ data sets the program was ported to the NEC SX-5 supercomputer of the Swiss CSCS facility in Manno. A typical fit took about 10 hours.

The description of $\pi^0\pi^0\eta$ requires, apart from the resonances seen directly in Fig. 5.1, a 2^{++} isovector state with mass and width

$$M = 1698 \pm 44 \text{ MeV}, \quad \Gamma = 265 \pm 55 \text{ MeV}, \quad (5.1)$$

in excellent agreement with our result for the $a_2(1660)$ in $\pi^0\eta\eta$ at 1940 MeV/c [9]. This is

the radial excitation of $a_2(1320)$. The L3 collaboration also reports a 2^{++} state in this mass region in $\gamma\gamma$ interactions, decaying into $\pi^+\pi^-\pi^0$ [10].

The description of the $3\pi^0$ data requires, apart from the obvious resonances directly seen in Fig. 5.1, a new broad tensor state with a mass of 1877 ± 30 MeV and a width of 318 ± 55 MeV, decaying into $\pi\pi$, which we call $f_2(1870)$. This state is also required in the analysis of the $\pi^0\eta\eta$ data, where it decays into $\eta\eta$. The $3\pi^0$ and $\pi^0\eta\eta$ data sets were therefore fitted simultaneously with a common description of the resonances. The fit differs only marginally from the ones obtained by the single fits.

The results of the coupled fit for tensor resonances are shown in Table 5.1. The mass and width of the $f_2'(1525)$ agree well with the known values. The $f_2(1565)/AX$, discovered in our earlier ASTERIX experiment [11], is seen here for the first time in annihilation in flight.

Table 5.1: *T-matrix pole parameters of the $\pi\pi$ and $\eta\eta$ D-waves of the coupled fit. The $f_2(1270)$ parameters are fixed.*

	Mass [MeV]	Width [MeV]
$f_2(1270)$	1275	185
$f_2'(1525)$	1508 ± 9	79 ± 8
$f_2(1565)$	1552 ± 13	113 ± 23
$f_2(1870)$	1867 ± 46	385 ± 58

The $f_2(1870)$ is new. The ratio of $\eta\eta$ to $\pi^0\pi^0$ branching fractions is 0.27 ± 0.10 . This ratio is related to SU(3) mixing angles and one gets two solutions for the mixing angle [2], one being compatible with a pure $\bar{u}u + \bar{d}d$ state, hence a radial excitation of the $f_2(1270)$. Then $f_2(1565)$ and $f_2(1870)$ are both radial excitations but do not belong to the same nonet. The other solution leads to a large $\bar{s}s$ component for $f_2(1870)$, in which case $f_2(1565)$, $a_2(1660)$ and $f_2(1870)$ would belong to the same nonet of radially excited 2^{++} $q\bar{q}$ mesons. The ambiguity could be solved by measuring the $f_2(1870)$ decay rates into $\eta\eta$ or $K\bar{K}$.

Figure 5.3 shows the $\pi^0\pi^0$ and $\pi^0\eta$ mass projections for $3\pi^0$ and $\pi^0\pi^0\eta$. The long tails are due to the two new tensor mesons $f_2(1870)$ and $a_2(1660)$.

Table 5.2: *Tentative SU(3) assignment of scalar mesons. The first isoscalar (second column) couples strongly to pions, the second (third column) strongly to kaons. The ‘‘pionic’’ states are very broad, except $f_0(1500)$, which is supernumerary.*

$I = 1$	$I = 0$	$I = 0$	$I = 1/2$	Nature
$a_0(980)$	$f_0(400 - 1200)$ (or σ)	$f_0(980)$	$\kappa(900)$	Scattering resonances
$a_0(1450)$	$f_0(1370)$ $f_0(1500)$	$f_0(1710)$	$K_0^*(1430)$	$1^3P_0(q\bar{q})$
?	$f_0(2020)$	$f_0(2200)$	$K_0^*(1950)$	$2^3P_0(q\bar{q})$

The $\eta\eta$ mass projection for $\pi^0\eta\eta$ is shown in Fig. 5.2 above. The data description is good and there are no significant deviations. The inclusion of an $f_0(1710)$ in either the $\eta\eta$ or the $\pi\pi$ S-wave was not successful. The $f_0(1710)$ is therefore not required to describe the data at 900 MeV/c. This is not surprising if this state is $\bar{s}s$, as the OZI rule forbids the production of $\bar{s}s$ states in $\bar{p}p$ annihilation. Recent results in central production [12] show that, indeed, this state prefers to decay into $K\bar{K}$ rather than into $\pi\pi$ which therefore suggests that this

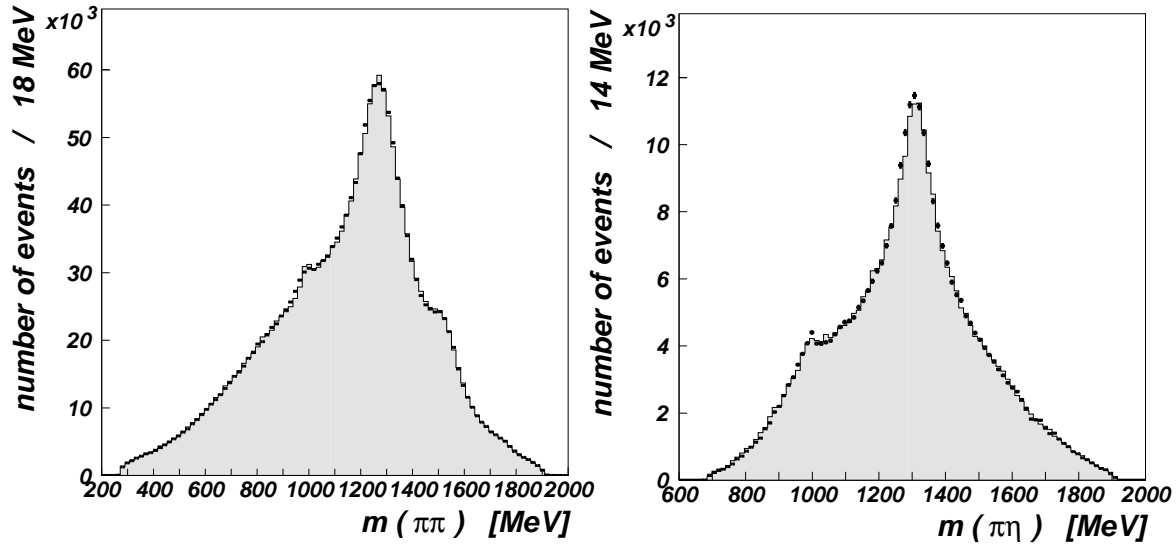


Figure 5.3: *Left:* $\pi^0\pi^0$ mass projection in the $3\pi^0$ channel. The shaded histogram shows the best fit. The peaks are due to $f_0(980)$, $f_2(1270)$ and $f_0(1500)/f_2(1565)$, and the long tail to the new $f_2(1870)$. *Right:* $\pi^0\eta$ mass projection in the $2\pi^0\eta$ channel. The peaks are due to $a_0(980)$ and $a_2(1320)$, the tail to $a_2(1660)$.

meson is the (mainly) $\bar{s}s$ member of the scalar nonet. Our present analysis then strengthens the interpretation of the $f_0(1500)$ as a glueball, or as a state with a large gluonic admixture in its wave-function [13].

Table 5.2 shows a tentative classification of scalar mesons. The low mass scalars are interpreted as scattering resonances. Alternatively, the $a_0(980)$ and $f_0(980)$ are often referred to as $K\bar{K}$ molecules or $q^2\bar{q}^2$ states. For a more detailed discussion and for a bibliography see refs [6, 7].

References

- [1] P. Giarritta, PhD Thesis, Universität Zürich (2000)
- [2] M. Heinzemann, PhD Thesis, Universität Zürich (2000)
- [3] C. Amsler, Rev. Mod. Phys. 70 (1998) 1293
- [4] C. Amsler, Proc. of the Hirscheegg 01 Workshop on Hadron Spectroscopy (2001)
- [5] C. Amsler, Proc. Workshop on Hadron Spectroscopy, Frascati Physics Series, Vol. XV (1999) p. 609
- [6] C. Amsler, Nucl. Phys. A 663 (2000) 93c
- [7] C. Amsler in Review of Particle Physics, Eur. Phys. J. C 15 (2000) 682
- [8] C. Amsler et al., Phys. Lett. B 355 (1995) 425
- [9] A. Abele et al., Eur. Phys. J. C 8 (1999) 67
- [10] M. Acciarri et al., Phys. Lett. B 413 (1997) 147
- [11] B. May et al., Phys. Lett. B 225 (1989) 450
- [12] D. Barberis et al., Phys. Lett. B 462 (1999) 462
- [13] C. Amsler and F. E. Close, Phys. Rev. D 53 (1996) 295

6 Production and Spectroscopy of Antihydrogen

C. Amsler, R. Brunner, D. Grögler, D. Lindelöf, H.P. Meyer, H. Pruijs,
C. Regenfus, P. Riedler[‡], J. Rochet[‡], and T. Speer

in collaboration with:

CERN, Universities of Aarhus, Brescia, Genoa, Pavia, Tokyo, Wales,
Universidade Federal do Rio de Janeiro

(ATHENA Collaboration)

[‡] presently at CERN, Geneva, Switzerland

6.1 Introduction

The final goal of the ATHENA experiment is to compare the properties of antihydrogen and hydrogen atoms with laser spectroscopic methods. In particular, we will measure the 1s - 2s energy difference in antihydrogen atoms. This will test CPT invariance for leptons and baryons with unprecedented accuracy, in the range 10^{-15} to 10^{-18} . Details on the project can be found in Refs. [1, 2] and in previous annual reports.

Antihydrogen has to be produced in large quantities for $\bar{\text{H}}$ spectroscopy. The experimental programme has therefore been split into two distinct phases. The aim of the current phase 1 is to demonstrate the formation of antihydrogen in a Penning trap and to optimize the techniques needed to produce a cold antihydrogen gas. There are large uncertainties for the hydrogen formation rate. The plasma sizes and temperatures have to be controlled and varied, and various recombination schemes investigated. Particularly important are the antihydrogen formation rate as a function of plasma densities and electrode potentials, the recombination scheme, the fraction of antihydrogen atoms with kinetic energies below 0.1 meV, and the cross-section for annihilation with rest gas atoms. The actual CPT test, e.g. with lasers and stored antihydrogen atoms in an inhomogeneous magnetic field, is planned in phase 2 (after 2002). The eventual experimental approach to test CPT will depend on the results achieved during phase 1.

The apparatus consists of a superconducting solenoid (3 T) with a cold bore to house the antiproton trap, the positron storage trap, and the $\bar{\text{H}}$ recombination trap. Antiprotons of 100 MeV/c from CERN's antiproton decelerator (AD) are injected along the axis of the magnet and are moderated through a silicon beam defining counter, an absorption foil and various windows. They are injected in a Penning trap (made of cylindrical electrodes) and reflected by an electrostatic potential. The \bar{p} shot lasts for 200 ns (repetition rate of one every 2 minutes) after which the voltage of the entrance electrode is also raised to capture the antiprotons. They are then cooled to meV energies by interaction with a pre-loaded electron gas inside the capture trap.

Positrons from a strong ^{22}Na source are moderated in solid neon and transferred into a longitudinal magnetic field where they are moderated by nitrogen gas and electrostatic fields. They are then injected into a Penning trap similar to the one used to store the antiprotons, at the opposite end of the superconducting solenoid. The particles stacked in the two traps are finally transported to the central recombination trap which runs at a vacuum of 10^{-12} mbar.

In phase 1 the formation of antihydrogen will be demonstrated by detecting the *simultaneous* annihilation of the positrons (into two 511 keV γ 's) and the antiprotons (e.g. into pions) which occurs when the unconfined (neutral) $\bar{\text{H}}$ atoms hit the wall of the recombination trap. The detector to achieve this task has been proposed, developed and built by the University

of Zurich. It was assembled during 2000 and commissioned in autumn with the first beams from the AD. We now present the detector, discuss our recent R&D results with CsI crystals operating at low temperatures, and report on our experience with the first antiproton beams.

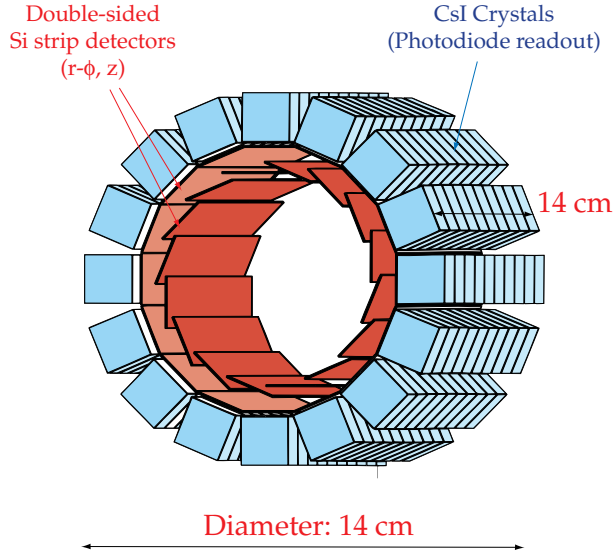


Figure 6.1: 3D sketch of the antihydrogen detector.

6.2 Antihydrogen detector

The pions are detected in two layers of 16 silicon microstrip detectors, and the two back-to-back 511 keV photons in 16 layers of 12 pure CsI crystals (Fig. 6.1). The detector covers a solid angle of $0.85 \times 4\pi$ for charged annihilation particles and $0.66 \times 4\pi$ for γ detection. The unambiguous proof of antihydrogen formation will be obtained by searching for events for which the two hit crystals and the reconstructed annihilation vertex lie on a straight line. The detection of both photons and the collinearity test are important to reduce background: the main background is due to positrons from showers initiated e.g. in the coils of the magnet by the high energy γ 's of annihilation π^0 's. The annihilation vertex can be determined from the charged tracks with an r.m.s. precision of 1.5 mm in radius and 3 mm along the axis. This is sufficient to establish that the events stem from annihilation of the neutral atoms hitting the wall of the recombination trap.

For best detection efficiency the detector is installed as close as possible to the recombination trap, inside the superconducting solenoid. The detector is located in a thermally insulated enclosure at the lowest temperature ($\simeq 77$ K), at which the detector and read-out electronics can be operated. A number of technical problems (thermal expansions of the various detector components, temperature sensitivity of electronic components, light yield of CsI, etc) had therefore to be solved.

The support structure (see Fig. 6.2 right and last year's annual report) holding the outer silicon microstrip modules and the CsI crystals was machined from one block of aluminum in the mechanics workshop of our institute. The cylindrical wall was electro-eroded to $500 \mu\text{m}$ to minimize multiple scattering and γ conversions.

The two cylindrical layers of the double-sided silicon microstrip modules detect the charged pions stemming from an antiproton annihilation on the wall of the recombination trap, or with a rest gas atom (Fig. 6.2). The microstrip detectors were produced by SINTEF. They are 162 mm long, 19 mm wide and $380 \mu\text{m}$ thick and consist of two 81 mm long pieces (n-material) glued and bonded, building a module. The front side is divided into 384 p^+

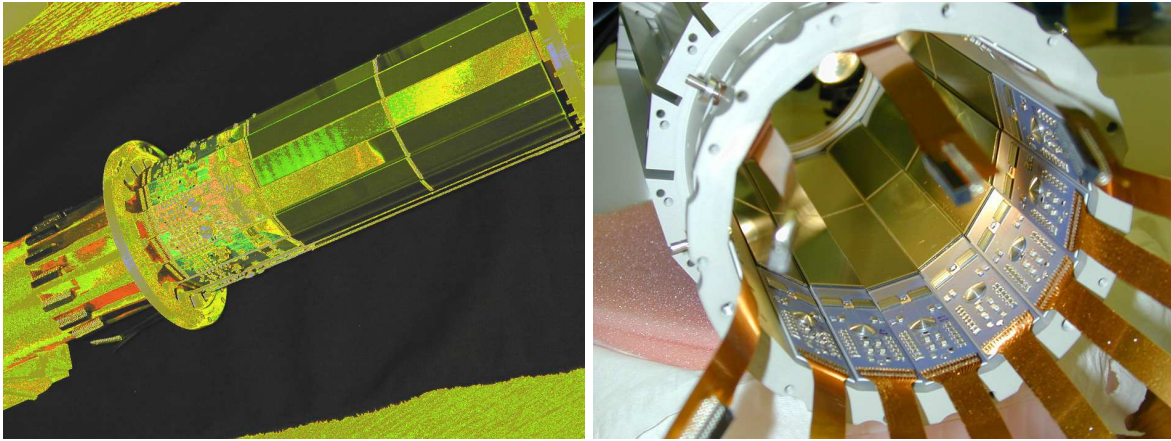


Figure 6.2: *Left: inner layer of 16 silicon microstrip modules, also showing the ceramic hybrids containing the preamplifiers and the capton readout cables. Right: outer layer of 16 silicon microstrip modules.*

strips with a pitch of $47\ \mu\text{m}$ (measurement of the azimuthal angle ϕ), but every third strip only is connected to the readout electronics (hence 128 readout strips per module). The charge collected by the floating strips induces a signal on the readout strips by capacitive coupling. A multiple guard ring structure around the strips ensures low leakage current and a good stability against breakdown. The back side contains 64 pads with a pitch of 1.25 mm. The pads are oriented perpendicular to the strips (measurement of the z coordinate along the detector axis).

The modules are connected to VIKING type (VA2_TA) readout chips, modified for self-triggering and mounted with passive SMD electronics on a ceramic hybrid (see Fig. 6.2). The self-triggering VA2_TA chip is multiplexing its 128 channels into one analogue output line. The multilayered hybrids were designed by our group and built at CERN.

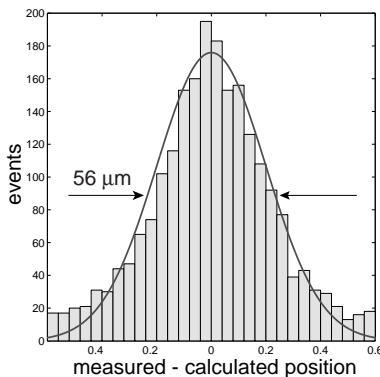


Figure 6.3: *Position resolution of the ATHENA test detector in strip units ($140\ \mu\text{m}$).*

The signals are processed by analogue repeater cards (built by the electronics workshop of our institute) behind the vacuum flange and are then digitized by flash ADC's. The performance of the detector and the readout chips at 77 K was investigated with cosmic rays [3]. The position resolution was determined with our track defining silicon microstrip telescope [4]. Figure 6.3 shows the distribution of the difference between the coordinates predicted from the telescope and the coordinates measured with the ATHENA strips. The latter was derived from the mean strip number between the two signal strips, weighted by the energy deposits. The predicted coordinate was obtained from a linear fit to the hits in the beam telescope. We obtained an r.m.s. resolution of $24\ \mu\text{m}$ (Fig. 6.3). The signal to

noise ratio was about 50.

The time resolution of the microstrip detector was also determined with cosmic rays and a resolution of 16 ns (FWHM) was measured.

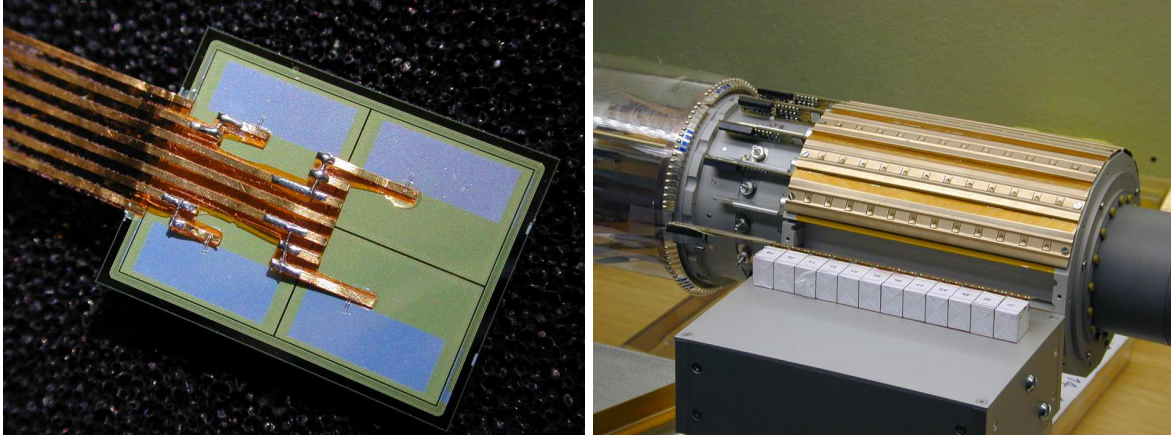


Figure 6.4: *Left: segmented photodiode with the bonded readout lines. The four (p^+) implants cover each a surface of 40 mm^2 . Right: one of the 16 crystal rows before insertion into the support structure.*

The pure CsI crystals (manufactured by CHRISMATEC) are read out by photodiodes, also provided by SINTEF. As pure CsI emits light in the UV region, the diodes were especially designed with very thin entrance windows. Each photodiode was subdivided into four segments to reduce the capacitive noise (Fig. 6.4 left). The four pads were made of p^+ implants on n-material. The layer in contact with the crystal is a thin n^+ covered by a SiO_2 layer of thickness $\sim 0.75 \lambda$ (where $\lambda = 350 \text{ nm}$ and 0.75 is the inverse of the refractive index), in an attempt to maximize the light reaching the depletion region. The positive voltage applied to the n^+ side is transferred to the guard ring on the pad side through an aluminum deposit along one edge of the diode.

The crystal dimensions are $13 \times 17.6 \times 17.1 \text{ mm}^3$. Figure 6.4 right shows one of the 12 rows of crystals wrapped in teflon tape before insertion into the support structure.

The 48 readout lines of a crystal row (12×4 pads) are connected to one VA2_TA chip. Custom designed capton cables connect the 48 hybrids (2×16 for the 2 silicon layers and 16 for the crystals) with the patch panel (Fig. 6.5).

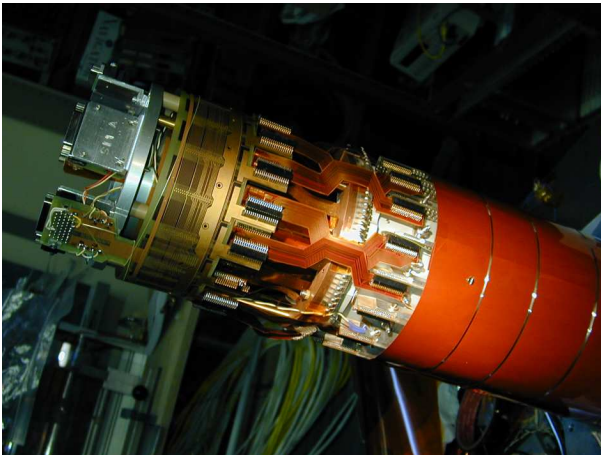


Figure 6.5: *Patch panel showing the readout side of the detector.*

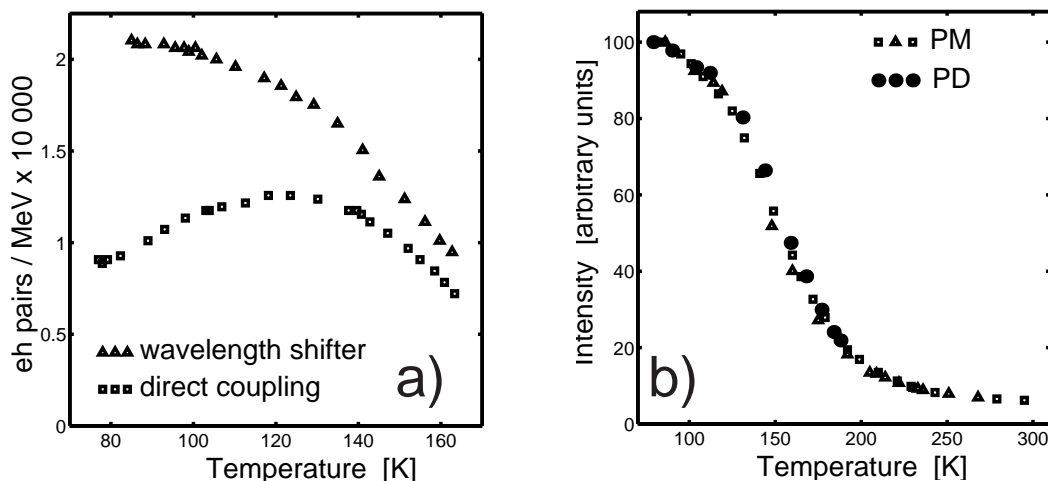


Figure 6.6: a): Yield of electron-hole pairs measured with a pure CsI crystal and a photodiode, with and without wavelength shifter. b): Light yield of pure CsI crystals as a function of temperature. Both measurements, one with a photomultiplier (PM), and the other with a photodiode (PD) and wavelength shifter, are normalized independently to the maximum.

6.3 Performance of undoped CsI at low temperature

In 1998 we initiated a programme to investigate the properties of pure CsI coupled to photodiodes as a function of temperature. We also built a test bench at 77 K to measure the light output with photomultipliers [5]. Tests with crystals from various suppliers using different polishing and wrapping methods were performed in parallel by our collaborators at Pavia.

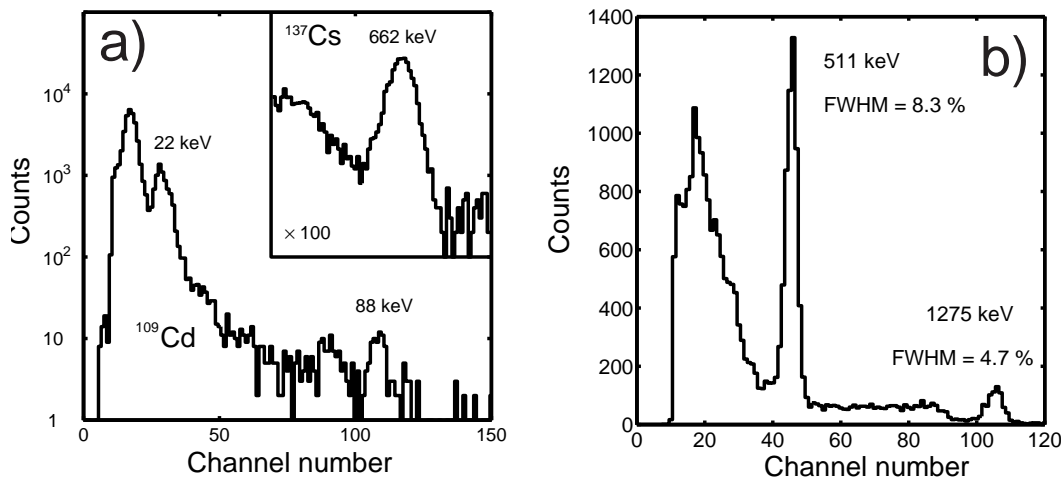


Figure 6.7: a): Calibration of the photodiode at 77 K with X-rays from a ^{109}Cd source and γ -rays from a ^{137}Cs source (inset). b): ^{22}Na spectrum taken with a sprayed pure CsI crystal coupled to a photodiode and preamplifier at 77 K.

Final results are being published [6]. The scintillation yield of pure CsI is known to increase with decreasing temperature. Hence the pulse height (proportional to the number of electron-hole pairs in the photodiode) was expected to behave accordingly. The increase in pulse height was indeed observed with photomultipliers, but with photodiodes we observed a maximum around 120 K, below which the signal decreased rapidly. This effect was traced

to the quantum efficiency of the photodiode which we measured as a function of wavelength, using a tunable light pulse generator (Xe lamp and diffractive grid) [7]. In the wavelength region of maximum light emission (340 nm at 77 K), the quantum efficiency of the photodiode oscillates between 10 and 20 % (presumably due to interference effects in the window), but rises rapidly above 360 nm to reach $\sim 75\%$ at 600 nm. We therefore sprayed the faces of the crystal with a fluorescent red dye to shift the wavelength into the red range. The yields with and without paint are shown in Fig. 6.6a. The measurements with photomultiplier and photodiodes agree for red light (Fig. 6.6b) and the light output increases by a factor of 15.8 ± 1.0 between room temperature and 77 K.

The number of electron-hole pairs in the photodiode per unit energy deposit in the crystals was measured with the 662 keV photons from a ^{137}Cs source. The calibration was achieved with 22 and 88 keV X-rays from a ^{109}Cd source, directly absorbed in the photodiodes. Figure 6.7a shows the X-rays spectra. At 77 K we obtained $39'600 \pm 1'200$ electron-hole pairs per MeV, a result only 20 % below the yield of doped CsI(Tl) at room temperature. Figure 6.7b shows the γ spectrum from a ^{22}Na source. The resolution for 511 keV γ 's is 8.3 % (FWHM). The decay time increases from 28 ns (main component) at 300 K to $\simeq 1 \mu\text{s}$ at 77 K [6]. The longer decay time is still acceptable for detecting antihydrogen in ATHENA.

6.4 First results with antiprotons

The antiprotons were decelerated in the AD from 3.5 GeV/c down to 100 MeV/c for the first time in July 2000 and the AD provided its first useful beam of 1.5×10^7 antiprotons per pulse at 100 MeV/c.

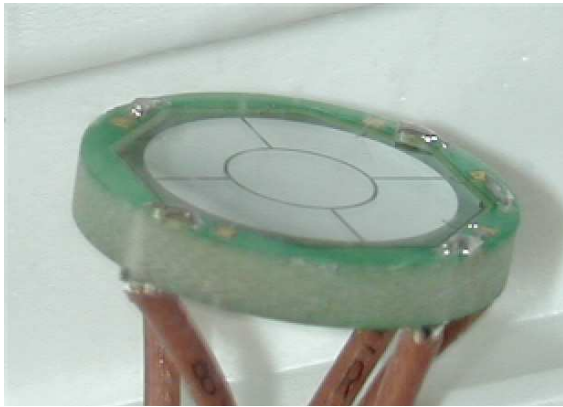


Figure 6.8: Segmented silicon beam counter.

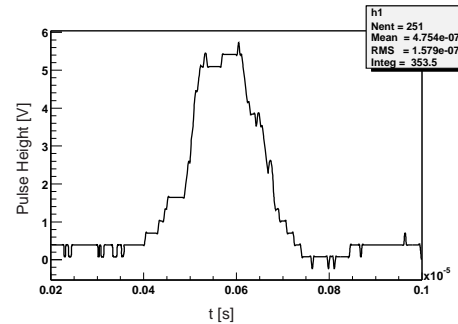


Figure 6.9: Pulse height delivered by the silicon beam counter; the spill length is about 200 ns and corresponds to a few 10^6 antiprotons.

The first thousand trapped antiprotons were also observed in ATHENA in July 2000. The extracted beam had a diameter of 3 mm and a momentum bite $\Delta p/p$ of 10^{-4} . The current from the incident antiprotons was measured in front of the \bar{p} capture trap. Figure 6.8 shows the segmented silicon counter that was recycled from our former Crystal Barrel experiment. The segmentation allowed a fine steering of the incident beam. Figure 6.9 shows the current as a function of time. An intensity of typically 3×10^6 antiprotons per pulse could be derived from the measured current. The noise induced on the beam counter by the nearby quickly rising trapping voltage was found to be negligible (typically 100 mV compared to a \bar{p} signal of several volts, see Fig. 6.9).

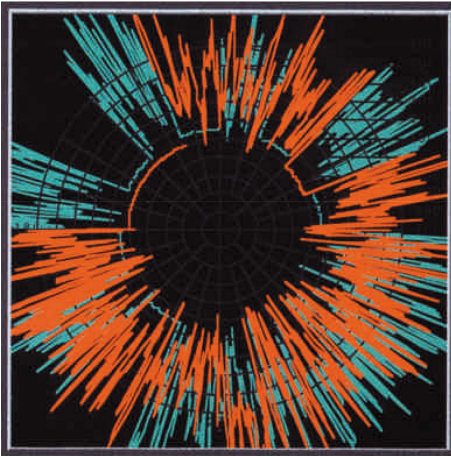


Figure 6.10: *Signals from annihilation pions in the detector inner layer (red) and outer layer (blue). The lengths of the spikes are proportional to the energy losses.*

The antiprotons were degraded by an aluminium foil and then electrostatically decelerated in the trap. Figure 6.10 shows pion tracks in the microstrip detector from a spill of antiprotons annihilating in the entrance windows. A thin rotating foil allowed for fine tuning of the absorber material needed to capture the antiprotons. The optimum degrader thickness was found by counting the stored antiprotons through their delayed annihilation: The voltage on the entrance electrode, which had been raised at the end of the spill, was lowered slowly. This allowed the antiprotons to escape the trap and to annihilate in the apparatus. The rate was measured by scintillator paddles installed below the magnet. Figure 6.11 shows the \bar{p} annihilation rate as a function of time for various absorber thicknesses, and also the final range curve. The estimated total number of trapped antiprotons was around 7,000 per spill in these first attempts.

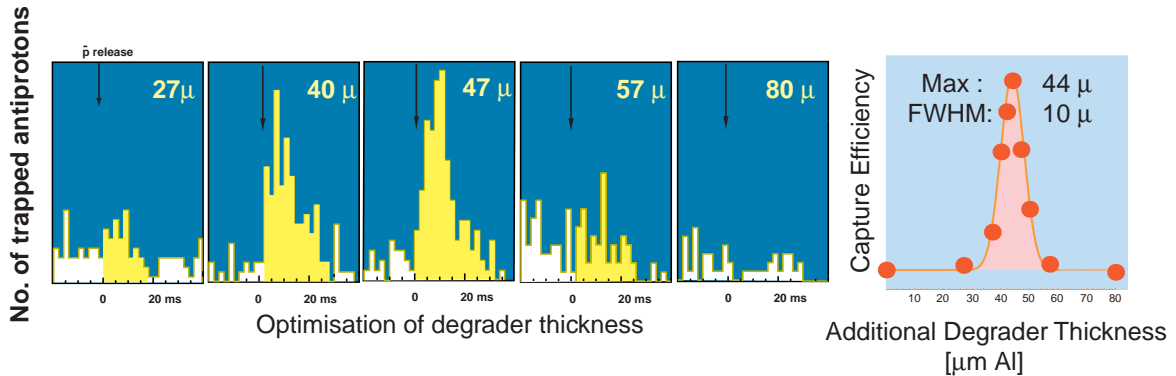


Figure 6.11: *Annihilation from antiprotons escaping the trap as a function of time (during the slow reduction of the confining voltage) for different beam degrader thicknesses. The number of trapped antiprotons reaches a maximum around 44 μm of aluminium (right curve).*

Once captured, the antiprotons could be cooled to meV energies by an electron gas. This cold gas (typically 3×10^8 electrons) was preloaded in the trap with an additional electrostatic potential supplied by the central ring electrodes (Fig. 6.12). Electron cooling occurs rapidly by synchrotron radiation. The cooled antiprotons can be detected by first reducing the main trapping voltage T_1 (which eliminates the hot antiprotons) and then the additional well T_2 (which eliminates the cold antiprotons). Figure 6.12 is quite encouraging as it demonstrates that indeed the number of cool antiprotons increases with cooling time.

Summarizing, the ATHENA experiment and the AD perform as expected. Initial trials

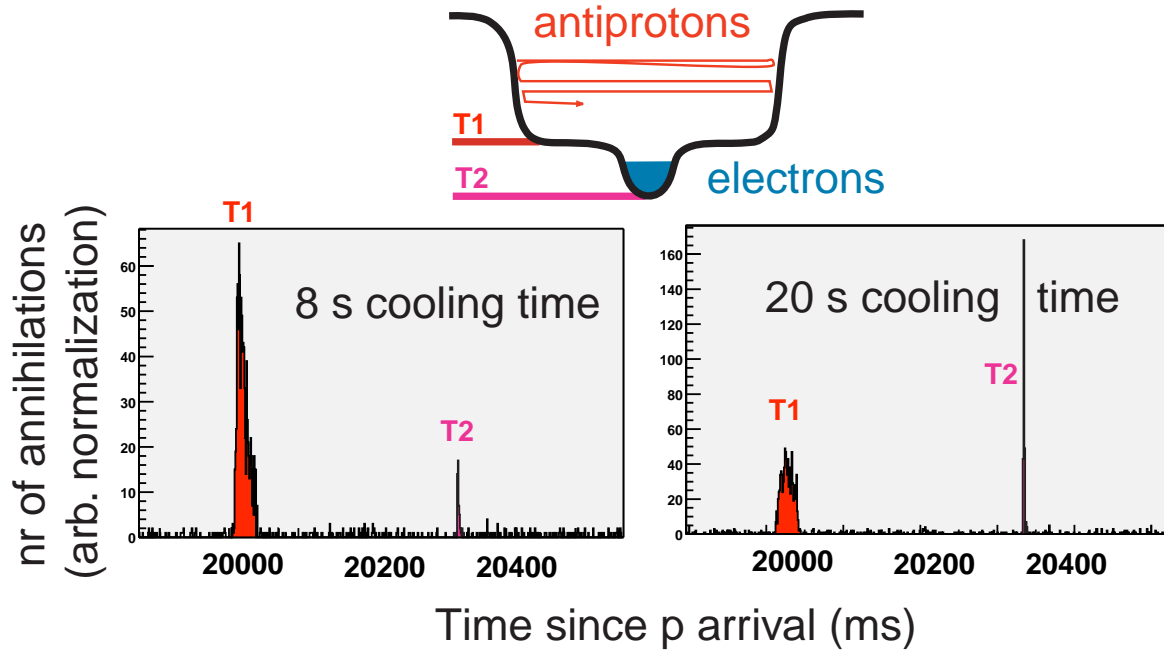


Figure 6.12: *Annihilation rate, showing that the fraction of electron cooled antiprotons T_2 increases with time (see text).*

to capture protons and positrons are quite promising. Our goal for the next two years is to demonstrate the formation of antihydrogen and to optimize the $e^+ \bar{p}$ recombination rate.

References

- [1] ATHENA proposal, CERN SPSLC 96-47, see <http://www.cern.ch/athena/>
- [2] C. Amsler et al. (ATHENA Collaboration), Proc. Hydrogen II Conf., Castiglione de Pescaia, Springer (2000)
- [3] R. Brunner, *Aufbau und Test eines Microstrip-Detektors für das ATHENA-Experiment*, Diplomarbeit, Universität Zürich, 2000
- [4] C. Amsler et al., Submitted to Nucl. Instr. and Methods in Phys. Res.
- [5] P. Niederberger, *Untersuchung von CsI-Szintillatoren bei tiefen Temperaturen*, Diplomarbeit, Universität Zürich, 1999
- [6] C. Amsler et al., Submitted to Nucl. Instr. and Methods in Phys. Res.
- [7] We thank the IPHE group for the kind assistance during these measurements at Lausanne University

7 Particle Physics at DESY/HERA (H1)

J. Becker, Ilaria Foresti, S. Hengstmann, M. Hildebrandt, N. Keller, J. Kroseberg, Katharina Müller, P. Robmann, F. Sefkow, U. Straumann, P. Truöl, M. Urban, R. Wallny and Nicole Werner

in collaboration with:

R. Eichler, W. Erdmann, C. Grab, M. Hilgers, H.-C. Kästli (until May 2000), B. List, S. Lüders, D. Meer and A. Schöning, Institut für Teilchenphysik der ETH, Zürich, S. Egli, K. Gabathuler, J. Gassner, and R. Horisberger, Paul-Scherrer-Institut, Villigen, and 34 institutes outside Switzerland

(H1-Collaboration)

7.1 Electron-proton collisions at up to 320 GeV center of mass energy: overall status of the project

In its last year before the major upgrade the HERA electron/positron-proton storage ring operated with positrons. A total luminosity of 56 pb^{-1} was accumulated. The big shutdown originally planned for May 2000 was delayed until September to let the HERA-B experiment take first physics data, and also to adapt for delivery delays of various components needed for the upgrade of HERA, the H1- and the ZEUS-experiment. The luminosity in the year 2000 constitutes 40 % of what is available for e^+p collisions altogether (see Table 7.1).

Table 7.1: Summary of HERA and H1 operation during the previous nine years.

Parameter	e^-p		e^+p		Sum
	1992-94, 1998/99		1994-99	2000	
Integrated luminosity \mathcal{L}					
HERA produced	$[\text{pb}^{-1}]$	28.3	95.8	69.5	165.3
HERA physics	$[\text{pb}^{-1}]$	26.6	90.0	66.8	156.8
H1 taken	$[\text{pb}^{-1}]$	22.7	71.6	59.4	131.0
H1 physics	$[\text{pb}^{-1}]$	19.9	65.1	56.2	121.3
HERA efficiency	$[\%]$	94	94	96	95
H1 efficiency	$[\%]$	75	72	84	77
Average luminosity	$[(\mu\text{b s})^{-1}]$	3.15	3.64	6.47	4.83
Peak luminosity	$[(\mu\text{b s})^{-1}]$	12.1	12.6	17.9	17.9
Average p current	$[\text{mA}]$	67.5	70.6	86.7	77.4
Average e^\pm current	$[\text{mA}]$	17.2	22.9	25.1	23.8
HERA luminosity runs		700	1376	346	1722
Permanent H1 runs	$[10^3]$	9.6	18.7	6.0	24.7
Average duration	$[\text{min}]$	20	22	28	25

Most of our publications use pre-1998 data only. A major effort, part of which is described below, was undertaken to improve the calibration and alignment of tracker components. After this was accomplished the reprocessing of the 1999/2000 data has recently been started. In 15 publications [1]-[15] of the collaboration the following principal areas are covered:

- neutral and charged electroweak current cross sections, proton structure functions and parton densities at high momentum transfer Q^2 [2, 13, 14],

- search for states outside the standard model [4, 9, 15],
- photon structure [5],
- parton-fragmentation into multijet final states [1, 10, 11, 12],
- electroproduction of exclusive final states [7, 8], and
- production of heavy quark-antiquark states, of open charm and beauty [6].

We will report below on the analyses in the heavy quark sector (Sect. 7.4.1), an area where there is manifest activity of the University of Zürich group, and also give an update of the high Q^2 data. The latter results are based also on data taken in 2000, have not been published, but were included in the 36 contributions of our collaboration to the ICHEP-2000 conference [16].

With the submission of a publication [13] and the thesis the analysis project of Rainer Wallny has been concluded. This work deals with deep-inelastic inclusive ep scattering at low x and a measurement of α_s , and was discussed in detail in our previous annual report. Another Zürich analysis project (thesis of Nikolas Keller) concerns QED Compton scattering. Events with both the scattered electron and the radiated photon within the main detector are investigated and will ultimately allow a comparison of the photon and gluon distributions within the proton.

Besides the physics analysis, our activities dealt with the maintenance, monitoring and calibration of the detector components built in Zürich for the central tracker and the first level trigger of H1. Most of our effort, however, was directed towards the H1 detector upgrade which progressed with minor delays. At present the H1-detector is ready for the installation of the first superconducting focussing magnet into the forward tracker. The central tracker, with the exception of the silicon detectors, is installed too. One element, the superconducting coil used to compensate the influence of the H1-analysing magnetic field on the proton beam, has now become obsolete. This element, indispensable for high luminosity tuning, was manufactured by Swiss industry and largely financed by University of Zürich funds. It functioned without problems for ten years. Figure 7.1 show the magnet on its way to storage.

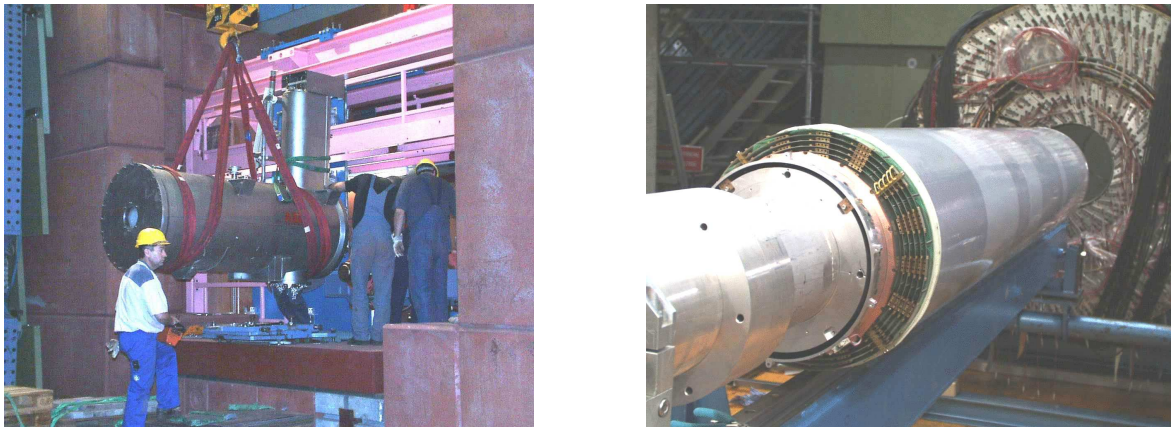


Figure 7.1: *Left: The superconducting compensator coil is being taken out of the beam line (October 2000). Right: Installation of the new central inner proportional chamber (CIP) into the central tracking device of the H1 Detector in Hamburg. The central jet chambers (CJC) which surround the CIP can be seen, too (February 2001).*

7.2 Summary of activities related to the H1-upgrade

As part of the H1 upgrade the two inner proportional chambers (CIP) and the inner drift chamber (CIZ) are replaced by a new five-layer proportional chamber (CIP2000). The aim is to improve z -vertex triggering and track reconstruction at the trigger level, as well as background rejection. The number of readout channels both in z and in azimuthal direction have increased. Five layers rather than two will provide redundancy and help resolve ambiguities in the track reconstruction of the central silicon tracker. The new CIP has pad readout in 16 azimuthal sectors. The trigger scheme is based on a projective pad geometry in the z direction, thus resulting in a varying number of pads per layer (ranging from 119 to 93 for the innermost and outermost layer, respectively). The larger number of detector channels also required new readout and trigger electronics.

The project was coordinated by the University of Zürich with ETH Zürich and University of Heidelberg as partners. The University of Zürich was responsible for the design and construction of the multiwire proportional chambers. The construction started in autumn 1999 and was completed by the end of 2000.

The ASIC laboratory in Heidelberg developed the amplifier and readout chip CIPix, and the electronics for trigger and data acquisition is a common Heidelberg and Zürich University effort. ETH Zürich is responsible for all components dealing with the optical data transmission from the detector to the electronic trailer.

Meanwhile the new chamber has been installed in the H1 detector. Further details are given below.

7.2.1 Central inner proportional chamber construction

Between July 1999 and February 2001 three to five people worked permanently on the construction and test of the new chamber which consists of an innermost layer with anodes only, four layers with cathode pads inside and anode wires outside and an outermost layer with only readout pads, all planes including readout cabling. 2400 anode wires were strung at the Paul-Scherrer-Institut Villigen (PSI) on provisional frames and soldered to the detector in Zürich. To guarantee a stable wire position the tension has to be around 80 g. Every individual wire has been tested, 30 of which had to be exchanged.

After the assembly of the whole chamber in December 2000 the first high voltage test took place. Due to two broken wires the chamber had to be reopened for a short time. From December to January the high voltage was increased up to the operation point of 2395 V and first signals were seen. Until February last wire problems had been solved, thus all layers operate at 2500 V. Fitting the cooling units to the readout electronic boards turned out to be a difficult task, but a solution was found. The chamber survived the transport from Zürich to Hamburg without any harm. Due to a glue seam at the $+z$ end of the Central Jet Chamber the CIP is now installed 1 mm shifted in backward direction. The readout prints are planned to be mounted at the beginning of April 2001.

7.2.2 CIP Electronics

Last year several tests of the readout electronics from PSI have been performed with the CIP prototype including the CIPix card and receiver card prototypes. Amongst others the pulse shape, efficiency and time resolution have been studied [17].

In order to measure the time resolution a ^{106}Ru β source was placed upon the CIP prototype and two scintillators on top and on bottom of the chamber acted as a coincidence

indicator for particles passing through. The HERA bunch structure was simulated by selecting tracks within 24 ns of the rising edge of a 10 MHz clock. The delay Δt of the signal readout was shifted between 0 and 70 ns and the number of signals coming from the correct bunch crossing divided by all coincidence signals was measured. This fraction is required to become one within significantly less than one bunch crossing. The resolution is measured to be better than 50 ns as can be seen in Fig. 7.2.

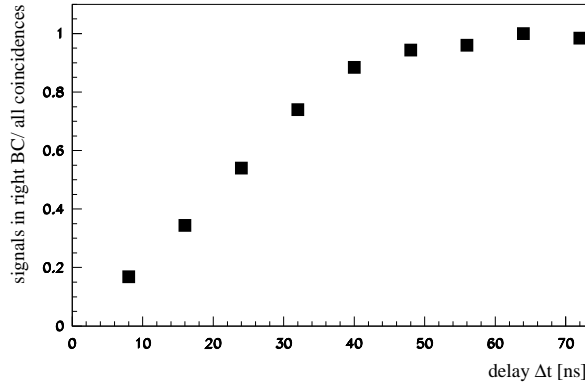


Figure 7.2: *Efficiency of the CIP prototype v.s. gate delay measured with a ruthenium source.*

In February 2001 part of the readout electronics was connected to the chamber and tested for the first time. Eight CIPix chips on the fifth chamber layer were connected to receiver cards through two optical links. The programming of the CIPix chips via an I²C-Bus has been developed in the framework of a diploma thesis [17]. After the usual grounding problems had been solved, pulse shapes as shown in Fig. 7.3 were recorded. The pulses were measured by using a scintillator coincidence as a trigger for tracks induced by the source. In addition to the analog pulse the digital signal is displayed in Fig. 7.3.

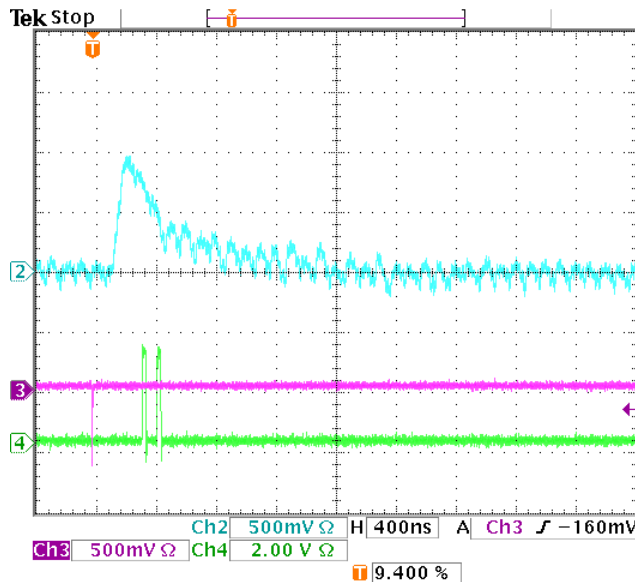


Figure 7.3: *Signals from a ruthenium source from layer 5 of CIP2000, after being transmitted through the optical link. The analog pulse (blue) triggered by a scintillator coincidence (pink) is transformed into a digital signal (green) on the CIPix chip.*

15 Feb 2001
12:03:16

The same setup was used to measure the first efficiency curve of the CIP2000. The plateau starts at around 2300 V which is comparable to the value of the old CIP. For the inner layers, which have narrower interwire spacing, the required voltage will be slightly higher.

The assembly of all CIPix and receiver cards with optical hybrids for all layers is now going on at PSI and expected to be finished at the end of March 2001. The mounting of the frontend electronics to the chamber is planned for April.

The trigger electronics has been developed and built together with the electronics workshop of the University of Heidelberg [18]. All trigger cards have been successfully tested and are ready since February 2001. In order to build trigger elements for the H1 trigger system, signals from the CIP2000 are readout in form of trigger histograms. These histograms are calculated by sum cards which are under construction and are expected to be ready in April.

For details about the data acquisition and control system of the CIP2000 see [19].

7.3 A new era of tracking at H1

The capability to detect heavy quarks through their lifetime broadens the scope of the HERA physics programme considerably. New possibilities arise not only for testing QCD and probing aspects of hadronic structure, but also for searches for processes beyond the Standard Model in which long-lived particles are produced. To resolve the secondary vertices of e.g. b hadrons with a mean life corresponding to $c\tau = 470 \mu\text{m}$ requires an excellent tracking performance; the efficiency to tag b hadrons and suppress background is directly related to the precision with which tracks from the secondary decay vertices can be reconstructed.

To fully exploit the potential of the H1 silicon micro-vertex detector (CST), it is therefore necessary to optimize the performance of the entire tracking system. To achieve this goal, the H1-collaboration has launched a dedicated tracking task force in autumn 1999 convened by F. Sefkow. The main project is a complete and consistent recalibration and alignment of the entire tracking system. The studies are based upon 10^7 cosmic muon triggers, which were recorded especially for this purpose. The alignment benefits from the enhanced redundancy and precision induced by the CST information into the tracking system, shown in Fig. 7.4.

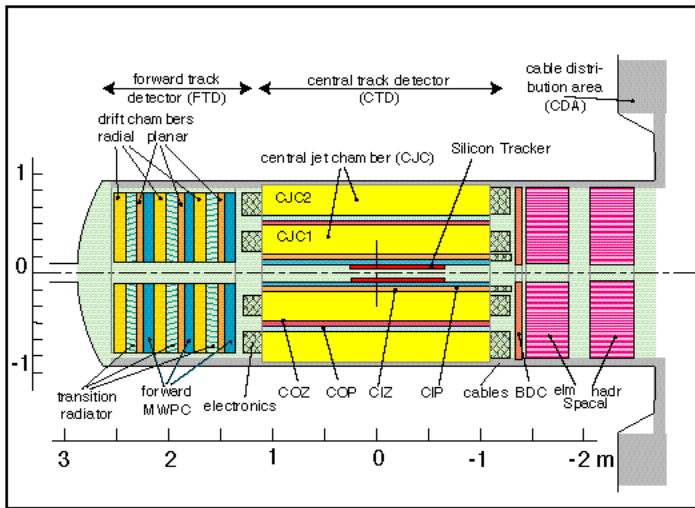


Figure 7.4: Schematic side view of the tracking system.

A frequent problem in tracking alignment is that reference tracks from one initially miscalibrated detector or detector part induce biases into the calibration of another, which requires lengthy iteration procedures. Such biases are avoided in the approach implemented in the MILLEPEDE program [20]. In this ansatz alignment and calibration parameters are called *global*, while individual track parameters are called *local*. Using the track information from many thousands of events the new fit algorithm allows for a simultaneous fit of all global and local parameters as an exact solution of a least squares minimisation problem. With $n = 10^3$ global parameters, typically, and $N = 10^4 \dots 10^6$ track parameters, this corresponds to the inversion of a huge $(N + n) \times (N + n)$ matrix, a problem which can be reduced to solvable size in MILLEPEDE because only the global parameters need to be explicitly known.

Focusing on the central z -chamber (CIZ), built at our institute, we briefly outline the new fit technique and present the improvements (Thesis S. Hengstmann). The CIZ is a drift chamber subdivided into 15 rings in z with in total 60 sense wires strung concentrically and perpendicular around the beam axis, to measure the z coordinate of tracks. The local track-model of the z -chamber is given by the equation $z = z_0 + \lambda \cdot S$, where S denotes the transverse arc-length of the track and z_0 and λ are the straight line fit parameters with $\lambda = \cot(\theta)$. The geometrical alignment and calibration constants are global translations (Δx , Δy) and rotations (γ , ψ , ω) around the z , x and y -axis, wirewise z -shifts $\Delta z^1, \Delta z^2, \dots, \Delta z^{60}$, drift velocities v_d and drift time corrections $t_0^1, t_0^2, \dots, t_0^{60}$. They can be integrated into one global fit-vector

$$\vec{P} = (\Delta x, \Delta y, \gamma, \psi, \omega, v_d, t_0^1, t_0^2, \dots, t_0^{60}, \Delta z^1, \Delta z^2, \dots, \Delta z^{60}) \quad (7.1)$$

and the local track model can be expanded to the form

$$z_{Hit} = z_0 + \lambda \cdot S_{Hit} + \vec{A} \cdot \vec{P}, \quad (7.2)$$

where the vector \vec{A} contains the derivatives $\partial z / \partial \vec{P}$, which have to be supplied in analytic form to MILLEPEDE. Similar formulae are valid for the outer z -chamber (COZ) which has 96 wires. The new z -coordinate fit determines the more than 300 CIZ and COZ alignment and calibration constants in a single step. It uses a large sample of cosmics precisely measured by the CST, together with tracks outside the CST acceptance. The simultaneous fit ensures that the precise constraints of the CST are propagated to the entire z -chamber system.

Results of the re-calibration are presented in Fig. 7.5. Here only central rings are shown, which almost fully overlap with the CST. In a first step correction the hit resolution has already been improved from 800 μm to 500 μm . With the final step, displayed here, remaining shifts in the residual distribution of δz indicating a misalignment vanish and the resolution improves further almost uniformly to $\sigma_z = (378 \pm 5) \mu\text{m}$. This result is consistent with the intrinsic resolution, as determined from hit triplets.

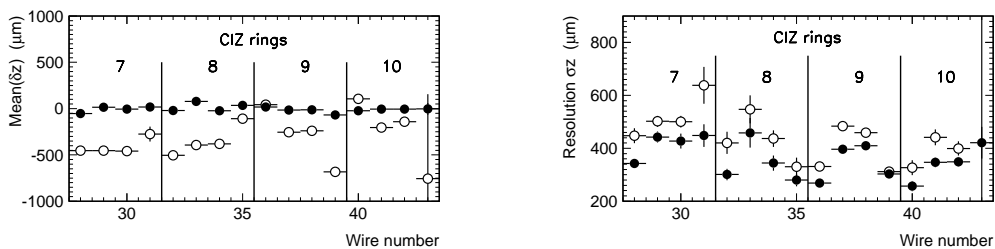


Figure 7.5: (a) Residuals δz and (b) resolution σ_z versus wire number before (open dots) and after (full dots) the new z calibration.

A complete re-calibration of the central jet chamber (CJC) has also been performed in the framework of the new fit using the precise CST information as a constraint. With the two cylindrical, coaxial drift volumes (CJC1 and CJC2) (see Fig. 7.4) consisting of in total 90 cells and 56 wire planes parallel to the beam axis, about 1000 parameters have to be fitted to calibrate the track measurement in the $r\phi$ -plane. Special corrections accounting for inhomogeneities of the drift region and the magnetic field, pulse shape dependence, time-of-flight, etc., have also been applied. An improvement of the resolution by about 40 % for the track parameters distance of closest approach d_{ca} , ϕ and $1/p_t$ is observed consistent with a

gain in the single hit resolution from $240\ \mu\text{m}$ to $140\ \mu\text{m}$ in the $r\phi$ -plane, which is the design value.

The new algorithm has also been applied to calibrate the CJC z -position and energy-loss (dE/dx) measurement, determined from the charge amplitudes on opposite ends of the wires. The amplitudes are highly correlated and show moderate resolutions. Furthermore they depend on the gas pressure, the electron current in HERA, on the track angle θ and there are effective corrections to the Bethe-Bloch formula. Considering all effects almost 8000 calibration constants have to be fitted. For this procedure a consistent calibration of the z -chambers (CIZ and COZ) was found to be essential.

The complete alignment and calibration of the CST requires the determination of 384 parameters. The combined CST+CJC track fit yields an impact parameter resolution of about $30\ \mu\text{m}$ which is again according to design and similar to values achieved in LEP detectors.

The total integrated luminosity that benefits from the recalibration amounts to about $100\ \text{pb}^{-1}$. The data have been taken during the years 1997 to 2000 and are currently reprocessed at H1. To account for time-dependent beam line parameters and calibration constants, e.g. drift velocities, two reconstruction passes are needed. An online version of the new fit algorithm has been implemented into the reconstruction software to determine these parameters in the first pass. Afterwards the results are fed into a second pass of the final re-processing. For this dual procedure a time-frame of 4 - 5 month is estimated. It is currently on track to finish before the end of the present shutdown.

7.4 Results from recent analyses

7.4.1 Beauty production

The important contributions of our group to track-based triggering and to precision tracking continue to be complemented by a strong analysis effort in the field of heavy quark production, which critically relies on these detector capabilities.

The heavy quarks, by virtue of their mass, provide an ideal test bed to explore the range of applicability of perturbative QCD. Furthermore, since in the QCD picture of ep interactions, heavy quarks are predominantly produced in the interaction of a real or virtual photon emitted from the scattered electron with a gluon in the proton, they carry direct messages about the gluons entering the hard scattering process.

Most results so far were obtained with charm quarks. We have used the clean experimental signature of D^* mesons [21] to measure the gluon density in the proton, and to probe the rôle of gluons in the dynamics of diffractive interactions [22] (Thesis S. Hengstmann). In comparison, relatively little is known so far about the production of beauty quarks at HERA, which is about 100 times less abundant than charm. Only the magnitude of the photo-production cross section has been measured [23] so far and found larger than expected. In DIS, beauty production has not yet been observed at all.

Whereas the theoretical description of charm production is found to be in reasonable agreement with data, not only at HERA, it appears to be difficult to reproduce the high beauty production rates with QCD calculations, even when next-to-leading order terms are included. The problem is known for some time for $\bar{p}p$ collisions [24], but similar discrepancies are seen in photo-production and have recently also been reported from high energy two-photon collisions at LEP [25]. These observations are in remarkable contrast to the expectation that contributions from higher orders should be smaller in the case of beauty than for charm, due to the larger mass scale, so that the theory should be more reliable, and they have thus given rise to speculations about contributions from non-standard production mechanisms (e.g. [26]).

Measurements at HERA can provide important clues to better understand beauty production, since, compared to $\bar{p}p$, γp and $\gamma\gamma$ interactions uncertainties due to imprecise knowledge of hadronic structure are smallest in ep scattering.

In this field, we could in the last year harvest the first fruits from our efforts to integrate the central silicon tracker [27] (CST) into the analysis. We confirmed the earlier photo-production measurement by using an independent, lifetime-based signature [28], and we succeeded in performing a first measurement of beauty production in DIS [29] (Thesis J. Kroseberg).

All H1 measurements are done using event samples with two jets accompanied by a muon identified as penetrating track in the instrumented iron and well measured in the CST. They rely on the signature of semileptonic decays of b hadrons in jets. The previous H1 measurement was based on the high transverse momentum p_T^{rel} with respect to the jet direction, which the lepton acquires due to the higher b mass. The long lifetimes of b hadrons, which can be measured with micro-vertex detectors, provide an independent signature. For each muon candidate, the impact parameter δ is calculated in the plane transverse to the beam axis. Its magnitude is given by the distance of closest approach of the track to the primary event vertex. Its sign is positive if the intercept of the track with the jet axis is downstream of the primary vertex, and negative otherwise. Decays of long-lived particles are signalled by positive impact parameters, whereas the finite track resolution yields a symmetric distribution.

The b cross section is extracted by decomposing the impact parameter distribution, Fig. 7.6. The fit yields a beauty fraction of $f_b = (26 \pm 5)\%$ which translates into a cross

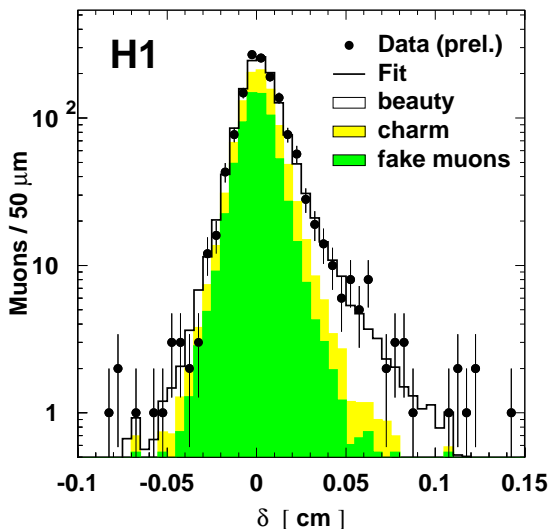


Figure 7.6: *Impact parameter distribution and decomposition from the likelihood fit.*

section consistent with the published result, based on earlier data, within the statistical error.

One can enrich the b component in the events by restricting the range of one variable, e.g. p_T^{rel} and then studying the distribution of the other quantity, δ , and *vice versa*. Fig. 7.7 shows a clean beauty signature in both observables.

The two variables δ and p_T^{rel} complement each other in the discrimination of the beauty component in the data against the different background sources. The separation power can be combined in a likelihood fit of the two-dimensional distribution of these quantities. The result, averaged with the published number, is $\sigma(ep \rightarrow b\bar{b}X \rightarrow \mu X) = (170 \pm 25)$ pb in the range $Q^2 < 1$ GeV², $0.1 < y < 0.8$, $p_T(\mu) > 2$ GeV, $35^\circ < \theta(\mu) < 130^\circ$. This is significantly higher than the NLO QCD prediction.

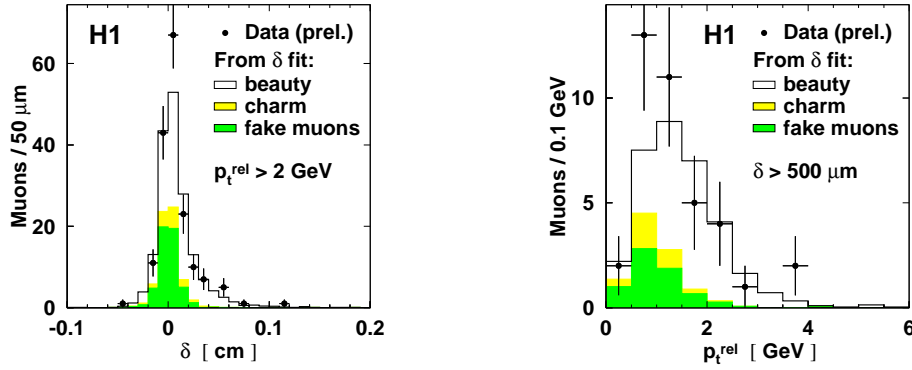


Figure 7.7: Impact parameter distribution for muon candidates with $p_T^{rel} > 2 \text{ GeV}$ (a) and p_T^{rel} distribution for muon candidates with $\delta > 500 \mu\text{m}$ (b), with estimated contributions.

The same method has been applied to obtain the first measurement of b production in DIS, where the statistics is considerably lower. The likelihood fit of the reference spectra to the two-dimensional distribution in δ and p_T^{rel} yields a $b\bar{b}$ fraction of $f_b = (43 \pm 8) \%$. The projections of this distribution are shown in Fig. 7.8 together with the decomposition from the fit. The distributions of both variables are well described, and the need for a $b\bar{b}$ component is evident from the lifetime based signature as well as from the p_T^{rel} spectrum. The cross section in the visible range $2 < Q^2 < 100 \text{ GeV}^2$, $0.05 < y < 0.7$, $p_T(\mu) > 2 \text{ GeV}$

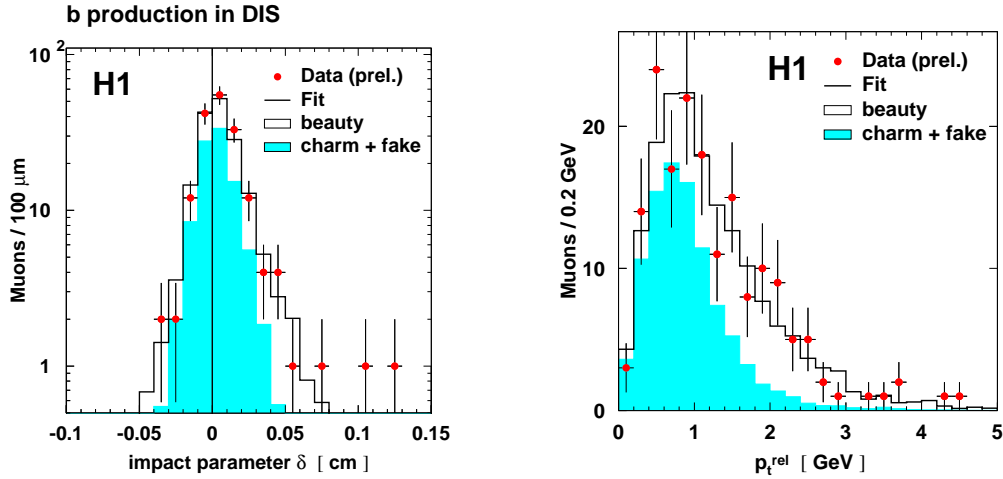


Figure 7.8: Impact parameter distribution (left), and distribution of transverse momentum relative to the jet axis (right), with decomposition from the likelihood fit.

and $35^\circ < \theta(\mu) < 130^\circ$ is found to be

$$\sigma_{vis}(ep \rightarrow b\bar{b}e'X \rightarrow \mu X) = 39 \pm 8 \text{ (stat.)} \pm 10 \text{ (syst.) pb}.$$

This measurement can be directly compared to a NLO QCD calculation, which gives $(11 \pm 2) \text{ pb}$. A similar excess as observed in $\bar{p}p$, γp and $\gamma\gamma$ interactions is now also seen in ep scattering.

In order to subject the theory to more refined tests, for example by measuring differential distributions, or to extend the probed phase space, more efficient ways of tagging beauty quarks are necessary, which becomes possible by making use of the CST information also in hadronic decay channels. This approach is followed in the thesis work of I. Foresti.

7.4.2 Update on high Q^2 data

The analyzed e^-p data taken in 1998 and 1999 at a center-of-mass energy of 320 GeV correspond to an integrated luminosity of 15.3 pb^{-1} . From these data inclusive single and double differential cross sections for neutral and charged current in the range of four-momentum transfer squared Q^2 between 200 and 30 000 GeV^2 , and Bjorken x between 0.0032 and 0.65 are extracted [30]. When these data are compared with our measurements of the inclusive neutral and charged current e^+p cross sections clear evidence is observed for neutral current parity violating Z^0 exchange and the structure function F_3 can be extracted. The data are found to be in good agreement with Standard Model predictions (see Fig. 7.9).

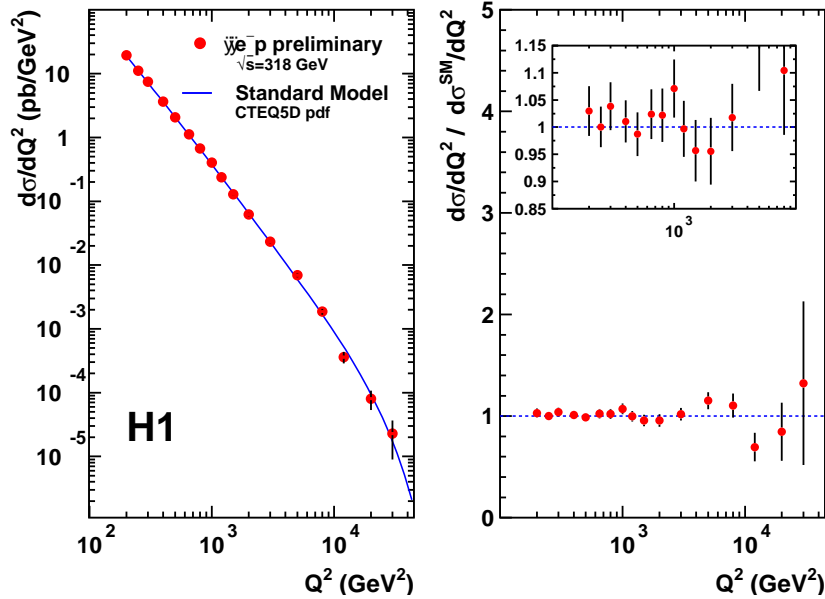


Figure 7.9: Differential cross sections $d\sigma/dQ^2$ at 318 GeV centre-of-mass energy for $e^-p \rightarrow e^-X$. The H1-data are compared to Standard model expectations using the CTEQ5D [34] parton density functions. (Extracted from ref. [31])

The same data are also used to search for eq contact interactions associated to scales not directly accessible at HERA [31]. For conventional contact interactions lower bounds can be set on eq compositeness scales Λ^\pm at 1.6 – 9.2 TeV and on leptoquarks with a ratio mass over coupling M/λ of 0.3 – 1.7 TeV. A search for low scale gravitational effects through the exchange of Kaluza-Klein excitations of gravitons in models with large extra dimensions results in lower limits on the effective Planck scale M_S of 0.63 TeV and 0.93 TeV for positive and negative coupling, respectively.

The inclusive e^+p single and double differential cross sections measured in 1999 and 2000 in the same range of x and Q^2 were also analyzed. The data set corresponds to an integrated luminosity of 45.9 pb^{-1} . The cross-sections are compared to previous H1 results based on 35.6 pb^{-1} of data taken in 1994 to 1997 at $\sqrt{s} = 300 \text{ GeV}$ in Fig. 7.10. The new measurements are found to be fully consistent with previous ones and well described by next-to-leading order QCD fits in the framework of the Standard Model [32], as is apparent in Fig. 7.11.

The search for W boson production in the process $ep \rightarrow eWX$, with subsequent W decay into electrons or muons, has been continued using an integrated luminosity of 13.6 pb^{-1} in e^-p scattering and 81.6 pb^{-1} in e^+p scattering [33]. The analysis has been tuned to maximize the acceptance of W ($W \rightarrow e\nu$, $W \rightarrow \mu\nu$) boson production, and reject other

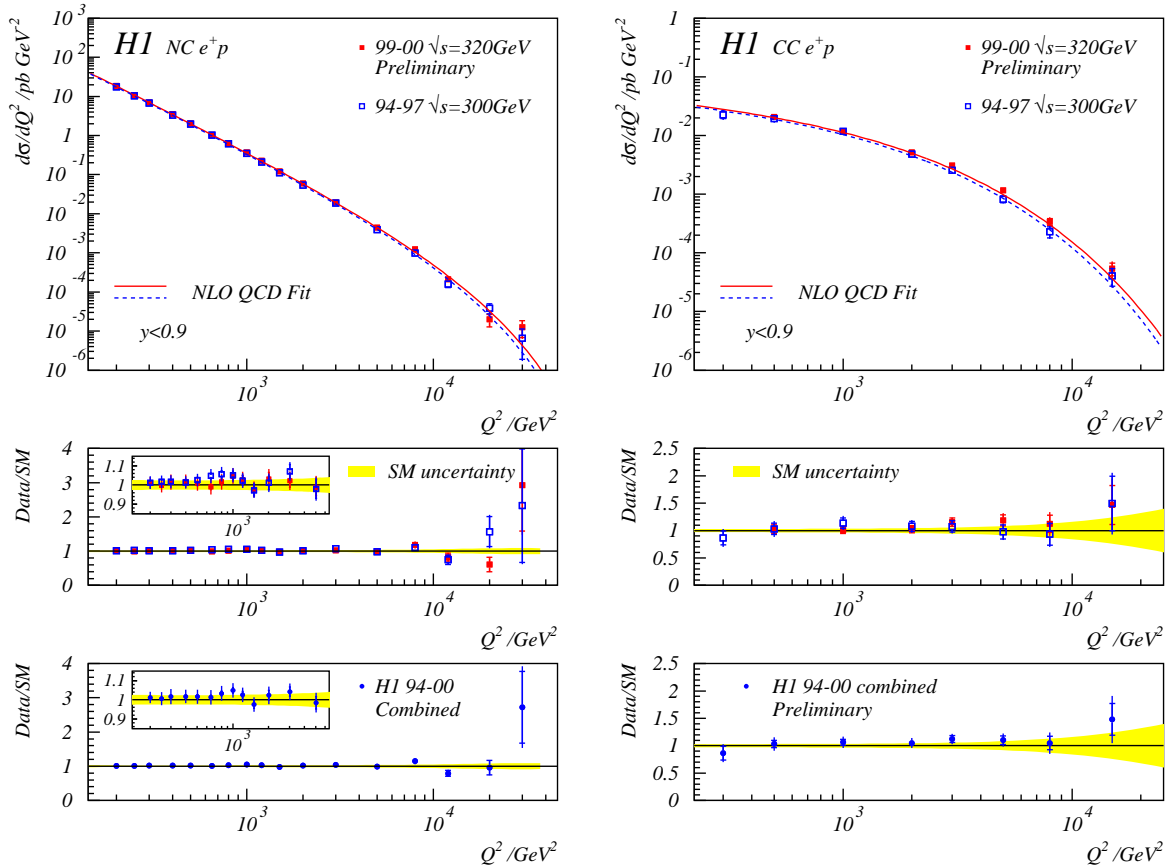


Figure 7.10: The Q^2 dependence of the neutral current (NC,left) and charged current (CC,right) cross sections $d\sigma/dQ^2$ is shown for the new (1999/2000, solid points) and the old (1994/7, open points) measurements. The lines indicate the results of a next-to-leading order QCD fit based on the pre-1997 H1 data, dashed at $\sqrt{s} = 300$ GeV and full for $\sqrt{s} = 320$ GeV. The ratio between data and Standard model fit is shown in figures (b) and (c). The latter includes both old and new data.

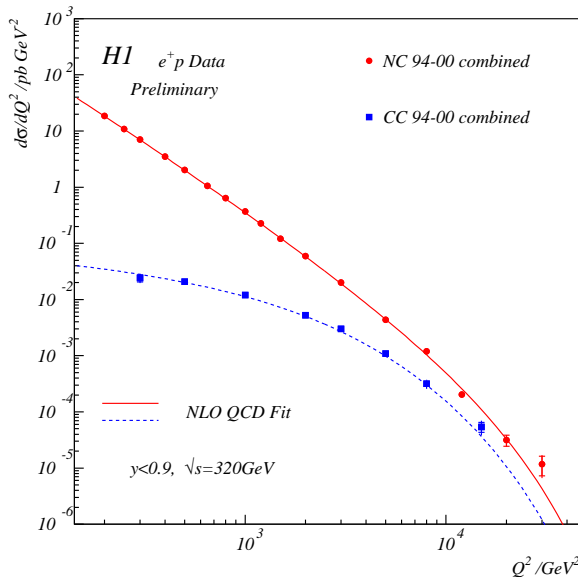


Figure 7.11: The Q^2 dependence of the neutral current (NC) and charged current (CC) cross sections $d\sigma/dQ^2$ is shown for the combined 1994 - 2000 data. The lines indicate the results of a next-to-leading order QCD fit based on the pre-1997 H1 data.

Standard Model processes like the charged and neutral current processes $ep \rightarrow \nu X; \rightarrow eX$, respectively or lepton pair production in $\gamma\gamma$ interactions. In e^-p interactions no events are observed, consistent with the expectation of the Standard Model in this low luminosity sample of 1.46 ± 0.30 (0.32 ± 0.09) for the e (μ) sample. In the e^+p data 14 events are seen, six in the electron and eight in the muon channel compared to an expectation of 6.14 ± 1.46 and 2.01 ± 0.54 , respectively, or 8.2 ± 2.0 when taken together dominated by W production (6.4 ± 1.9). The excess above the expectation is mainly due to events with transverse momentum of the hadronic system greater than 25 GeV where 9 events are found compared to 2.3 ± 0.6 expected. Four of these events are observed in the latest data sample.

References

- [1] *Measurement of Transverse Energy Flow in Deep-Inelastic Scattering at HERA*, H1-Coll., C. Adloff *et al.*, Eur. J. Phys. **C12** (2000), 595.
- [2] *Measurement of Neutral and Charged Current Cross Sections in Positron-Proton Collisions at Large Momentum Transfer*, H1-Coll., C. Adloff *et al.*, Eur. J. Phys. **C13** (2000), 609.
- [3] *Investigation of Power Corrections Event Shape Variables Measured in Deep-Inelastic Scattering*, H1-Coll., C. Adloff *et al.*, Eur. J. Phys. **C14** (2000), 255; addendum *ibid.* **C18** (2000), 417.
- [4] *Search for Compositeness, Leptoquarks and Large Extra Dimensions in eq Contact Interactions at HERA*, H1-Coll., C. Adloff *et al.*, Phys. Lett. **B479** (2000), 358.
- [5] *Measurement of Di-jet Cross Sections in Photoproduction and Photon Structure*, H1-Coll., C. Adloff *et al.*, Phys. Lett. **B483** (2000), 36.
- [6] *Elastic Photoproduction of J/Ψ - and Y -Mesons at HERA*, H1-Coll., C. Adloff *et al.*, Phys. Lett. **B483** (2000), 23.
- [7] *Elastic Φ -Meson Production at HERA*, H1-Coll., C. Adloff *et al.*, Phys. Lett. **B483** (2000), 360.
- [8] *Inclusive Photoproduction of Neutral Pions in the Photon Hemisphere at HERA*, H1-Coll., C. Adloff *et al.*, Eur. J. Phys. **C18** (2000), 293.
- [9] *A Search for Excited Fermions at HERA*, H1-Coll., C. Adloff *et al.*, Eur. J. Phys. **C17** (2000), 567.
- [10] *Di-jet Production in Charged and Neutral Current ep Interactions at High Q^2* , H1-Coll., C. Adloff *et al.*, DESY 00 – 143, hep-ex 0010016, Eur. J. Phys. **C** (2001), in print.
- [11] *Measurement and QCD Analysis of Jet Cross Sections in Deep-Inelastic Positron-Proton Collisions at \sqrt{s} of 300 GeV*, H1-Coll., C. Adloff *et al.*, DESY 00 – 145, hep-ex 0010054, Eur. J. Phys. **C** (2001), in print.
- [12] *Diffractional Jet-Production in Deep-Inelastic e^+p Collisions at HERA*, H1-Coll., C. Adloff *et al.*, DESY 00 – 174, hep-ex 0012051, Eur. J. Phys. **C** (2001), in print.
- [13] *Deep-Inelastic Inclusive ep Scattering at Low x and a Measurement of α_s* , H1-Coll., C. Adloff *et al.*, DESY 00 – 181, hep-ex 0012053, *subm. to Eur. J. Phys. C*.

- [14] *Measurements of Neutral and Charged Current Cross Sections in Electron-proton Collisions at High Q^2 at HERA*, H1-Coll., C. Adloff *et al.*, DESY 00 – 187, hep-ex 0012052, Eur. J. Phys. **C** (2001), in print.
- [15] *Searches at HERA for Squarks in R-Parity Violating Supersymmetry*, H1-Collaboration, C. Adloff *et al.*, DESY 01 – 021, hep-ex 0102050. subm. to Eur. J. Phys. **C** (2001).
- [16] H1-contributions to Int. Cong. on High-Energy Physics (ICHEP 2000), Osaka, Japan; available at <http://www-h1.desy.de/h1/www/publications/conf/list/ICHEP2000.html>
- [17] A. Vollhardt, *Entwurf und Bau einer Frontend-Steuerung für das CIP-Upgrade Projekt für H1 bei HERA*, Diploma Thesis, January 2001.
- [18] M. Urban, *Ein schneller Trigger für H1 bei HERA*, Diploma Thesis, May 2000.
- [19] J. Becker, *The Data Acquisition and Control System for a Fast Trigger at H1*, Diploma Thesis, November 2000.
- [20] V. Blobel, *Linear Least Squares Fits with a Large Number of Parameters*, Universität Hamburg (1999).
- [21] H1 Coll., S. Aid *et al.*, Nucl. Phys. **B545** (1999), 21.
- [22] S. Hengstmann, Nucl. Phys. (Proc.Suppl.) **B79** (1999), 296.
- [23] H1 Coll., C. Adloff *et al.*, Phys. Lett. **B467** (1999), 156.
- [24] CDF Coll., F. Abe *et al.*, Phys. Rev. Lett. **71** (1993) 2396, Phys. Rev. **D53** (1996), 1051; D0 Coll., S. Abachi *et al.*, Phys. Rev. Lett. **74** (1995) 3548, Phys. Lett. **B370** (1996), 239.
- [25] M. Acciarri *et al.*, L3-Coll., preprint hep-ex/0011070; OPAL Coll., *Beauty particle production in photon-photon scattering at LEP2*, presented at ICHEP2000, Osaka, Japan, 2000.
- [26] E. L. Berger *et al.*, preprint hep-ph/0012001.
- [27] *The H1 Silicon Vertex Detector*, D. Pitzl *et al.*, Nucl. Instrum. Meth. **A454** (2000), 334.
- [28] *Open charm and beauty production at HERA* F. Sefkow, Proc. 30th Int. Conf. on High Energy Physics (ICHEP 2000), Osaka, Japan, July 2000, hep-ex 0011034.
- [29] T. Sloan, talk presented for the H1-Coll. at Moriond-QCD 2001, March 2001
- [30] *Measurement of Neutral and Charged Current Cross-Sections in Electron-Proton Collisions at High Q^2* , contr. # 971 in ref. [16].
- [31] *Search for Compositeness, Leptoquarks and Large Extra Dimensions in e^-q and e^+q Contact Interactions at HERA*, contr. # 951 in ref. [16].
- [32] *Inclusive Measurement of Deep Inelastic Scattering at high Q^2 in Positron-Proton Collisions at HERA*, contr. # 975 in ref. [16].
- [33] *W production in ep collisions at HERA*, contr. # 974 in ref. [16].
- [34] CTEQ-Coll., H.L. Lai *et al.*, Phys. Rev. **D55** (1997), 1280; hep-ph 9701256, hep-ph 9903282.

8 Particle Physics at DESY/HERA (HERA-B)

P. Robmann, S. Steiner, O. Steinkamp, P. Truöl and T. Walter

in collaboration with:

the Universities of Heidelberg and Siegen and 31 further institutes from outside Switzerland

(Hera-B collaboration)

In last years annual report [1] we have reported in detail on the status of the Hera-B experiment, its goals, and on the motivation for our modest participation in this experiment. Since the experiment is still in the debugging phase, and our contributions to its development only minor - all of us have predominantly been occupied with other projects - we will keep the report on these aspects short, and concentrate on the only part of the Hera-B experiment, to which we have made contributions, the inner tracker (ITR).

With the completion of the thesis of T. Walter [2] our own research and development project concerning the development of microstrip gas chambers (MSGC) with gas electron multiplier (GEM) foils, has come to an end. We will, however, continue to contribute the maintenance, repair and replacement of defect MSGC's within the ITR, and are for this purpose supervising, as in the past, the production at the laboratories of IMT (Masken und Teilungen), Greifensee.

The present status of the inner tracking system is as follows: During the run period 2000 the stations in front of the ring imaging Čerenkov (RICH) (see Fig. 8.1) have been installed,

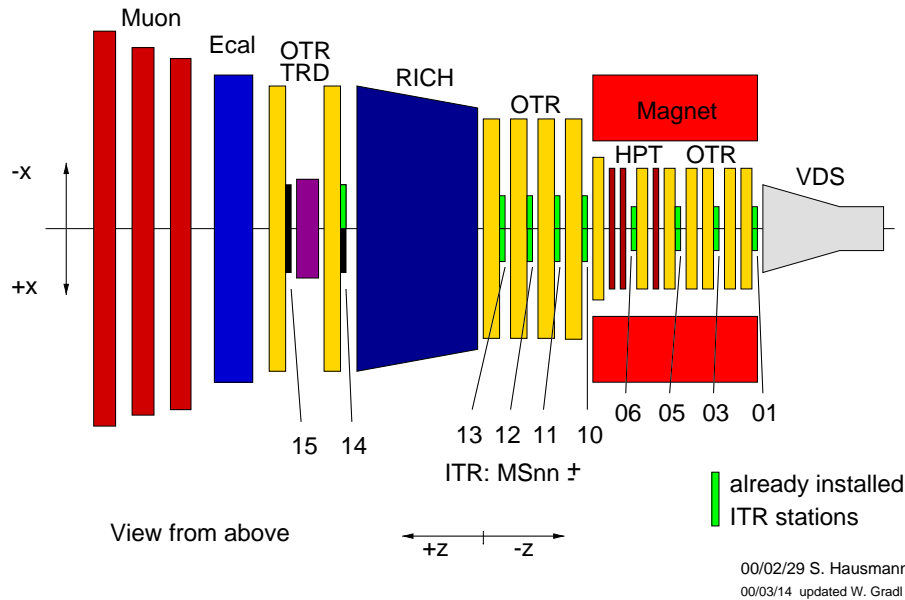


Figure 8.1: Hera-B - tracking components. OTR: Outer tracker; ITR: inner tracker, VDS: silicon tracker. The inner tracker stations, which already have been installed are labeled MSnn, with nn = 01...15.

commissioned and finally routinely operated for a period of 6 - 8 weeks stably at target rates of 5 to 20 MHz with efficiencies between 90% and 96% (see Figure 8.2). These levels were reached after careful training during target operation. The drift and then the GEM voltages were slowly raised over a period of typically one week. This led to a continuous reduction of

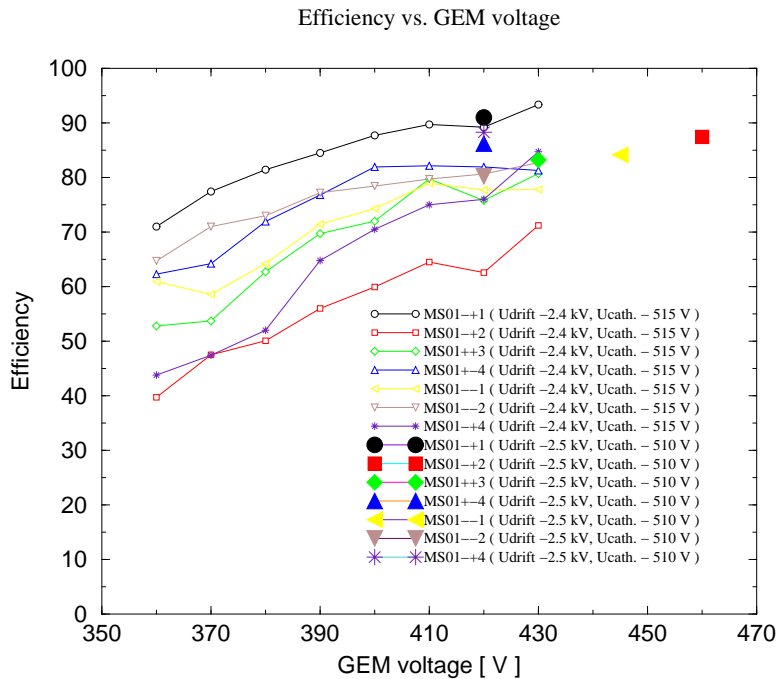


Figure 8.2: *Efficiency curves of MSGC MS01 versus GEM-foil voltage for fixed cathode voltage of 510 V. The filled symbols show the efficiencies for the current voltage settings after individual gain adjustments.*

the number of GEM sparks and subsequent trips. With a gas mixture of Ar/CO₂ (70%/30%) all detectors are first operated with a cathode voltage of 510 V and a GEM voltage of 420 V. With these settings the detector pulse height and gas gain varies up to a factor of 2.5 between different detectors, due to variations of the GEM gain of unknown origin. Individual GEM voltage adjustment is therefore necessary to equalize response.

The ITR was not yet used in the first level trigger because the threshold could not be lowered enough to get acceptable efficiency. In August 2000 a new trigger setup was tested in Hera-B with three detectors using improved grounding and reduced voltage swing of the trigger outputs. This allowed efficient triggering under realistic beam conditions. Part of the improvements are based on the results of tests performed at PSI, which are described in the thesis of T. Walter [2].

During the shutdown 2000/1 the ITR undergoes major revisions, part of which are already completed, namely: All detectors are equipped with improved grounding to minimize baseline fluctuations and noise levels. Detectors with major defects were replaced, weak points of detectors were eliminated like some high voltage cable connections and protection diodes which were damaged. All anodes which produced shorts (about one in 2 detectors) were cut at the fan-in.

All detectors in the trigger stations will be equipped with new HELIX frontend boards using HELIX 1.3a chips. These have full pipeline length, an improved current source which is not oscillating and they can be reliably read out with a readout clock frequency up to 30 MHz. This way the readout can be done with minimal deadtime up to first level trigger rates of 90 kHz.

The calibration and alignment have been carried out for the 2000 data. The procedures are established to do it fast in the coming running period again. The construction program is an integral part of the overall Hera-B reconstruction. The code is also implemented in the second level trigger filter. Major problems were observed in 2000 with the stability of the readout system and online sparsification. The biggest problem were frequent failures of the low voltage power supplies. All of them have been modified in the meantime to

improve protection and reliability. Online sparsification is still under investigation and will be gradually improved.

A complete account of the status of the Hera-*B* experiment at the end of the run (autumn 2000) is contained in reference [3]. This is the status, which was reported to the DESY program review committee. This report was critically reviewed by the committee, which arrived at the following conclusion:

The original aim of the Hera-*B* experiment, which has been approved in 1995, has been the study of the question, why the universe consists mainly of matter although in the big bang matter and anti-matter had been produced equally. Experimentally the CP violation of B mesons is measured. It has been clear from the beginning, that the experiment would be very difficult and that detectors with unprecedented radiation hardness would have to be developed. Unexpected difficulties during this development resulted in delays. In parallel with Hera-*B* special electron-positron storage rings, each with one detector, have been developed in Japan and in the USA. They have already presented first results towards the CP violation of B mesons. Therefore the DESY PRC (Physics Research Committee) concluded in October 2000, that Hera-*B* would not be competitive with these experiments. On this basis and considering the critical manpower situation at DESY, the DESY EWR (Extended Scientific Council) recommended an orderly termination of Hera-*B* in the near future.

Further evaluations within the collaboration and presentations made to the DESY directorate, including an alternative physics program for the next two years, resulted in January of this year in the approval by the DESY directorate of the revised physics program. The relevant statement reads as follows:

The Hera-*B* collaboration has presented a revised physics program for the next two years and detailed plans for detector improvements, the running of the experiment and organisation of data and physics analysis. The collaboration has in this way taken into account the recommendations of the PRC and the EWR. The data and first results will be available by the end of 2002. The continuation beyond 2002 requires a detailed re-evaluation of the scientific potential of the Hera-*B* experiment.

The planned physics program covers open questions of strong interaction physics and rare decays of charmed quarks. Central themes are: the measurement of the B cross section in proton-nucleus interactions, the study of the production of charmonium states and the Drell-Yan production of lepton pairs, as well as the search for rare charm decays like $D^0 \rightarrow \mu^+ \mu^-$. This physics program can be performed essentially with the detector in its present state and the manpower available in the collaboration.

The collaboration wants to demonstrate with this physics program, that Hera-*B* is a powerful precision spectrometer for the study of rare decays of charm and beauty.

References

- [1] Physik-Institut, Universität Zürich, Annual Report 2000/1, available at <http://www.physik.unizh.ch/jb/2000>.
- [2] *Contributions to the Development of Microstrip Gas Chambers (MSGC) for the Hera-B experiment*, Thesis T. Walter (February 2001).
- [3] *Hera-B, Report on Status and Prospects*, 330 p; Executive Summary, 31 p; available at <http://www-hera-b.desy.de/general/publications/hb2k/>.
- [4] Talk given by the spokesman at PRC, DESY, October 2000, available at http://www-hera-b.desy.de/general/talks/prctalk/prc_Oct00.ps.gz.

9 High-precision CP-violation Physics at LHCb

R. Bernet, P. Sievers, O. Steinkamp, U. Straumann, D. Wyler, M. Ziegler

in collaboration with the inner tracking group of LHCb:

University of Lausanne; Max Planck Institute, Heidelberg, Germany; University of Santiago de Compostela, Spain; Budker Institute for Nuclear Physics (INP), Novosibirsk, Russia and Ukrainian Academy of Sciences, Kiev, Ukraine.

The full LHCb collaboration consists of 50 institutes from the countries Brazil, China, Finland, France, Germany, Italy, Netherlands, Poland, Romania, Russia, Spain, Switzerland, Ukraine, United Kingdom.

(LHCb)

9.1 Introduction

LHCb is a second generation experiment on b quark physics which will run from the beginning of the LHC (Large Hadron Collider) operation at CERN (around the year 2006). The production rate of B -mesons will be about three orders of magnitude larger than in all preceding B - physics experiments.

The goal of the experiment is to make systematic measurements of CP violation and rare decays in the B -meson system with unprecedented precision. By measuring CP violation in many different decay modes of B_d , B_s and B_c mesons and comparing the results with the predictions from the Standard Model, the experiment will open a new and very sensitive window for searching for new physics.

The Zurich group concentrates on development, construction, operation and data analysis of the inner tracking part of this experiment. The present research and development phase is done in close collaboration with the particle physics group of the university of Lausanne and should result in a technical design report by the end of 2001.

U. Straumann is project leader for the inner tracking system within the LHCb collaboration and is thus a member of the technical board of LHCb. Olaf Steinkamp leads the silicon task force for developing the silicon microstrip option for the inner tracking system. Furthermore he is a member of the LHCb editorial board, which has to ensure that coherent and correct publications are produced by the LHCb collaboration.

9.2 CP – Violation in the B Meson system: recent developments

The interest in the study of CP – violation in the B System, and its relevance for understanding fundamental interactions, in particular its role in the evolution of the early universe (Baryogenesis) have been elucidated in detail in the previous annual report.

The CP violation effects, expected in the standard model of particle physics, are usually discussed in terms of so-called unitarity triangles, graphical representations of the 6 equations describing the unitarity of the quark mixing matrix V_{ij} (CKM matrix), resulting from the weak interactions of the quarks. For a review of the present knowledge of these triangles see [3].

Recently two experiments on the observation of CP violation in the B system have published results on $\sin 2\beta$, where $\beta \equiv \arg[-(V_{cb}^* V_{cd})/(V_{tb}^* V_{td})]$ is an inner angle of one of these unitarity triangles. The values obtained, by measuring the time dependent asymmetry in the

decays of B_d^0 and \bar{B}_d^0 into $J/\psi K_S$ are:

$$\sin 2\beta = \begin{cases} 0.34 \pm 0.20(\text{stat}) \pm 0.05(\text{syst}) & \text{BaBar [1]} \\ 0.58^{+0.32}_{-0.34}(\text{stat})^{+0.09}_{-0.10}(\text{syst}) & \text{Belle [2]} \end{cases}$$

These results can be compared with a recent analysis in the standard model, assuming the unitarity of the CKM quark mixing matrix and making use of the following experimentally accessible quantities: the CP violation parameter of the Kaon system $|\epsilon_K|$, the ratio of the two CKM elements responsible for b quark decay rates $|\frac{V_{ub}}{V_{cb}}|$, and the oscillation frequencies of the neutral B_d and B_s - Mesons Δm_d and Δm_s . (The status of the mixing and oscillation measurements are summarized in a recent review [4]). The resulting standard model prediction is [3]

$$\sin 2\beta_{\text{SM}} = 0.67 \pm 0.17. \quad (9.1)$$

Whereas the more accurate result of BaBar is lower by 1.2σ (adding all errors quadratically) the Belle result with its larger errors is in perfect agreement with the standard model.

To use the B system as a probe for new physics requires much higher accuracy. Supersymmetry, for instance, will mainly affect rare processes which in the standard model involve quark loop diagrams in lowest order already. New Physics may lead to inconsistencies between channels that are redundant in the standard model so all relevant CKM phases should be measured directly, with the highest precision possible.

In spring 2000 the results of a one year workshop on physics at LHC were published. The study group for B Decays at LHC [5] was able to show, that specially from channels which allow direct measurement of the angle $\gamma = \arg V_{ub}$, LHCb will provide a unique facility to explore the various CP violating modes. Examples are $B_s \rightarrow J/\psi K_s$ and $B_s \rightarrow D_s K$, which need a very good eigentime resolution of the decaying B_s , or $B \rightarrow \pi K$ and $B_{d(s)} \rightarrow D_{d(s)}^+ D_{d(s)}^-$, which can only be isolated with reliable particle identification, as provided by the RICH system of LHCb.

9.3 Development of an inner tracking detector for LHCb

The inner tracking setup, which is presently being discussed, deviates considerably from the one described in the technical proposal [11]. On the basis of results from extensive R&D on various different micro-pattern gas detectors as well as background simulation studies with realistic beam pipe assumptions the inner tracking group decided in February 2000 to concentrate on triple GEM gas and silicon microstrip detectors and drop all other gas micro-pattern technologies which proved unstable in high density hadronic beams. Detailed design studies for an implementation of the remaining two technologies and prototype construction are presently going on.

9.3.1 Triple GEM option

Our group in Zurich has built a full-size prototype of a triple GEM detector and has measured all its relevant properties. We have shown, that the triple GEM is a stable and robust detector with spark probabilities much below 10^{-10} , which provides enough safety margins in the operating parameters to be used as an inner tracking technology of LHCb. First results had been mentioned already in the last years annual report. The final analysis of the measurements on the pulse height distributions, detection efficiencies, geometrical cluster size, position resolution, detector homogeneity w.r.t. to signal size and performance as a function of incident angle have been published in [6] and [7].

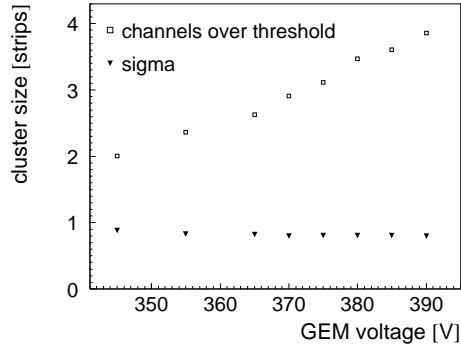


Figure 9.3: Cluster width for perpendicular tracks as a function of detector gain. Shown are the mean number of channels above a threshold of 3.5 times the noise (σ) and the width of a Gaussian fit to the pulse shape. The pitch of the readout strips is $300 \mu\text{m}$.

As an example, the analysis of the cluster-size is worth mentioning in this report. Two different methods were used, a simple counting of number of adjacent channels above a fixed signal to noise ratio and a Gaussian fit to the signal amplitude versus channel position. Figure 9.3 shows the resulting values as a function of the GEM voltage, which determines the total gas amplification. A typical operating point is $V_{\text{GEM}} = 370 \text{ V}$. The Gaussian width of the clusters does in fact not depend on the detector gain. The value of $\sigma = 0.8$ strip pitches ($240 \mu\text{m}$) is consistent with an estimate [8], based only on the transverse diffusion ($D_t \approx 300 \mu\text{m}/\sqrt{\text{cm}}$ for a gas mixture of Ar:CO₂ = 70:30) of the charged cloud along an average drift path of 4.5 mm. The GEM foils thus do not influence the cluster size.

Large cluster sizes increase the channel occupancy of the detector, which is a major limitation of such a device in the LHCb environment. Electrons and positrons generated in the beam pipe may pass the inner tracker with large incident angles corresponding to even larger clusters, increasing the occupancy further.

Because of these rate effects it seems unlikely, that the inner tracking of LHCb will be a pure triple GEM solution. Since triple GEM detectors have the advantage over silicon microstrip devices, that larger sensor planes can be built with smaller number of readout channels a mixed solution may turn out optimal. We also expect shifts in the boundaries between inner and outer tracking, to be determined in on-going simulation studies.

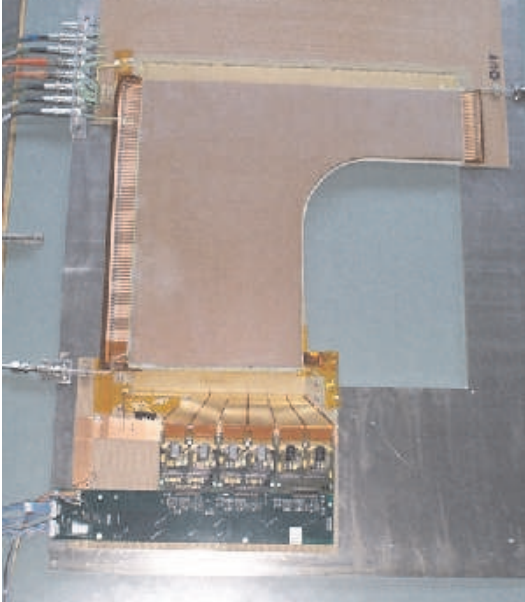


Figure 9.4: A full size triple GEM prototype suitable for tracking station 7 to 10. It measures 415 mm in height and 430 mm in width (active detector area). Two such “L” shape detectors would be mounted around the beam pipe, allowing to measure two coordinates (x, u). On the bottom electronics readout boards bonded to the detector can be seen. These consist of HELIX chips, which have a similar front-end behaviour as the foreseen Beetle chips.

A new full size triple GEM prototype with correct geometry for LHCb, suited for one

of the tracking stations 7 to 10 has been constructed (see Fig. 9.4) in cooperation with the university of Lausanne. The device is presently being studied in the laboratory, and beam tests will start soon. It has a new readout board, with much lower capacity, allowing to run the detector at lower gain (see the conclusion in [6]).

9.3.2 Silicon microstrip option

The importance of the silicon solution has increased, mainly due to the higher backgrounds from the beam-pipe. Silicon is considered to be a realistic option despite its higher costs and slightly larger radiation length.

We foresee an arrangement of silicon detectors in ladders, which will be mounted vertically. The conical beam pipe of LHCb makes it necessary to have different arrangements for each of the 11 tracking stations. We plan to use only one sensor type, with an active size of 100 mm length, 90 mm width and readout strip pitch of 235 μm . Such a sensor can be produced on a 6 inch wafer and is similar to those used in the CMS tracking system. It is almost identical to the silicon detectors used in the satellite GLAST². A possible layout of such a system we described in [9]. The same time a more realistic definition of the space requirements and positions of the different tracking stations was provided [10].

22 prototype sensors with 67 mm strip length and different strip width have been designed and built at the company DETECTOR in Kiev, Ukraine. They consist of 63 strips with a pitch of 240 μm . We are currently constructing ladders of different length for performance measurements at particle beams at PSI (high rate) and CERN (large momentum to measure position resolution) soon.

We also have started to install in Zurich the relevant equipment for silicon microstrip detector development and tests: a manual wedge bonding machine from Devotek, type 5425, is used to connect electronics to the detectors, both for the triple GEM prototypes and for the silicon microstrip detectors. It will also be used to combine several sensors into longer ladders.

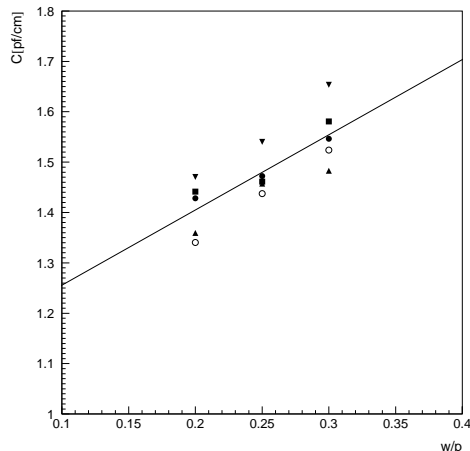


Figure 9.5: Total strip capacitance as a function of the ratio implant width to strip pitch (w/p), measured at a depletion voltage of 75 V and a frequency of 1 MHz. The different markers belong to different detectors. A linear fit to all points yields an average systematic dependence of $C_{\text{tot}} = 1.49 \times \frac{\text{width}}{\text{pitch}} + 1.11$ [pF/cm].

A new manual wafer probe station from the company Karl Suss, type PM5, in connection with an existing impedance analyzer HP 4192A was used to measure the electrical characteristics of prototype sensors. Figure 9.5 shows the total strip capacitance for our prototype detectors for different width and pitch geometries. For each detector a dependence of the

²see www-glast.stanford.edu/

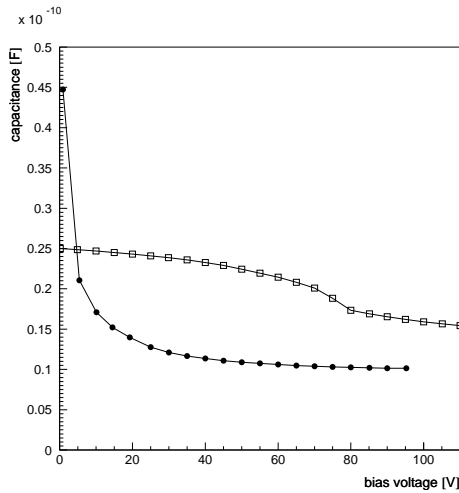


Figure 9.6: *Capacitance versus depletion voltage of a silicon detector prototype. Filled points before irradiation, open squares after irradiation with a maximum of 10^{14} protons.*

ratio width/pitch can be observed, however the variation from detector to detector seems to be at least as large as the width over pitch effect.

Figure 9.6 shows the capacitance as a function of the depletion voltage. Before irradiation the detectors show a decrease of the capacitance with voltage and the full depletion is reached at about 50 V. After irradiation the capacitance is increased. Further investigations are ongoing to try to understand the performance of the irradiated detectors and the possible implications of the higher capacitance on the readout electronics.

We also have studied a first version of the readout chip to be used in LHCb (Beetle from ASIC Laboratory in Heidelberg), connecting it to a silicon microstrip detector and observing the signals from radioactive sources. A crucial question is the dependence of the pulse shape on the load capacity at the input of the amplifier, since we intend to build long silicon ladders, with total capacitance of the order of 20 to 30 pF. The measured pulse shapes (Fig. 9.7) are relatively wide, however seem to be acceptable. This pulse shape data is used in the LHCb simulation software to determine the additional occupancy by particles originating in neighbouring bunch crossings of LHC (so called spill over), which occur with a period of 25 ns.

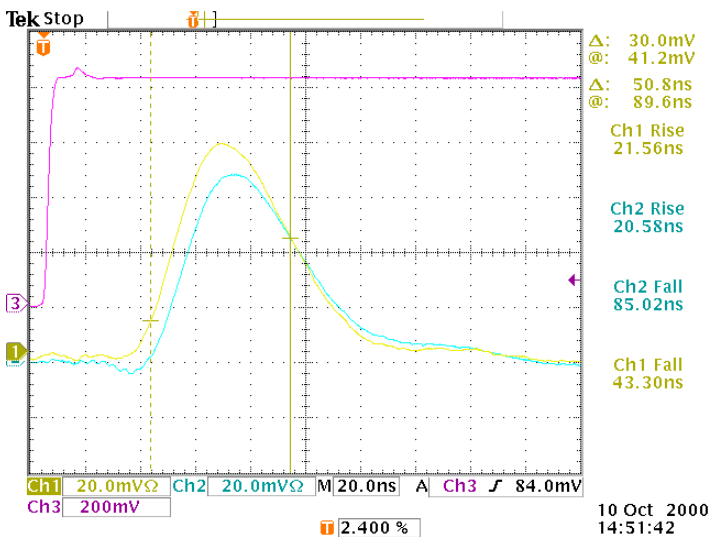


Figure 9.7: *Signal from the front end stage of a Beetle prototype chip, using a pulser to simulate a charged particle signal (upper signal) and SMD capacities of 22 and 33 pF (middle and lower signal, respectively) to simulate a large silicon detector.*

9.4 Other collaboration activities

9.4.1 Hardware developments

An essential part of the dipole spectrometer to be realized in LHCb is its magnet, which should provide enough magnetic field to reach the momentum resolution anticipated in the experiment. For the Technical Proposal [11] a window-frame dipole magnet with super-conducting coils and horizontal pole faces had been assumed. Contacts with industry revealed, that the complicated shape of the coils and the high magnetic forces would lead to high cost and mechanical risks. LHCb has therefore moved to the design of a warm magnet. The new magnet is described in a technical design report [14], which was accepted by the CERN LHCC and all relevant committees.

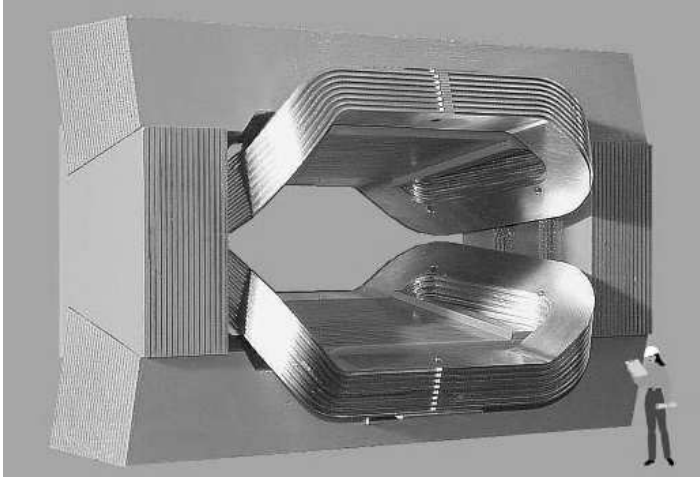


Figure 9.8: *Sketch of the LHCb magnet*

To reduce electrical power requirements to about 4.2 MW, the pole faces are shaped to follow the acceptance of the experiment (Fig. 9.8). The total bending power amounts to $\int Bdl = 4 \text{ Tm}$ over a total track length of 10 m. The useful aperture is 2.6 m x 2.2 m, increasing along the beam axis to 4.2 m x 3.5 m, fitting the acceptance shape of the experiment. The coils will be made of Aluminum (AL-99.7) and the total weight of the magnet will be about 1500 tons.

A market survey has been performed by CERN, resulting in 4 firms interested in the conductor production, 7 firms for the coil winding and 16 firms for the yoke production. The magnet will be ordered soon, and the financial contribution from the swiss FORCE pool is well received for this purpose.

In the year 2000 technical design reports both on the calorimeters [12] and the RICH [13] were well received by the CERN program committee LHCC and construction of these detectors can start now.

9.4.2 Software

All LHCb data processing applications are being built using the LHCb software framework, GAUDI. The latest releases allow simulated events stored in the old ZEBRA format to be read and new data to be written using an object oriented persistence tool taken from the ROOT package, a general object oriented analysis tool. Other new components include a structured description of the detector and its geometry, and support for statistical data e.g. histograms. Work is now in progress to extend the framework in many specialized areas, such as integration with the new object oriented GEANT4 simulation package, the addition of components for

managing calibration and alignment data, the development of a visualization framework and analysis tools. A new LHCb reconstruction program, called BRUNEL, has been developed that is based on the above mentioned object oriented framework “GAUDI”, but uses most of the existing physics algorithms written in FORTRAN. At the same time much effort has gone into developing new algorithms, redesigned using object oriented methods and written in C++. This new code is gradually being incorporated into BRUNEL with the aim of eventually producing a reconstruction program that conforms entirely to an object oriented design.

In the Zurich group we have started to use parts of these simulation packages to predict the behaviour of the proposed inner tracking design and optimize its parameters.

References

- [1] BaBar Collaboration, B. Aubert *et al.*, hep-ph/0102030 (submitted to Phys. Rev. Lett.).
- [2] Belle Collaboration, A. Abashian *et al.*, hep-ph/0102018 (submitted to Phys. Rev. Lett.).
- [3] A.J. Buras, hep-ph/0101336;
- [4] Colin Gay: *B-mixing*, Ann. Rev. Nucl. Part. Sci. (2000) 50:577-641
- [5] P. Ball, R. Fleischner, G.F. Tartarelli, P. Vikas, G. Wilkinson *et al.*, *B decays at LHC*, CERN-TH/2000-101, hep-ph/0003238.
- [6] M. Ziegler, P. Sievers and U. Straumann, *A triple GEM detector with two dimensional readout*, hep-ex/0007007 and LHCb internal note LHCb-2000-056, July 2000.
- [7] M. Ziegler, P. Sievers and U. Straumann, *A triple GEM detector with two dimensional readout*, Proceedings of the International Conference on Imaging Techniques in the borderlands of High Energy Physics, Astrophysics, Nuclear Physics, Medicine and Biology (Imaging 2000), 28 June - 1 July 2000, Stockholm, submitted to Nucl. Instr. and Meth.
- [8] P. Cwetanski, *Studies on detector prototypes for the inner tracking system of LHCb*, Diplomarbeit Heidelberg, März 2000.
- [9] O. Steinkamp, *A Possible Layout of an Inner Tracker Silicon Detector*, LHCb-2000-109, November 2000.
- [10] O. Steinkamp: *Space Requirements and z Positions for Tracking Stations*, LHCb-2000-108, November 2000.
- [11] LHCb Collaboration: *LHCb technical proposal*, CERN LHCC 98-4, Feb. 20, 1998.
- [12] LHCb Collaboration: *LHCb Calorimeter, Technical Design Report*, CERN/LHCC/2000-036, Sep. 6, 2000.
- [13] LHCb Collaboration: *LHCb RICH, Technical Design Report*, CERN/LHCC/2000-037, Sep. 7, 2000.
- [14] LHCb Collaboration: *LHCb Magnet: Technical Design Report*, CERN/LHCC/2000-007, Dec. 17, 1999.

10 Particle Physics with CMS

C. Amsler, R. Kaufmann, H. Pruyss, C. Regenfus, P. Riedler[‡],
P. Robmann, T. Speer, and S. Steiner

in collaboration with:

ETH-Zürich, Paul Scherrer Institut (PSI), Universität Basel and the CMS Collaboration.

(CMS Collaboration)

[‡] now at CERN, Geneva, Switzerland

10.1 Introduction

Our group is participating in the design and construction of the silicon pixel detectors for the CMS experiment at CERN's LHC, which is scheduled to start operations in spring 2006 at an energy of $\sqrt{s} = 14$ TeV. We shall concentrate on issues related to the heavy b and t quarks. The physics programme with CMS is focused on the Higgs boson(s) and on the supersymmetric (SUSY) particles, expected in the ~ 1 TeV mass range. The B physics programme is centered on the search and measurement of CP-violation through the decays $B_d^0 \rightarrow J/\psi K_s$, $B_d^0 \rightarrow \pi^+ \pi^-$ and $B_s^0 \rightarrow J/\psi \phi$, the measurement of B_s^0 mixing, and searches for flavor changing neutral currents decays. The study of B -baryon decay and the spectroscopy of B hadrons could also be undertaken.

The identification of b -jets is crucial both to select signal events and to reject background events; b -jets will be used to identify top quarks, the standard model Higgs boson and SUSY particles. Due to the long lifetime of B mesons, b -jets can be identified by looking for tracks not pointing to the primary vertex (i.e. with large impact parameters). Trajectories have to be measured with a high precision that depends on the distance of the first detected point from the interaction vertex, and on the point resolution. It is thus crucial that the first detector layer be located as close as possible to the primary interaction vertex, bearing in mind the high radiation which the pixel detectors will have to withstand. The high rate requires a fine detector granularity and also developments using radiation hard technology.

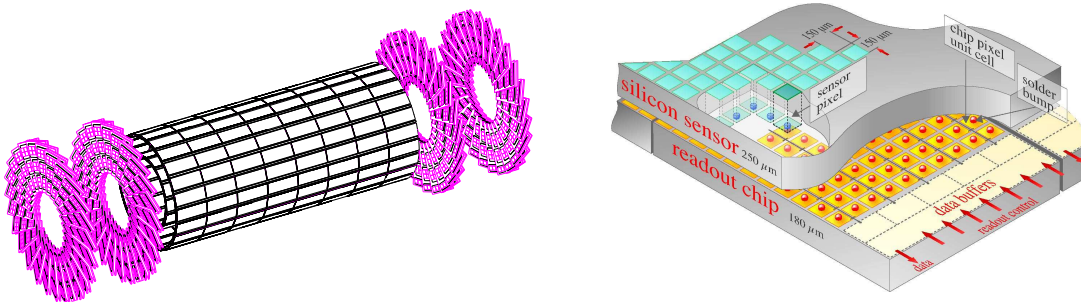


Figure 10.1: a): Perspective view of the CMS pixel detector. b): schematic view of a pixel detector element. Each sensor pixel is connected via an indium solder bump to a pixel unit cell on the readout chip which amplifies the signal. The hit data are stored on the edge of the chip where they wait for trigger confirmation.

The pixel detector envelope extends from 3.7 to 21 cm radially and from -50 to 50 cm in beam direction. The detector is made of three cylindrical layers, 53 cm long, with radii of 4, 7 and 11 cm (Fig. 10.1a). The layers contain some 3×10^7 silicon pixels. The pixel modules consist of thin, segmented sensor plates with highly integrated readout chips connected with

the indium bump bonding technique (see Fig. 10.1b). A sensor plate contains 53×52 pixels, each with a surface area of $150 \times 150 \mu\text{m}^2$. The analogue signals are read out to determine the coordinates more accurately, using charge sharing between adjacent pixels. A double column of pixels forms an independent readout unit controlled by a circuit sitting in the periphery. The chips are connected through bond wires to hybrid circuits, which collect the data signals and distribute the readout control and clock signals. Capton cables connected to the hybrids transmit the signals to and from the outer region of the pixel system frame which contains detector control chips and electro-optical converters for optical signal transmission.

We have worked on the design and test of the silicon sensors for the barrel detector [1]. Position resolutions and depletion depths were measured at CERN for various magnetic field configurations [2] and for detectors that had been irradiated with doses equivalent to several years of LHC operation. Full details can be found in previous annual reports, in several diploma works and in ref. [3, 4].

We are also designing and building the mechanical support and cooling structure for the pixel detector in the Institute's workshop, as well as the service tubes which will contain the electrical and cooling lines. All these projects are currently in the R & D phase. During last year most of our hardware efforts were devoted to the commissioning of the ATHENA experiment. We nevertheless studied various pixel designs and studied their performances before and after irradiation in the laboratory, and with a test beam at CERN. We also started to contribute towards simulation and reconstruction for the trackfinder software.

10.2 Test of irradiated pixel sensors

In 2000 we irradiated the pixel sensors ordered earlier from SINTEF (Norway) and CSEM (Neuchâtel). They consist of a $300 \mu\text{m}$ n-type silicon bulk with n^+ pixel implants. The p-n junction was made by implanting a p^+ layer on the sensor backside [5]. In the non-irradiated sensor the depletion zone grows from the p^+ side, but during irradiation, type inversion occurs and the depletion zone then grows from the pixel side. The prototypes from the two vendors were irradiated with $24 \text{ GeV}/c$ protons from the CERN-PS and with $300 \text{ MeV}/c$ pions at PSI. The devices were submitted to various charged particle fluxes, some reaching 6×10^{14} hadrons/ cm^2 , which corresponds to the accumulated dose of the innermost layer after several years of LHC operation.

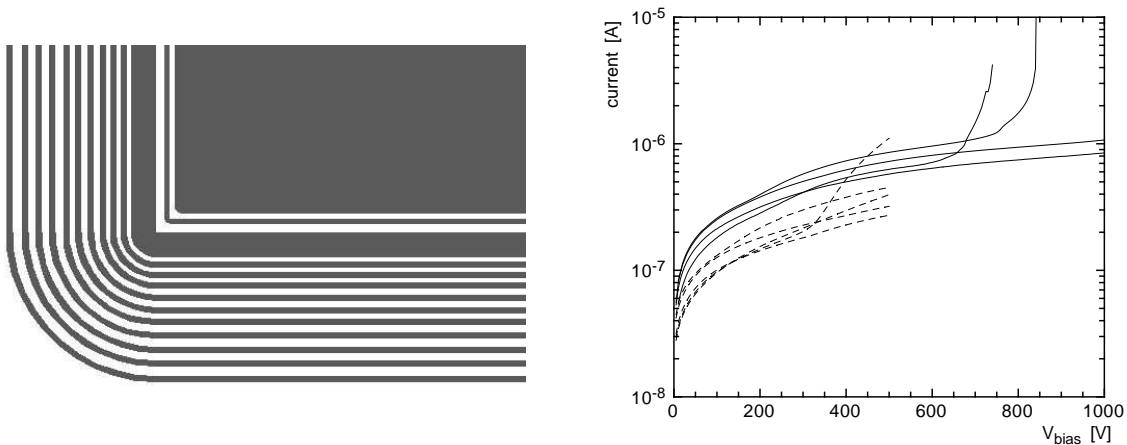


Figure 10.2: *Left: one of the various guard-ring designs. Right: leakage currents of irradiated diodes with different guard ring designs. Full curves: test up to 1 kV, dashed curved: test up to 500 V.*

10.2.1 Guard ring design

The bias voltage needed to guarantee a sufficient depletion depth increases with time due to the accumulation of radiation defects and the sensors will eventually have to withstand a bias voltage of several hundred volts. This requires an advanced guard ring structure around the sensor plate. Different structures have been designed, built and tested after irradiation. One of them is shown in Fig. 10.2 (left).

The leakage-currents of nine different diodes after irradiation with 6×10^{14} hadrons/cm² are plotted in Fig. 10.2 (right), as a function of bias voltage. The surface surrounded by the guard rings was between 1 and 4 mm². From the four devices that were tested up to 1 kV, two sustained 1000 V, whereas two broke down already at 700 V. The other devices were only tested up to 500 V, with only one performing unsatisfactorily below 500 V. In conclusion, a guard-ring structure of the type shown in Fig. 10.2 (left) is suitable for the harsh radiation environment at LHC.

10.2.2 Pixel design

Since the pixels consist of n⁺ silicon in an n-type substrate they have to be insulated. This is normally done with a narrow p⁺-ring around each pixel, called p-stop ring. When the detector is fully depleted the pixels are perfectly insulated against each other. However, a (hopefully small) fraction of pixels will fail, owing to the poor connection with the readout chip through the indium bump. The accumulation of charge on these pixels will lead to a local breakdown through the narrow gap to the read-out chip, generating a dead cluster around the faulty pixel. This can be avoided by reducing the resistance between the pixels, for instance with the atoll structure and small openings in the p-stop rings shown in Fig. 10.3 (left). The long paths through the maze provide enough resistance, yet allow the accumulated charge to flow in a controlled way. Simulations show that the inter-pixel resistance should be at least a few MΩ in order not to influence the fast signal-charge collection.

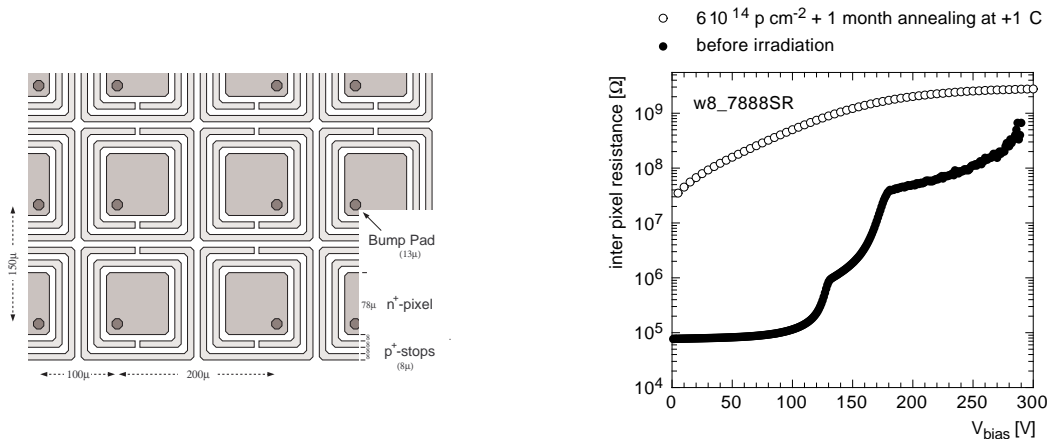


Figure 10.3: *Left: Pixel layout with atoll-like open double p-stop rings. Right: Interpixel resistance as a function of bias voltage, before and after irradiation, for a device with only one open p-stop ring.*

Figure 10.3 (right) shows the resistance between one pixel and all of its neighbours for a device with only one open p-stop ring, before and after irradiation. The full depletion voltage of the non-irradiated device was 140 V. The quite different shape of the irradiated curve is due the bulk type-inversion. The resistance after irradiation has increased by several

orders of magnitude and is in the range of $\sim 1 \text{ G}\Omega$. Figure 10.4 shows the behaviour of the inter-pixel resistance as a function of fluence (time integrated hadron flux). The maximal fluence of $6 \times 10^{14} \text{ cm}^{-2}$ corresponds roughly to a dose of $2 \times 10^5 \text{ Gy}$.

The inter-pixel resistance decreases at low fluencies but increases dramatically at higher doses. The low fluence behaviour could be explained by the build-up of an electron accumulation layer at the surface on the pixel-side. At higher doses the influence of surface defects (reduced surface mobility, interface traps, etc) over-compensates for the effect of the accumulated charge and lead again to an increase in resistance.

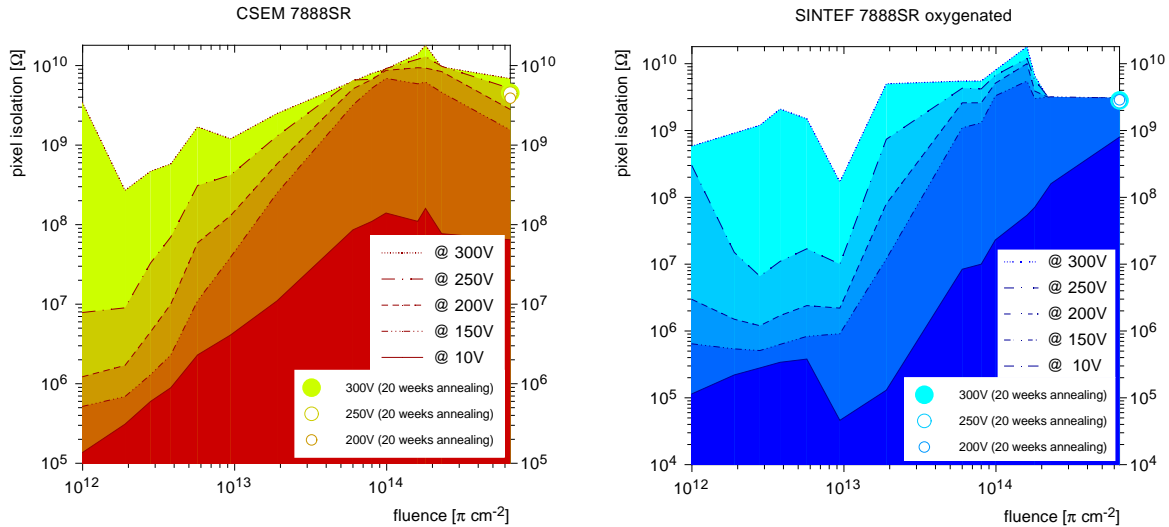


Figure 10.4: *Inter-pixel resistance as a function of pion fluence for a typical CSEM device (left) and an oxygenated SINTEF device (right), both with one open p-stop ring.*

10.2.3 Oxygenated silicon pixels

Recently, the CERN RD48 collaboration (also known as ROSE-collaboration) demonstrated that a high oxygen concentration in the silicon bulk can increase the radiation hardness of detectors. In fact, it reduces the so-called β factor, which denotes the introduction rate of negative space charge after type inversion [6]. In Fig. 10.4 there is no dramatic difference between the high dose inter-pixel resistances of a CSEM and an oxygenated SINTEF device, and therefore oxygenation does not influence significantly the surface defects. However, the smaller β factor is still useful, as it reduces the full depletion voltage $V(FD)$ after irradiation. Several diodes were irradiated with pions at PSI to measure $V(FD)$ and the doping concentration N_{eff} . After a fluence of $6 \times 10^{14} \pi \text{ cm}^{-2}$, $V(FD)$ was about 190 V for the oxygenated device, which corresponds to $N_{eff} = 2.8 \times 10^{12} \text{ cm}^{-3}$. However, $V(FD)$ was much higher for the non-oxygenated device ($> 400 \text{ V}$), leading to $N_{eff} > 6 \times 10^{12} \text{ cm}^{-3}$.

10.2.4 Beam tests

In summer 2000 a preliminary readout chip (DM_PSI38), designed by our PSI colleagues in radiation hard DMILL technology, and fully equipped with bump bonded sensors, was submitted to a beam test at CERN. We used the 220 GeV/c pion beam H2 produced with the SPS proton beam. Figure 10.5 shows a remarkable Landau pulse height distribution for events from one pixel only. Since the chip was used in self-triggering mode, the noise peak is cut off.

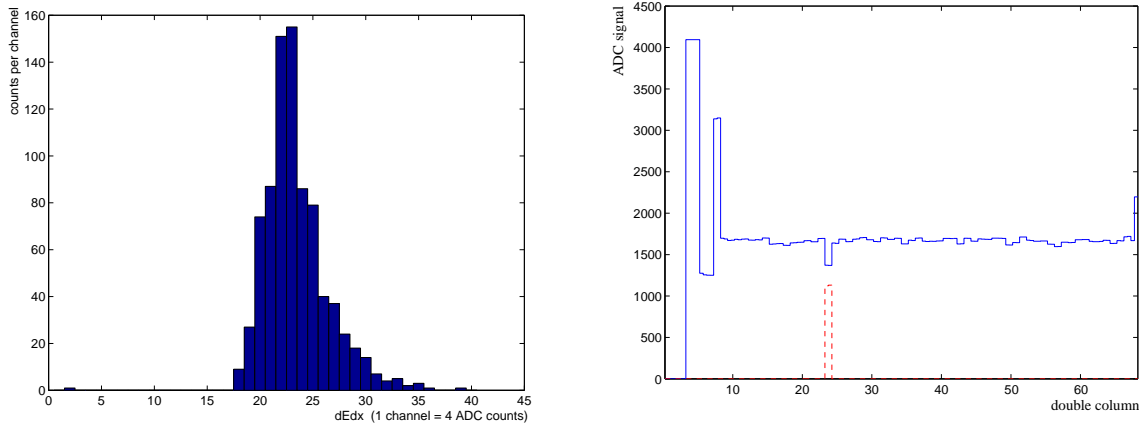


Figure 10.5: *Left: Pulse height distribution from one pixel only, taken with 220 GeV/c pions. Right: Output signal distribution from the DM_PSI30 chip showing a signal from the bump bonded pixel. The whole double column was read out after a pixel hit (see text).*

A single event registered with our sensors by the DM_PSI30 chip is shown in Fig. 10.5 (right). The continuous line shows the contents of the analogue cells of one double column. The first analogue signals (up to count 8 on the horizontal axis) consist of time stamps and column address. The analogue values of the 60 pixels of one double column are displayed above $x=9$. The dashed signal marks a pixel with analogue signal above threshold. At $x = 23$ a clear analogue signal from pixel 14 can be seen, confirmed by its digital output.

To optimize the atoll design and in an attempt to increase the breakdown voltage after irradiation, we will design and order a last batch of pixel sensors with various p-stop geometries, before a final decision is taken in 2002. One possible way to remove the accumulated charge would be to implant a uniform p-layer on the surface (p-spray technique). On the other hand, we have shown that the current layout is already adequate for several years of LHC operation.

10.3 Tracking at CMS: the combinatorial forward Kalman filter

With the high luminosity of the LHC, the challenge of track reconstruction is to reliably find tracks in a high density environment, where low luminosity events will feature around 5000 hits and high luminosity events ten times more. With this high number of hits, combinatorial problems can be severe, and the challenge is to find for each track the correct combination of hits, while limiting the number of spurious combinations leading to ghost tracks in a reasonable amount of time.

Tracks usually leave between 8 and 15 hits in the tracker (pixel and silicon detectors), according to their rapidity. However, some of these hits may be missed, due for example to detector inefficiencies. The track reconstruction algorithm has therefore to exclude bad hits, for example background hits near the tracks, and accommodate layers without hits.

Several algorithms were studied for CMS in the past [3]. In the new object-oriented reconstruction framework (ORCA), the first method to be pursued is the combinatorial forward Kalman filter. The Kalman filter was extensively used in high energy physics experiments [7]. In the combinatorial Kalman filter only one track is reconstructed at a time, starting from an initial trajectory. It is a recursive procedure to estimate the track parameters from a set of reconstructed hits, taking into account the random perturbation of the particle trajectory due to the material traversed. The filter proceeds iteratively from the innermost tracker

layer towards the outer layers, starting from a coarse estimate of the track parameters and including the information of the successive detection layers, one by one.

The first step is the construction of the initial trajectories, called *seeds*. These are composed of two hits in two pixel layers and the beam crossing region. In the present algorithm, any combination of two pixel layers are used, and seeds are constructed for every pair of hits pointing to the the beam crossing region and a specified minimum transverse momentum.

In the next step, track candidates are grown from each seed: the initial seed trajectory is extrapolated to the next layer, according to the expected motion in the magnetic field, accounting for multiple scattering and energy loss in the traversed material. On the new layer several hits may be compatible with the extrapolated trajectory and thus several trajectories are constructed, each time with a different hit. An additional trajectory candidate is created, in which no measured hit is used, to account for tracks with no hit on that particular layer. All trajectory candidates are then grown in turn to the next layer, and the procedure is repeated until the outer layer of the tracker is reached. To avoid a bias, the trajectory candidates are grown in parallel and, to limit the number of combinations, only the candidates with the best χ^2 are kept. Each seed usually leads to a large number of mutually exclusive trajectories which are partly composed of the same hits. A subset of compatible candidates, based on the number of hits shared and the track qualities, is therefore selected to resolve hit assignment ambiguities.

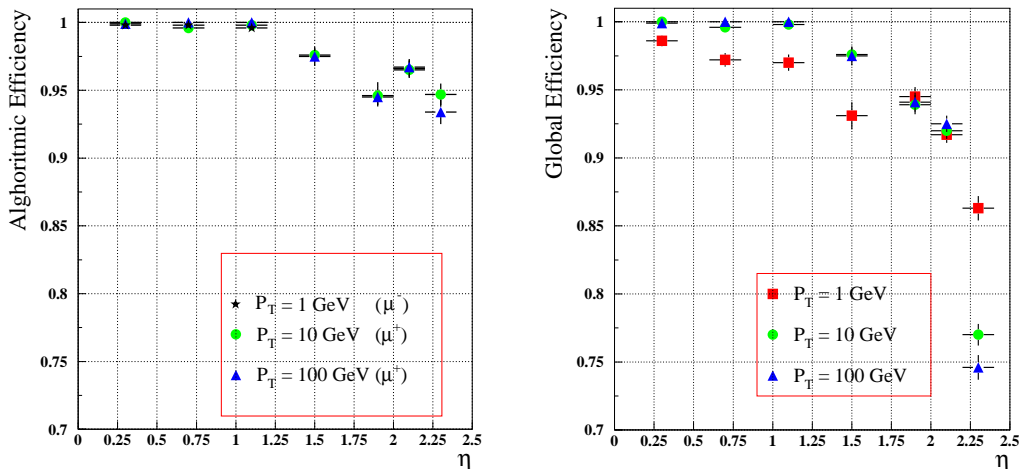


Figure 10.6: *Algorithmic (left) and global (right) track reconstruction efficiencies in single muon events, as a function of pseudo-rapidity η .*

Currently, a reconstructed track is required to have a minimum of 8 hits, with a hit missing in at most one layer. Two definitions are used for the track reconstruction efficiency. The *algorithmic* efficiency corresponds to tracks which have at least 8 hits in the tracker, among them at least 2 in the pixel detector. The *global* efficiency is the reconstruction efficiency for all tracks. In addition to the algorithmic efficiency, it also includes the acceptance, hit efficiency and any other factor influencing reconstruction. It mainly differs from the algorithmic efficiency in the forward region due to the loss of coverage.

The algorithmic and global track reconstruction efficiencies for single muon events are shown in Fig. 10.6. In the central region ($|\eta| < 1$) the algorithmic efficiency is nearly 100%. In the $|\eta| > 1$ region, the current algorithmic efficiencies of all samples are between 92% and

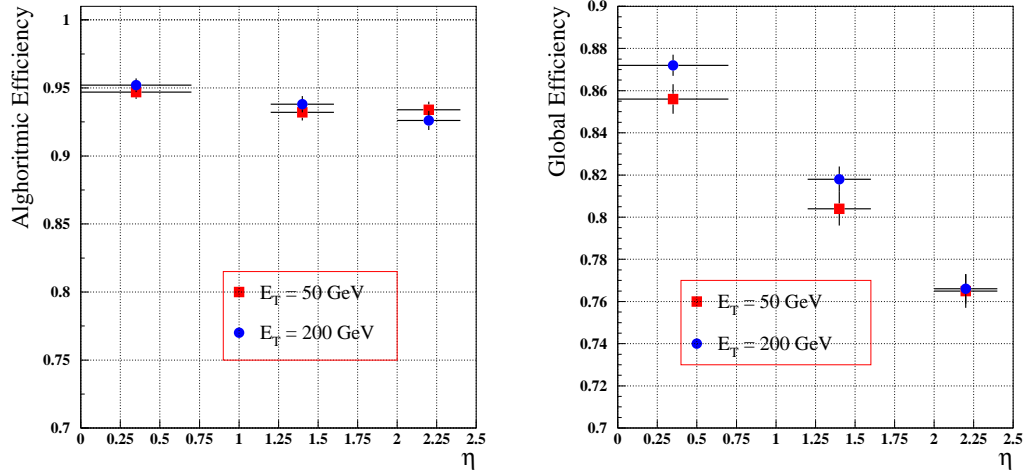


Figure 10.7: *Algorithmic (left) and global (right) track reconstruction efficiencies in $b\bar{b}$ jet events.*

97%. This somewhat low efficiency has been traced to shortcomings in the simulation.

The algorithmic and global track reconstruction efficiencies for $b\bar{b}$ jet events are shown in Fig. 10.7. The pseudo-rapidity bins correspond to the axis of the jets, and not to that of individual tracks.

Since no inefficiency related to the algorithm itself was found, the present effort is on improving the speed of the reconstruction (seed and trajectory building). At full luminosity, the large number of hits in the pixel layers leads to a very large number of seeds which do not grow into real tracks. Methods to reject spurious combinations as quickly as possible are being studied.

References

- [1] R. Kaufmann, PhD thesis, in preparation
- [2] V. Dubacher, Diplomarbeit, Universität Zürich (1996); R. Kaufmann, Diplomarbeit, Universität Zürich (1997); M. Glättli, Diplomarbeit, Universität Zürich (1998)
- [3] Technical Design Report of the CMS Tracker, CERN/LHCC 98-6 (1998)
- [4] R. Kaufmann and B. Henrich, Proc. of the ENDEASD Workshop, Santorin (1999) and Nucl. Instr. and Methods in Phys. Research A (in print)
- [5] G. Bolla, D. Bortoletto, C. Rott, A. Roy, S. Kwan, C. Chien, H. Cho, B. Gobbi, R. Horisberger, K. Gabathuler, R. Kaufmann: Design and Test of Pixel Sensors for the CMS Experiment, Nucl. Instr. and Methods in Phys. Research A (in print)
- [6] M. Moll, E. Fretwurst, G. Lindström (ROSE Collaboration), Nucl. Instr. Meth. in Phys, Res. A 439 (2000) 282
- [7] R. Frühwirth, Nucl. Instr. Meth. in Phys. Research A 262 (1987) 444

11 Superconductivity and Magnetism

H. Keller, J. Hofer (until June 2000), R. Khasanov, M. Mali, P. Morf,
 R. Pircher (since March 2001), R. Renggli, J. Roos, A. Schilling, Ph. Schneider (since
 January 2001), A. Shengelaya, G.M. Zhao, S. Zech-Döttinger (until July 2000),
 V.A. Ivanshin (visiting scientist),
 T. Schneider (Titularprofessor), and K.A. Müller (Honorarprofessor)

in collaboration with:

ETH Zürich (J. Karpinski), Paul Scherrer Institute (E. Morenzoni, K. Conder, A. Furrer),
 IBM Rüschlikon Research Laboratory (C. Rossel), Max Planck Institut für Festkörperforschung,
 Stuttgart (H.-U. Habermeier), University of Birmingham (E.M. Forgan), University
 of St. Andrews (S.L. Lee), Loughborough University (A. S. Alexandrov), University of Oxford
 (S.J. Blundell), Rutherford Appleton Laboratory (F.L. Pratt), Institut Max von Laue-
 Paul Langevin, Grenoble (R. Cubitt), Kazan State University (M.V. Eremin, A.V. Dooglav,
 B.I. Kochelaev), University of Belgrade (I.M. Savić), Institute of Low Temperature and Struc-
 ture Research, Polish Academy of Sciences, Wroclaw (P.W. Klamut), University of Maryland
 (R. L. Greene), Argonne National Laboratory (G.W. Crabtree), Northern Illinois Univer-
 sity, DeKalb (B. Dabrowski), University of Houston (C. W. Chu), NEC Research Institute,
 Princeton (S. Bhattacharya).

11.1 Introduction

In the previous year we have continued and extended our studies of the fundamental physical properties of high-temperature superconductors (HTS) and related magnetic systems. One main research project involves detailed oxygen isotope ($^{16}\text{O}/^{18}\text{O}$) effect (OIE) studies on various physical quantities and phenomena (critical temperature, in-plane penetration depth, resistivity, charge and spin dynamics, stripe formation) in these systems in order to explore the role of lattice effects in cuprate systems. In another project, we have continued our investigation of the magnetic, electronic and thermal properties of HTS, that we have started several years ago. A great advantage of our work is the application of complementary experimental techniques, such as muon-spin rotation (μSR), nuclear magnetic resonance (NMR), nuclear quadrupole resonance (NQR,) electron paramagnetic resonance (EPR), together with bulk SQUID and torque magnetometry measurements, resistivity, and thermal measurements. The scientific merit of this work is to gain new information on the relevant physical properties of HTS and related systems which may help to clarify the nature of high-temperature superconductivity.

11.2 Studies of oxygen isotope effects

11.2.1 Oxygen isotope effects in manganites

Despite tremendous experimental efforts [1], the basic physics and the microscopic mechanism for the colossal magnetoresistance (CMR) in doped manganites remain controversial [2, 3, 4]. Several theoretical investigations [2, 3] indicate that in the paramagnetic state the electron-phonon coupling constant λ is large enough to form small polarons while the growing ferromagnetic order increases the bandwidth and thus decreases λ sufficiently to form a large polaron metallic state. On the other hand, Alexandrov and Bratkovsky [4] have recently argued that the model suggested by Millis *et al.* [2] cannot quantitatively explain CMR, and thus proposed an alternative CMR theory. The basic idea of their model is that the small polarons form localized bound pairs (bipolarons) in the paramagnetic state, while

the competing exchange interaction of the polaronic carriers with localized spins drives the ferromagnetic transition. The transition is accompanied by a giant increase in the number of small polarons which are mobile carriers and move coherently at low temperatures. This model appears to be able to explain the CMR quantitatively.

In order to discriminate among those different models, we study the oxygen ^{16}O vs. ^{18}O isotope effects on the transport properties in several doped manganites. The OIE on the intrinsic resistivity was obtained from high-quality epitaxial thin films of $\text{La}_{0.75}\text{Ca}_{0.25}\text{MnO}_3$ and $\text{Nd}_{0.7}\text{Sr}_{0.3}\text{MnO}_3$. The OIE on the thermoelectric power S was studied in ceramic samples of $\text{La}_{1-x}\text{Ca}_x\text{MnO}_3$, since the grain-boundary effect on S is negligible.

In the low-temperature ferromagnetic state, the intrinsic resistivity of these compounds shows a strong dependence on the oxygen isotope mass. The residual resistivity of the films increases by 15(3)% upon replacing ^{16}O with ^{18}O [5]. In contrast, the thermoelectric power is nearly independent of the oxygen isotope mass [6]. The observed large isotope effect on the resistivity and negligible effect on the thermoelectric power are in quantitative agreement with a theory based on a novel polaronic Fermi liquid [6]. The existence of a polaronic Fermi-liquid state in the ferromagnetic state is also consistent with the CMR theory by Alexandrov and Bratkovsky [4].

In the paramagnetic state, the resistivity data can be well fit by [7]

$$\rho = \frac{A}{\sqrt{T}} \exp(E_\rho/k_B T),$$

where $A = (ah/e^2 \sqrt{k_B}) (1.05 W_p)^{1.5} / \hbar \omega_o$, W_p is the polaron bandwidth, and E_ρ is the activation energy. We found that, upon replacing ^{16}O with ^{18}O , the parameter A decreases by 35(5)%, and E_ρ increases by 13.2(5) meV [7]. The strong isotope dependence of E_ρ is not consistent with a simple small polaron hopping conduction mechanism where E_ρ is nearly independent of the isotope mass. However, this isotope effect is in quantitative agreement with a scenario where immobile bipolarons are formed in the paramagnetic state [7], and thus give a strong support to the CMR theory proposed by Alexandrov and Bratkovsky [4].

11.2.2 Oxygen isotope effects in cuprates

a) Charge and spin dynamics in $\text{YBa}_2\text{Cu}_4\text{O}_8$ studied by NMR/NQR

Recently we performed high accuracy ^{63}Cu NQR spin-lattice relaxation and SQUID magnetization measurements on ^{16}O and ^{18}O exchanged $\text{YBa}_2\text{Cu}_4\text{O}_8$ and determined the isotope shift of the opening of the spin-pseudogap, T^* , and the superconducting transition temperature T_c . The corresponding isotope exponents are $\alpha_{T^*} = 0.061(8)$ and $\alpha_{T_c} = 0.056(12)$, which are the same within error bars and suggest a common origin for the superconducting and the spin-pseudogap [8]. This result is in contrast to a recent study [9] which reported the absence of an OIE in the pseudogap of $\text{YBa}_2\text{Cu}_4\text{O}_8$ as determined by ^{89}Y Knight shift. To resolve this controversy we decided to perform high precision Cu Knight shift measurements on the same samples we used in the spin-lattice relaxation measurements. For this purpose we first had to measure accurately on both oxygen exchanged samples the Cu NQR frequency (zero magnetic field), shown in the left part of Fig. 11.8. After orientating the $\text{YBa}_2\text{Cu}_4\text{O}_8$ powder grains in the 9T-magnet and fixing them in epoxy resin, we performed Cu Knight shift measurements for the orientation of the grains with their c-axis perpendicular to the magnetic field. In the right part of Fig. 11.8 we exhibit the final result obtained for the Knight shift after correcting for quadrupolar effects. There is definitely an OIE on the pseudogap determined by the Cu Knight shift. For the corresponding pseudogap energy scale we find values of 239.5 K and 237.4 K for ^{16}O and ^{18}O , respectively. The Knight shift

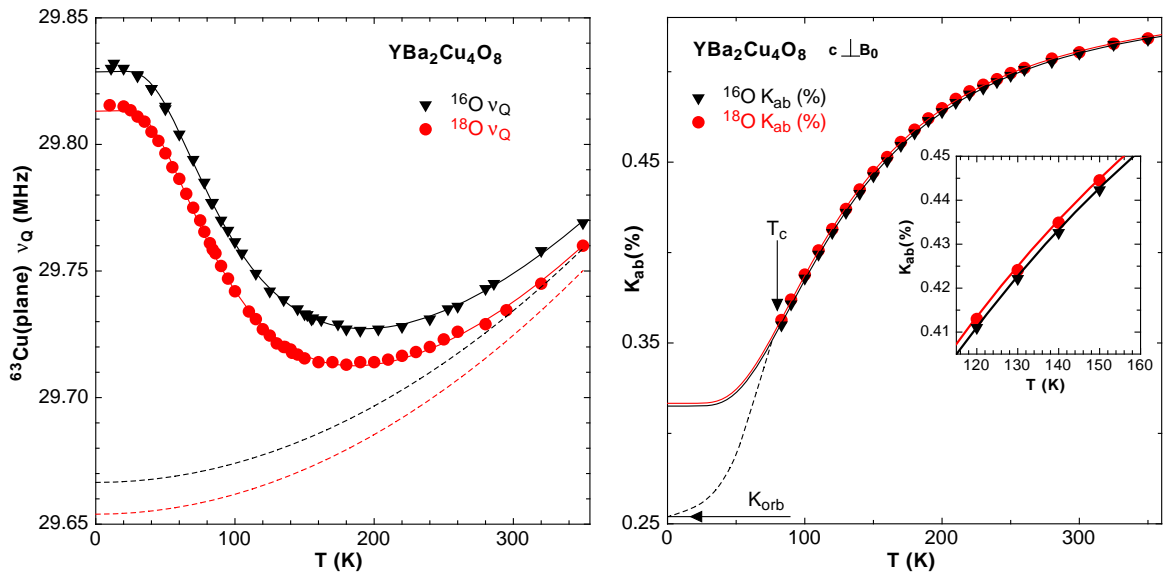


Figure 11.8: *Oxygen isotope effect on NMR and NQR of plane copper in $YBa_2Cu_4O_8$. Left: temperature dependence of the NQR frequency. Right: temperature dependence of the Knight shift.*

isotope exponent amounts to 0.085(44) which is in error bar limits the same as for T^* . Thus we clearly demonstrate that spin-lattice relaxation and Knight shift show the same OIE on the pseudogap with an isotope exponent equal to the one of T_c . Looking closer at the NQR frequency (ν_Q) dependence of ^{16}O and ^{18}O samples (Fig. 11.8) we noticed an additional interesting OIE. Besides the roughly constant 15 kHz shift between the two samples which comes from the difference in the quantum mechanical zero-point displacement and thermal lattice expansion, we observed a strong OIE in the temperatures where the $\nu_Q(T)$ curves have their minima and their largest slopes, respectively. Subtracting from $\nu_Q(T)$ a lattice contribution, corrected for thermal expansion, we end up with a "rest" contribution that has to come from charge redistribution in the CuO_2 plane, presumably connected to the formation of a new pseudogap. Quantifying this "rest" contribution by fitting it with an expression similar to the one used for the Knight shift leads to energy scales of 186.4 K and 177.8 K for ^{16}O and ^{18}O , respectively. The corresponding isotope exponent was found to be 0.45(11) which is quite different from what the spin-pseudogap shows. The NQR frequency involves no spin but charge only, however, all the charges irrespective of what state they occupy. This contrasts the spin-pseudogap as observed by spin lattice-relaxation and by Knight shift where only spins of electrons close to the Fermi surface get involved. However, it is evident from the results shown in Fig. 11.8 that the NQR frequency reveals independent electronic charge features that appear to coexist with the spin-pseudogap and superconductivity.

b) Rare earth ion size effects in LaSrCuO compounds

The OIE on the suppression of the superconducting transition temperature T_c induced by the substitution of La by Eu in the compound $(\text{La}_{1-y}\text{Eu}_y)_{2-x}\text{Sr}_x\text{CuO}_4$ was systematically investigated in the framework of a diploma thesis. For this purpose, a series of samples of $(\text{La}_{1-y}\text{Eu}_y)_{2-x}\text{Sr}_x\text{CuO}_4$ with Sr contents $x = 0.1, 0.15,$ and 0.20 and Eu contents $y = 0.00, 0.05,$ and 0.10 , were synthesized by means of standard solid state reaction sample preparation techniques. The oxygen-isotope exchange $^{16}\text{O} \rightarrow ^{18}\text{O}$ was carried out by Dr.

K. Conder at the Paul Scherrer Institute (PSI) in Villigen, Switzerland. The superconducting

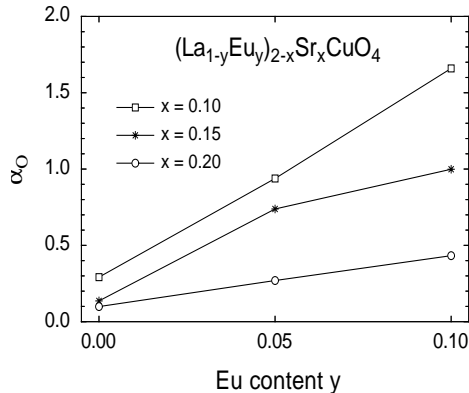


Figure 11.9: Oxygen-isotope exponent α_O of T_c as a function of Eu substitution level in $(La_{1-y}Eu_y)_{2-x}Sr_xCuO_4$ for Sr concentrations $x = 0.10, 0.15,$ and 0.20 . Note that the rate at which α_O increases for the overdoped ($x = 0.20$) samples amounts only $\approx 27\%$ of the rate found in the underdoped ($x = 0.10$) samples, demonstrating the strong doping dependence of the Eu induced enhancement of α_O .

transition temperature T_c and hence its dependence on the Sr and Eu content were determined by magnetic susceptibility measurements. The results are as follows: First, T_c decreases drastically with increasing Eu concentration, whereby the T_c suppression is most efficient in the underdoped regime. Replacement of 10% of La^{3+} (ionic radius $r_K = 114$ pm) by the smaller rare-earth ion Eu^{3+} ($r_K = 95$ pm) reduces T_c below 5 K. Second, the oxygen-isotope exponent α_O of T_c decreases almost linearly with increasing charge carrier concentration, i.e. the OIE is most pronounced in the underdoped regime for all Eu concentrations. Furthermore, α_O increases nearly linearly with increasing Eu content for all charge carrier concentrations (Fig. 11.9). These findings confirm the well known generic trend that α_O is largest for lowest T_c .

Moreover, our results for the Eu induced suppression of T_c are consistent with the physical model, recently proposed for the Nd induced suppression of T_c in $(La_{1-y}Nd_y)_{2-x}Sr_xCuO_4$ [10]. The basic idea of this model involves the buckling of the CuO_2 conduction layers caused by the mismatch between the radii of the rare-earth ions which is responsible for the disappearance of superconductivity in the low temperature tetragonal (LTT) structural phase.

c) Stripe formation and structural phase transitions in LaSrCuO compounds

The observation of alternating spin and charge stripes below a characteristic temperature T^* [11, 12] has added a new feature to the phase diagram of the high-temperature cuprate superconductors. The stripe phase was suggested to be important to the understanding of the pairing mechanism in these materials [13]. However, the microscopic origin of the stripe phase is still a matter of debate. Concerning the high- T_c materials, most studies of the stripe phase were concentrated on 214 compounds with a doping level close to $1/8$. It was shown that in Nd-substituted $La_{1.48}Nd_{0.4}Sr_{0.12}CuO_4$, the stripe phase is static, and no superconductivity is observed [11]. On the other hand, the stripe phase in Nd-free samples (e.g., $La_{1.94}Sr_{0.06}CuO_4$) is dynamic and superconductivity survives [14]. This indicates that Nd substitution has substantial effects on both the dynamics of the stripe phase and superconductivity.

However, it is still not clear how Nd substitution effects the physical properties of the $La_{2-x}Sr_xCuO_4$ system. The complication is associated with the fact that a partial substitution of La by Nd in $La_{2-x}Sr_xCuO_4$ induces a structural-phase transition, which occurs (for 40% substitution) at about 80 K, while the charge stripe formation takes place near 65 K. This complication is even more pronounced in the compound $La_{1.875}Ba_{0.125}CuO_4$, where the structural phase transition is clearly observable at 57 K (see Annual Report 1999/2000), while the charge stripe formation temperature is near 54 K, which renders the two transi-

tions almost indistinguishable. Therefore, it is natural to ask whether these two phenomena are related to each other. If they are related, the OIE on the charge-stripe formation temperature might be caused by the OIE on the structural phase transition temperature or vice versa. In order to clarify the situation, it is necessary to synthesize a compound in which the two transitions occur at clearly distinct temperatures. This condition is fulfilled in the compound $(\text{La}_{0.9}\text{Eu}_{0.1})_{1.875}\text{Sr}_{0.125}\text{CuO}_4$, where the structural phase transition takes place around 120 K, whereby the charge ordering temperature is 65 K [15]. Therefore, the compounds $(\text{La}_{0.9}\text{Eu}_{0.1})_{1.875}\text{Sr}_{0.125}\text{CuO}_4$ containing the oxygen isotopes ^{16}O and ^{18}O were chosen for our studies of the relation between the OIE on the charge stripe formation and the structural-phase transition temperatures.

One of the strongest signatures of a possible stripe formation in the $\text{La}_{2-x}\text{Sr}_x\text{CuO}_4$ system was found in the so-called *wipeout effect* for the ^{63}Cu NQR signal [15]. On cooling the number of ^{63}Cu nuclei contributing to the signal starts to decrease at a certain temperature (even above T_c), which is identified as the onset temperature for stripe formation. At low temperature the signal completely disappears. We performed an OIE study of the ^{63}Cu -NQR-wipeout effect in $\text{La}_{1.875}\text{Ba}_{0.125}\text{CuO}_4$ and $(\text{La}_{0.9}\text{Eu}_{0.1})_{1.875}\text{Sr}_{0.125}\text{CuO}_4$. The results are shown in Fig. 11.10. The wipeout effect is described by a normalized factor F which

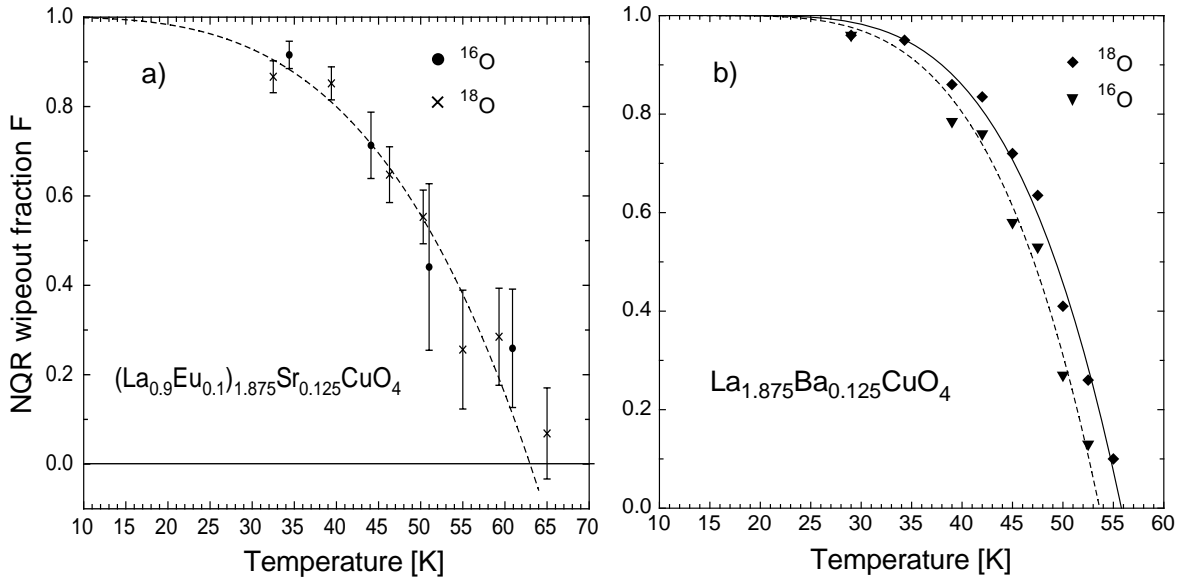


Figure 11.10: *NQR-wipeout effect in $\text{La}_{1.875}\text{Ba}_{0.125}\text{CuO}_4$ and $(\text{La}_{0.9}\text{Eu}_{0.1})_{1.875}\text{Sr}_{0.125}\text{CuO}_4$. The effect is represented by a normalized factor F , as introduced in Ref. [15]. Curves are guides to the eye.*

represents sort of an order parameter for charge stripe formation. The charge stripe formation onset-temperature in $(\text{La}_{0.9}\text{Eu}_{0.1})_{1.875}\text{Sr}_{0.125}\text{CuO}_4$ was found to be 63(2) K, which is in good agreement with the value reported in Ref. [15]. Heat capacity measurements on the identical sample revealed a clearly discernible structural phase transition at 116(2) K, in agreement with 119 K reported in earlier work [16]. However, within experimental errors we have not been able to detect any clear OIE on both transition temperatures.

This is in contrast to the situation in $\text{La}_{1.875}\text{Ba}_{0.125}\text{CuO}_4$, where we observe an oxygen-isotope shift of 2 K on both the structural phase transition around 57 K (from our heat capacity data) and on the charge stripe formation temperature (from our NQR wipeout data in Fig. 11.10b). Hence, the situation in $(\text{La}_{0.9}\text{Eu}_{0.1})_{1.85}\text{Sr}_{0.15}\text{CuO}_4$ is less clear, and we cannot

draw any further conclusions on the microscopic mechanism responsible for the occurrence of the observed phase transition and its dependence on oxygen-isotope exchange.

At this point it should be mentioned that there exists an alternative point of view concerning the interpretation of the NQR-wipeout effect as a measure of stripe order. According to Ref. [17] this effect also could be explained by the glassy nature of the magnetic freezing: slow spin dynamics shorten copper nuclear relaxation times, and these nuclei become unobservable below a threshold value of relaxation times. Because the dynamics is spatially inhomogeneous and the freezing occurs on a wide temperature interval, the NQR signal disappears gradually on cooling.

d) Measurements of the magnetic penetration depth by μ SR

There is increasing evidence that a strong electron-phonon coupling is present in cuprate superconductors, which may lead to the formation of polarons (bare charge carriers accompanied by local lattice distortions) [18, 19]. However, it is not clear whether these normal-state polaronic carriers condense into Cooper pairs in the superconducting state. One way to test this hypothesis is to demonstrate that the effective mass of the supercarriers m^* depends on the mass M of the lattice atoms. This is in contrast to conventional BCS superconductors, where only the ‘bare’ charge carriers condense into Cooper pairs, and m^* is essentially independent of M .

According to the London model the in-plane penetration depth λ_{ab} in cuprate superconductors (clean limit) obeys the simple relation: $\lambda_{ab}^{-2}(0) \propto n_s/m_{ab}^*$, where n_s is the charge carrier density, and m_{ab}^* is the in-plane effective mass of the superconducting charge carriers. Thus a possible mass dependence of m_{ab}^* can be measured by investigating the isotope effect on the penetration depth. Previous OIE studies of the penetration depth in $\text{La}_{2-x}\text{Sr}_x\text{CuO}_4$ indeed showed a pronounced oxygen-mass dependence on the supercarrier mass [20, 21, 22]. However, in all these experiments λ was extracted indirectly, either from the Meissner fraction [20, 21], or from magnetic torque measurements [22].

The μ SR technique is one of the most direct and accurate methods to determine the penetration depth λ in type II superconductors. Detailed μ SR investigations of polycrystalline samples of cuprate superconductors have demonstrated that λ can be obtained from the muon spin depolarization rate $\sigma(T) \propto 1/\lambda^2(T)$, which probes the magnetic field distribution in the mixed state. For highly anisotropic superconductors (like the cuprate superconductors) λ is solely determined by the shortest penetration depth λ_{ab} , and the following relation holds [23]:

$$\sigma(T) \propto 1/\lambda_{ab}^2(T) \propto n_s/m_{ab}^*.$$

In the last year we used transverse-field μ SR in order to study the OIE on λ_{ab} in underdoped powder samples of $\text{Y}_{1-x}\text{Pr}_x\text{Ba}_2\text{Cu}_3\text{O}_{7-\delta}$ with $x = 0.3$ and 0.4 . Preliminary results clearly indicate a pronounced OIE on λ_{ab}^{-2} which increases with decreasing T_c . For $x = 0.3$ and 0.4 the OIE was found to be $\Delta\sigma/\sigma = \Delta\lambda_{ab}^{-2}/\lambda_{ab}^{-2} = -4(1)\%$ and $-7(1)\%$, respectively, in agreement with the recent magnetic torque measurements on $\text{La}_{2-x}\text{Sr}_x\text{CuO}_4$ [22]. These experiments are the first direct demonstration of an OIE on the magnetic penetration depth in a cuprate superconductor, implying that lattice vibrations indeed play a role in high-temperature superconductivity.

11.3 Thermal and transport studies

11.3.1 New developments in instrumentation

An old and very sensitive method to detect phase transitions in solids is the differential-thermal analysis (DTA). It is widely used in chemical sciences for measurements above room temperature. However, recently it has also been used to measure heat capacities of superconductors between 40 K and 300 K [24]. The method is so sensitive that the latent heat of vortex-lattice melting in $\text{YBa}_2\text{Cu}_3\text{O}_{7-\delta}$ could be measured for the first time [25]. We

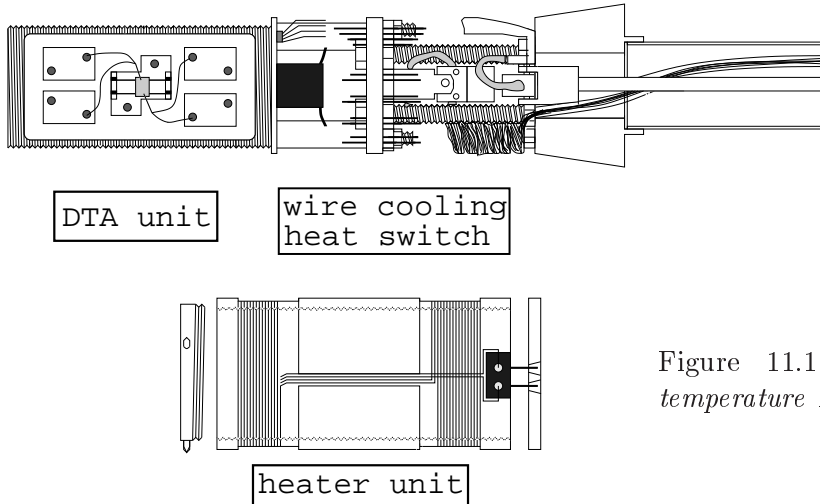


Figure 11.11: *Central part of low-temperature DTA-insert*

extended the DTA method described in Ref. [24] using cryogenic resistance thermometers. With this new setup we achieved a relative accuracy in heat capacity of at least 1 part in 10000 on samples with a mass of typically 20 mg, with a data-point density of 1000 points per Kelvin and higher. The measuring cell, shown in Fig. 11.11, is inserted into a split-coil magnet system that allows us to explore angular dependent properties in an external magnetic field. This is of particular interest for studying anisotropic superconductors at low temperatures which are expected to show a variety of phenomena related to vortex physics. We successfully tested the apparatus on a 16 mg sample of superconducting niobium ($T_c \simeq 9$ K). Since the thermometers are calibrated up to room temperature, the same setup can be used to perform measurements in the temperature range 2.5 K to 300 K. This work was done in the framework of a diploma thesis.

In the context of the technical part of another diploma thesis an independent and fully automated device for electrical four-point transport measurements was designed and built. Two main specifications guided the development of this device: 1) The possibility to quickly stabilize the temperature of the sample within 0.1 K; 2) The minimization of thermal gradients across the sample holder, in order to keep the difference between the temperature at the sensor site and the effective temperature at the sample site as small as possible. In order to comply with these requirements, a whole experimental setup was put on stream, comprising a He flow cryostat, a temperature controller for the sample holder, a cryosorption pump (with automatic nitrogen refill relay circuit), a digital nano-voltmeter, a dc current source, and a measurement computer with IEEE interface card. A *Labview* program performs the readings and settings for the actual four-point measurements and controls the sequence in the temperature profile entered by the user.

Basically, the temperature stabilization process involves the temperature controllers of both, the cryostat and the sample holder. As the thermal inertia of the cryostat is large, it

takes up to 10 minutes until a new cryostat temperature is stabilized. However, very fast temperature changes of the sample away from the cryostat temperature could be realized by integrating a powerful heating foil on the sample holder. Thermal relaxation tests revealed that temperature steps of 10 K are well stabilized within about 30 s. The accuracy of typical resistance data was found to be $\pm 10 \mu\Omega$.

11.3.2 Electrical transport in doped manganites

A number of experiments have provided strong evidence for the existence of small polaronic charge carriers and their hopping conduction in the paramagnetic state of manganites. However, the nature of the charge carriers and the electrical transport mechanism in the low-temperature metallic state have not been resolved. At low temperatures, a dominant T^2 contribution in resistivity is generally observed, and has been ascribed to electron-electron scattering [26]. Jaime *et al.* [27] have recently shown that the resistivity is essentially temperature independent below 20 K and exhibits a strong T^2 dependence above 50 K. In addition, the coefficient of the T^2 term is about 60 times larger than that expected for electron-electron scattering. They thus ruled out the electron-electron scattering as the conduction mechanism and proposed single magnon scattering with a cutoff at long wavelengths. In their scenario [27], they considered a case where the manganese e_g minority (spin-up) band lies slightly above the Fermi level (in the majority spin-down band) with a small energy gap of about 1 meV. This is in contradiction with optical data [28] which show that the manganese e_g minority band is well above the Fermi level. This suggests that the conduction mechanism proposed in ref. [27] is not relevant.

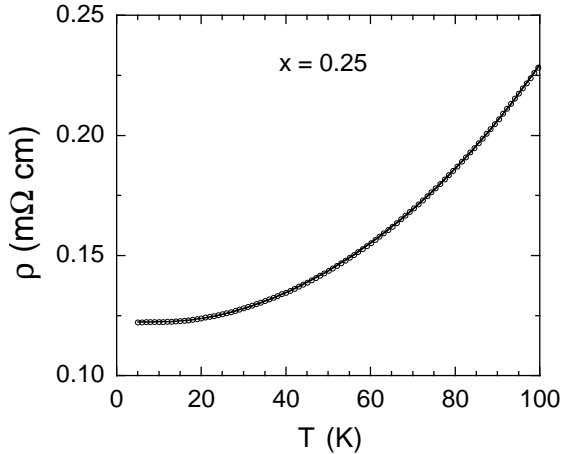


Figure 11.12: Low temperature resistivity $\rho(T)$ for a high-quality film of $\text{La}_{0.75}\text{Ca}_{0.25}\text{MnO}_3$. The solid line is a fit to the data using Eq. 11.1 with $\hbar\omega_s/k_B = 74.5(4)$ K.

Recently, Alexandrov and Bratkovsky [4] have proposed a theory for colossal magnetoresistance in doped manganites. Their model predicts that small polaronic transport is the prevalent conduction mechanism even below the ferromagnetic ordering temperature T_C . If their model is indeed relevant, the temperature dependence of the resistivity should agree with polaron metallic conduction. This is indeed the case as demonstrated by us [29]. There are three contributions to the resistivity: the residual resistivity ρ_o , the term $AT^{4.5}$ contributed from 2-magnon scattering [30], and the term $B\omega_s/\sinh^2(\hbar\omega_s/2k_B T)$, which arises from polaron coherent motion involving a relaxation due to a soft optical phonon mode that is strongly coupled to the carriers [29]. Here ω_s is the frequency of a soft optical mode. The low-temperature resistivity is then given by [29, 31]

$$\rho(T) = \rho_o + AT^{4.5} + B\omega_s/\sinh^2(\hbar\omega_s/2k_B T). \quad (11.1)$$

Fig. 11.12 shows $\rho(T)$ data for a high-quality epitaxial thin film of $\text{La}_{0.75}\text{Ca}_{0.25}\text{MnO}_3$. The data can be well fitted by Eq. 11.1 with $\hbar\omega_s/k_B = 74.5(4)$ K. If we allow the power in the second term of Eq. 11.1 to be a fitting parameter, the best fit gives a power of $4.2(4)$ [32], very close to 4.5 expected from 2-magnon scattering [30]. Furthermore, the coefficient A is in quantitative agreement with the prediction of 2-magnon scattering [32]. This provides the first bulk experimental evidence of half-metallic ferromagnetism in doped manganites [32].

11.3.3 Phase transition of the vortex lattice in cuprates

It is well known from thermal experiments that the vortex-lattice melting-transition in $\text{YBa}_2\text{Cu}_3\text{O}_{7-\delta}$ for magnetic fields parallel to the crystallographic c -axis is a first-order phase transition [25, 33, 34, 35]. The measured latent heats of melting, $L = T\Delta S$, are in very good agreement with theoretical predictions based on an anisotropic London model [36, 37]. When the applied magnetic field H is tilted away from c , one expects a certain scaling behavior of the melting fields $H_m(T)$ and of the associated discontinuities in entropy, ΔS .

However, it has been concluded from resistivity data in a perfect $H//ab$ geometry that deviations from the standard anisotropic scaling behavior [36, 37] should occur within 0.3 degrees around $H//ab$ [38]. Within this narrow range of angles, we may expect that the vortex physics is influenced by the layered crystal structure of the material, and a state with intrinsic vortex pinning should develop. Early theoretical work has predicted the occurrence of a second-order phase transition of the $H//ab$ Josephson-vortex lattice to a corresponding fluid state [39]. The thermodynamics of this state is experimentally unexplored. Our previous work on the angular dependence of ΔS [25, 33] did not reach sufficient resolution to explore a perfect $H//ab$ geometry. We have very much improved the accuracy, so we can test whether the thermodynamics of the vortex matter near $H//ab$ deviates from continuum-theory expectations or not.

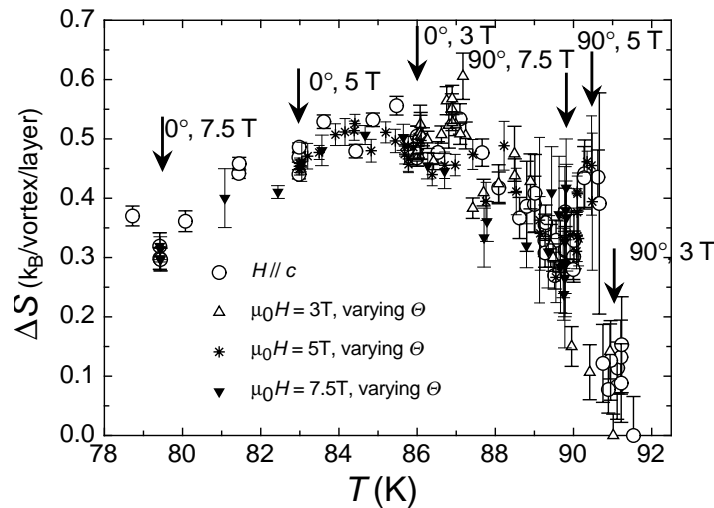


Figure 11.13: *Entropies of vortex-lattice melting in $\text{YBa}_2\text{Cu}_3\text{O}_{7-\delta}$ from 250 specific-heat experiments for varying external magnetic field H and angle Θ between H and the c -axis of the crystal. In agreement with continuum theory, all $\Delta S(T)$ data collapse onto one single curve.*

To do this, we have carefully investigated the angular dependence of the thermodynamic quantities $H_m(T)$ and ΔS of an untwined $\text{YBa}_2\text{Cu}_3\text{O}_{7-\delta}$ single crystal ($T_c = 92.5$ K) using our new high-resolution calorimeter with an angular resolution of 0.01 degrees. We have

performed a series of 250 heat-capacity measurements for a varying $H//c$, and for a fixed $\mu_0 H = 3$ T, 5 T and 7.5 T and varying angle between H and c , respectively (see Fig. 11.13). According to conventional continuum theory, the melting entropies ΔS for $H//ab$ should coincide with the respective data obtained at the same temperature in a $H//c$ geometry. For instance, ΔS for $H//ab$ in $\mu_0 H = 7.5$ T at $T = 89.8$ K should be the same as ΔS for $H//c$ in $\mu_0 H = 0.86$ T for $H//c$ at the same temperature. Within the accuracy of our apparatus, ΔS behaves as predicted by an anisotropic London theory, also for $H//ab$. There is still a measurable latent heat, at exactly the temperature calculated from an anisotropic continuum theory. We do not see any change in the thermodynamics of the vortex system for $H//ab$ in the investigated crystal.

Very recent theoretical [40] and experimental [41] work indicates, however, that significant deviations from continuum theory can occur only in cuprate superconductors with a electronic anisotropy larger than in optimally doped $\text{YBa}_2\text{Cu}_3\text{O}_{7-\delta}$. Suitable candidates for similar experiments are therefore oxygen depleted $\text{YBa}_2\text{Cu}_3\text{O}_{7-\delta}$ and $\text{Bi}_2\text{Sr}_2\text{CaCu}_2\text{O}_8$.

11.4 Spectroscopic studies of cuprates (not related to isotope effects)

11.4.1 NMR and NQR studies

In a collaboration with Dr. J. Karpinski (ETHZ) the influence of Sr for Ba substitution on the structure and charge distribution in $\text{YBa}_2\text{Cu}_4\text{O}_8$ was studied by NQR and compared to an extensive bond-valence sum (BVS) investigation [42]. The NQR frequency ν_Q of the plane copper is very sensitive to changes in the density of hole charge carriers n in the CuO_2 planes. NQR experiments for $\text{YBa}_2\text{Cu}_3\text{O}_{7-x}$ and $\text{La}_{2-x}\text{Sr}_x\text{CuO}_4$ show that ν_Q of the plane copper nuclei shifts towards higher values with increasing hole charge carrier concentration in the planes. In the $\text{YBa}_2\text{Cu}_3\text{O}_{7-x}$ family ν_Q changes at 100 K from 23.18 MHz in underdoped $\text{YBa}_2\text{Cu}_3\text{O}_6$ to 31.53 MHz in $\text{YBa}_2\text{Cu}_3\text{O}_7$. In the $\text{La}_{2-x}\text{Sr}_x\text{CuO}_4$ system, ν_Q increases linearly with Sr doping from 33 MHz for $x=0$ to 36.2 MHz for $x=0.15$. Assuming that each Sr ion delivers one hole charge carrier into the CuO_2 plane one gets a frequency change of $d\nu_Q/dn = 21$ MHz/hole. This result is used to estimate the increase of n in the CuO_2 planes of $\text{YBa}_{2-x}\text{Sr}_x\text{Cu}_4\text{O}_8$ when Ba is substituted by isovalent Sr. The measurements of ν_Q of plane copper in $\text{YBa}_{2-x}\text{Sr}_x\text{Cu}_4\text{O}_8$ show an increase by 330 kHz for $x = 0.3$ and by 610 kHz for $x = 0.6$ as compared to the pure $x = 0$ material. The increase in ν_Q is approximately linear in x , and thus one can conclude that the plane hole charge carrier concentration increases by 0.016 hole/Cu for $x = 0.3$ and 0.029 hole/Cu for $x = 0.6$. Since Sr and Ba are isovalent, this increase has to come from a charge redistribution in the structure. With x increasing, ν_Q of chain copper decreases for almost the same value as ν_Q of plane copper increases suggesting a chain to plane hole transfer. These results support BVS calculations which show a general increase of hole concentration and, in addition, a clear indication of redistribution of holes between copper and oxygen in the CuO_2 planes. The estimated values of the charge transfer differ slightly between BVS and NQR results. This is understandable in view of the crudeness of these two empirical approaches, which neglect other effects like volume change and strain caused by substitutions.

In a similar copper NQR study of $\text{YBa}_2\text{Cu}_4\text{O}_8$ the influence on structure and charge distribution by substituting Y with isovalent RE ions was investigated. A clear trend was observed showing an increase in NQR frequencies for plane as well as chain copper sites with increasing ionic radii of RE ions in the sequence Er, Ho, Y, Dy, Gd, Sm, Nd. These findings can be explained by a change in the chain to plane hole transfer, combined with an appreciable variation of lattice parameters, and have to be compared with the results obtained from a detailed BVS investigation.

11.4.2 μ SR studies of ruthenocuprates

There have been a number of recent reports of the coexistence of superconductivity and long-range magnetic order in the new class of hybrid ruthenocuprates $\text{RuSr}_2\text{LnCu}_2\text{O}_8$ (Ru-1212) and $\text{RuSr}_2(\text{Ln}_{1+x}\text{Ce}_{1-x})\text{Cu}_2\text{O}_{10}$ (Ru-1222) (Ln = Sm, Eu, and Gd) [43, 44]. These compounds have a layered structure with alternating CuO_2 and RuO_2 layers. It seems that superconductivity is developed in CuO_2 layers like in high- T_c cuprates and magnetism is due to the RuO_2 planes. Till now most of the reports have focused on a Ru-1212 phase, where the magnetic transition is observed at $T_m=133$ K and the onset temperature of superconductivity is $T_c=35$ K. Several experiments were performed to confirm the coexistence of superconductivity and magnetism on a microscopic scale. In particular, Bernhard *et al.* [44] using zero-field (ZF) muon-spin rotation (μ SR) technique found that the magnetic order is uniform and homogeneous on a microscopic level.

We decided to focus our attention on a Ru-1222 phase $\text{RuSr}_2(\text{Ln}_{1.4}\text{Ce}_{0.6})\text{Cu}_2\text{O}_{10}$ (Ln=Eu or Gd), which is actually the first ruthenocuprate where the coexistence of superconductivity and magnetism was found [43]. Recently the specific heat jump at T_c was observed in these samples confirming bulk superconductivity [45]. However, it remains to be demonstrated that the magnetism also has bulk character in order to infer the microscopic coexistence of magnetism and superconductivity. To answer this question we studied $\text{RuSr}_2(\text{Ln}_{1.4}\text{Ce}_{0.6})\text{Cu}_2\text{O}_{10}$ (Ln=Eu or Gd) using ZF- μ SR. Magnetization measurements showed that these samples were superconducting below $T_c=40$ K and the magnetic transition occurs at $T_m=80$ K.

The μ SR experiments were performed at the Paul Scherrer Institute (PSI), using essentially 100% spin-polarized positive “surface muons”. At low temperatures in all studied samples we observed damped oscillations due to muon-spin precession in local magnetic fields. A clear oscillation observed in the ZF- μ SR spectra implies that muons sense a well defined internal magnetic field.

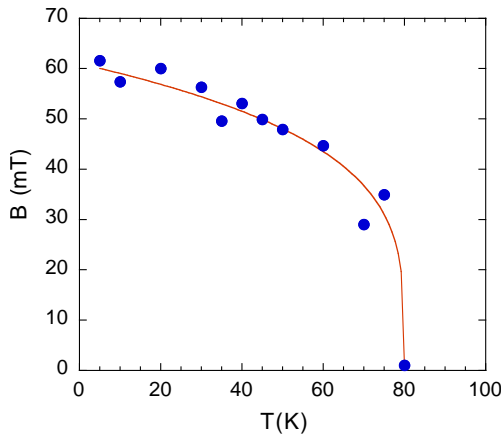


Figure 11.14: Temperature dependence of the internal magnetic field at the muon site in $\text{RuSr}_2(\text{Eu}_{1.4}\text{Ce}_{0.6})\text{Cu}_2\text{O}_{10}$. The solid line represents a fit with the power law $B(T) = B(0)(1 - T/T_m)^n$.

Figure 11.14 shows the temperature dependence of the internal magnetic field at the muon site for a $\text{RuSr}_2(\text{Eu}_{1.4}\text{Ce}_{0.6})\text{Cu}_2\text{O}_{10}$ sample. From the magnitude of the oscillatory component we deduce that the entire sample volume is magnetically ordered. Our ZF- μ SR experiments thus provide conclusive evidence of magnetic order in the superconducting Ru-1222 compounds. The magnetism is uniform and homogeneous in the entire sample volume. Therefore there is a microscopic coexistence of superconductivity and magnetism in Ru-1222 compounds.

11.4.3 EPR studies of cuprates

The investigation of high- T_c superconductors has, from a magnetic resonance point of view, till recently been dominated by NMR. The observation of EPR is of great interest, because the time-domain of observation of EPR is two to three orders of magnitude shorter than that of NMR. However, the application of EPR to high- T_c cuprates was restricted owing to the absence of intrinsic EPR signals in these compounds. The reason of the EPR silence in the cuprates is due to the extremely large linewidth. Another approach in the application of EPR to high- T_c superconductors is to dope these compounds with small amounts of paramagnetic ions which are used to probe the intrinsic behavior. One of the best candidates is Mn, which in the 2+ valent state gives a well defined signal and substitutes for the Cu^{2+} in the CuO_2 plane. Recently, Kochelaev *et al.* [46] have intensively studied the EPR of Mn^{2+} doped $\text{La}_{2-x}\text{Sr}_x\text{CuO}_4$. They found that the Mn ions are strongly coupled to the collective motion of the Cu spins (the so called bottleneck regime). The bottleneck regime allows to obtain substantial information on the dynamics of the copper electron spins in the CuO_2 plane [46].

We decided to take advantage of the Mn^{2+} doped $\text{La}_{2-x}\text{Sr}_x\text{CuO}_4$ to probe the copper spin relaxation via the bottleneck effect. Figure 11.15 shows the temperature dependence of the linewidth for samples with different Sr concentration. In all studied samples the linewidth

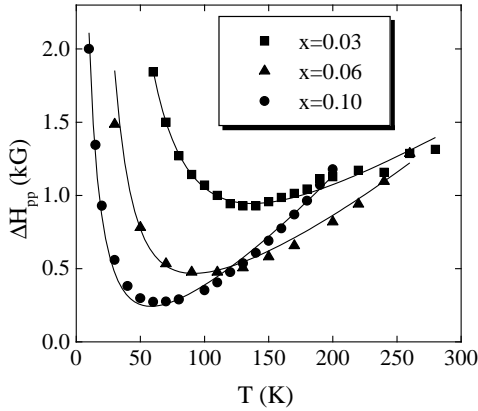


Figure 11.15: *Temperature dependence of the EPR linewidth ΔH_{pp} for $\text{La}_{2-x}\text{Sr}_x\text{Cu}_{0.98}\text{Mn}_{0.02}\text{O}_4$ samples with various concentration x . The solid lines represent the best fit using the theoretical model described in the text.*

decreases with decreasing temperature, passes through a minimum at a temperature T_{min} and increases again on further cooling. The low temperature upturn is more pronounced in underdoped samples and decreases with increasing doping and in addition T_{min} systematically shifts to lower temperatures.

In order to explain the observed temperature dependence of the linewidth, a new theoretical model is proposed that relates the EPR linewidth with the tilting and tunneling modes of the oxygen octahedra around the copper. This model leads to a Hamiltonian in which the Q_4^i and Q_5^i modes are coupled linearly to Dzyaloshinsky-type spin terms [47]:

$$H_{\sigma L} = \frac{J\Lambda}{8a} \sum_{\langle ij \rangle} \left[(\sigma_y^i \sigma_z^j - \sigma_z^i \sigma_y^j) (Q_4^i - Q_4^j) + (\sigma_x^i \sigma_z^j - \sigma_z^i \sigma_x^j) (Q_5^i - Q_5^j) \right], \quad (11.2)$$

$$\Lambda = \frac{3\lambda G}{\Delta^2}.$$

Here Q_4^i and Q_5^i are the normal coordinates of the oxygen octahedron CuO_6 , which describe its distortions due to the tunneling motion of the apical oxygen between the four potential minima without the rigid rotation of the octahedra as a whole. The constants λ and G correspond to the spin-orbit and orbit-lattice coupling, Δ is the crystal field splitting between the ground and excited orbital energy levels, $\langle ij \rangle$ means the sum over neighboring Cu sites in the $x - y$ plane, and a is the lattice constant.

Using this Hamiltonian we calculated the temperature dependence of the EPR linewidth and compared it with the experimental data [48]. The solid lines in Fig. 11.15 represent the best fit curves to the theoretical model. One can see that there is a good agreement between theory and experiment. Furthermore, this novel theoretical approach allows an estimation of the intrinsic EPR relaxation time, and provides an explanation for the long-standing problem of EPR silence in high- T_c superconductors. Our estimations show that the intrinsic EPR linewidth from copper spins in these compounds would be of the order of 10^4 G. This value is too large for observing an EPR signal at the usual frequencies.

11.5 Experiments with low-energy muons

As described in the Annual Report 1999/2000, the recent development of a low-energy (LE) muon beam at the Paul Scherrer Institute (PSI) [49, 50] offers completely new possibilities in μ SR research in condensed matter physics. These slow muons of tunable energy can be implanted at very small and controllable depth (with nanometer resolution) below the surface of a sample. The spectrum of applications of LE- μ SR is unique, including magnetic and superconducting thin films, multilayer systems and structured materials, quasi two-dimensional magnetic systems, and new materials which can only be prepared in thin film form.

Over the last five years the LE- μ SR technique was developed by researchers from PSI (E. Morenzoni, project leader) and from the Universities of Birmingham, Braunschweig, Konstanz, and Zurich. In the last year the LE- μ SR apparatus was considerably modified to improve its performance. In order to extend the range of possible samples to be investigated by this technique, a new ultra-high vacuum cryostat was built, that allows to perform experiments from 2.4 K up to room temperature. In addition, the magnetic field of the external solenoid was increased to 0.3 Tesla. With the goal to use solid neon as a moderation material in the future, which would increase the intensity of low energy muons by at least 50%, an experimental program was started to improve the cryostat required for the moderation of the low-energy muons. Furthermore, PSI has decided to build a new dedicated surface muon beam line. All these improvements will increase the muon intensity by a factor of 10, making LE- μ SR experiments much more efficient in the near future.

References

- [1] A.P. Ramirez, *J. Phys.:Condens. Matter*, **9**, 8171 (1997).
- [2] A.J. Millis, P.B. Littlewood, and B.I. Shraiman, *Phys. Rev. Lett.* **74**, 5144 (1995).
- [3] A. Moreo, S. Yunoki, and E. Dagotto, *Science* **283**, 2034 (1998).
- [4] A.S. Alexandrov, A.M. Bratkovsky, *Phys. Rev. Lett.* **82**, 141 (1999).
- [5] G.M. Zhao *et al.*, *Phys. Rev. B* **63**, R60402 (2001).
- [6] A.S. Alexandrov *et al.*, cond-mat/0011436 (submitted to *Phys. Rev. Lett.*).
- [7] G.M. Zhao *et al.*, *Phys. Rev. B* **62**, R11949 (2000).
- [8] F. Raffa, *et al.*, *Phys. Rev. Lett.* **81**, 5912 (1998).
- [9] G.V.M. Williams, *et al.*, *Phys. Rev. Lett.* **80**, 377 (1998).

- [10] B. Büchner *et al.*, Phys. Rev. Lett. **73**, 1841 (1994).
- [11] J.M. Tranquada, *et al.*, Nature **375**, 56 (1995).
- [12] H.A. Mook, *et al.*, Nature (London) **395**, 580 (1998).
- [13] V.J. Emery, S.A. Kivelson, and O. Zachar, Phys. Rev. B **56**, 6120 (1997).
- [14] A. Lanzara, *et al.*, J. Phys.:Condens. Matter **11**, L541 (1999).
- [15] A.W. Hunt, P.M. Singer, K.R. Thurber, and T. Imai, Phys. Rev. Lett. **82**, 4300 (1999).
- [16] R. Werner, M.Hücker and B. Büchner, Phys. Rev. B **62**, 3704 (2000).
- [17] N.J. Curro, *et al.*, Phys. Rev. Lett. **85**, 642 (2000) and M.-H. Julien, *et al.* (cond-mat/0010362).
- [18] A. S. Alexandrov and N.F. Mott, Int. J. Mod. Phys. **8**, 2075 (1994).
- [19] K.A. Müller, Physica C **341-348**, 11 (2000).
- [20] G.M. Zhao *et al.*, Nature **385**, 236 (1997).
- [21] G.M. Zhao *et al.*, J. Phys.: Condens. Matter **10**, 9055 (1998).
- [22] J. Hofer *et al.*, Phys. Rev. Lett. **84**, 4192 (2000).
- [23] P. Zimmerman *et al.*, Phys. Rev. B **52**, 541 (1995).
- [24] A. Schilling and O. Jeandupeux, Phys. Rev. B **52**, 9714 (1995).
- [25] A. Schilling *et al.*, Nature **382**, 791 (1996).
- [26] A. Urushibara *et al.*, Phys. Rev. B **51**, 14103 (1995).
- [27] M. Jaime *et al.*, Phys. Rev. B **58**, R5901 (1998).
- [28] A. Machida, Y. Moritomo, and A. Nakamura, Phys. Rev. B **58**, R4281 (1998).
- [29] G.M. Zhao *et al.*, Phys. Rev. Lett. **84**, 6086 (2000).
- [30] K. Kubo and N.A. Ohata, J. Phys. Soc. Jpn. **33**, 21 (1972).
- [31] G.M. Zhao, H. Keller, and W. Prellier, J. Phys.: Condens. Matter **12**, L361 (2000).
- [32] G.M. Zhao *et al.*, Phys. Rev. B (in press).
- [33] A. Schilling *et al.*, Phys. Rev. Lett. **76**, 4833 (1997).
- [34] M. Willemin *et al.*, Phys. Rev. Lett. **81**, 4236 (1998).
- [35] A. Schilling *et al.*, Phys. Rev. B. **61**, 3592 (2000).
- [36] G. Blatter *et al.*, Phys. Rev. Lett. **68**, 875 (1992).
- [37] M.W. Dodgson *et al.*, Phys. Rev. B. **57**, 14498 (1998).
- [38] W.K. Kwok *et al.*, Phys. Rev. Lett. **67**, 390 (1991).

-
- [39] X. Hu and M. Tachiki, Phys. Rev. Lett. **80**, 4044 (1998).
- [40] X. Hu and M. Tachiki, Phys. Rev. Lett. **85**, 2577 (2000).
- [41] S.N. Gordeev *et al.*, Phys. Rev. Lett. **85**, 2577 (2000).
- [42] J. Karpinski *et al.*, submitted to Phys. Rev. B.
- [43] I. Felner *et al.*, Phys. Rev. B **55**, R3374 (1997).
- [44] C. Bernhard *et al.*, Phys. Rev. B **59**, 14099 (1999).
- [45] X.H. Chen *et al.*, J. Phys.: Condens. Matter **12**, 10561 (2000).
- [46] B.I. Kochelaev *et al.*, Phys. Rev. B **49**, 13106 (1994).
- [47] B.I. Kochelaev, J. Supercond., **12**, 53 (1999).
- [48] A. Shengelaya *et al.*, to be published in Phys. Rev. B
- [49] E. Morenzoni *et al.*, J. Appl. Phys. **81**, 3340 (1997).
- [50] E. Morenzoni, *Physics and applications of low energy muons*, in Muon Science, S.L. Lee *et al.* Eds., IOP Publishing (1999).

12 Surface Physics

T. Greber, J. Kröger, M. Hengsberger, J. Wider, H. J. Neff, C. Cepek, W. Auwärter,
F. Baumberger, M. Hoesch, M. Muntwiler, I. Matsuda, R. Karrer, W. Deichmann,
J. Osterwalder

Artificial nanostructures, exemplified e.g. by ultra-thin films, quantum wires or quantum dots, are of enormous scientific and technological interest. Their electronic and magnetic properties are dominated by size- and shape dependent quantum effects and can thus be tailored to fulfill any particular need. Their diameter in at least one dimension does not exceed a few atomic layers, and therefore they consist to a large extent of interfaces and surfaces. In the surface physics laboratory we prepare clean surfaces, ultra-thin films and nanostructures under ultra-high vacuum (UHV) conditions and characterize their surface and interface structures at atomic resolution. Their electronic and magnetic properties are studied in detail. In order to measure the geometric arrangement of the atoms within the first few mono-layers of the surface we apply predominantly electron-based techniques such as x-ray photo-electron diffraction (XPD), medium-energy electron diffraction (MEED), low-energy electron diffraction (LEED), and more recently also scanning-tunneling and atomic force microscopy (STM/AFM). Angle-resolved UV photo-electron spectroscopy (ARUPS) gives us a detailed picture of the electronic band structure of such systems. Specifically, our experimental setup permits to directly map sections through the Fermi surface, which describes the electronic degrees of freedom relevant for transport properties, magnetic interactions and phase transitions. An important asset of such experiments is that the same probe (photo-emission) gives structural, electronic and magnetic information, and we can therefore study the interplay between these different degrees of freedom on the same sample.

Over the past year we have continued our work on the following systems:

- Vicinal Cu(111) surfaces expose (111)-oriented terraces separated by a roughly regular array of mono-atomic steps, therefore they represent lateral nanostructures that can be easily prepared. We have studied the behaviour of the two-dimensional electron gas formed by a surface state in this well-defined and tunable potential energy landscape. In particular, the effect of the terrace size distribution on the measured surface state dispersion was studied (see Section 12.1).
- The quality and the electronic character of the interfaces are very important in metal-insulator heterojunctions, especially for magnetic devices based on junctions in which the tunneling barrier depends on the electron spin. A system, which has been thoroughly studied by our group is the Ni(111) surface covered with one mono-layer of hexagonal boron nitride (*h*-BN, see Sections 12.3, 12.4 and 12.5).
- In a collaboration with Prof. M. Sancrotti (TASC Laboratory of the Istituto Nazionale per la Fisica della Materia, Trieste, Italy) the structural properties of C₆₀ mono-layer films on Ag(100) have been refined, and the coexistence of two inequivalent molecular orientations could be discovered by XPD [1].

Concurrent with these ongoing systematic studies, the development of several new experimental techniques has been pushed forward:

- Experimental near-node holograms could be measured in the new apparatus built in our laboratory (see Section 12.7). Nearest-neighbour atoms within a (111) plane of an Al crystal could be imaged at atomic resolution.

- Our picosecond time-resolved electron diffraction experiment is still in the phase where we struggle to enhance the surface sensitivity of the MEED technique. We have engaged in a strong collaboration with a group from Tohoku University (Japan). They have recently introduced a new three-dimensional MEED method that yields surface Patterson functions, thus revealing bonding vectors within the surface unit cells (see Section 12.8). In order to bypass these problems with surface sensitivity, a pulsed low-energy electron gun has been designed and tested which can be used for picosecond time-resolved LEED (see Section 12.9).
- We exploit our femtosecond Ti:sapphire laser system for introducing the same angle-mapping modes that we apply for ARUPS now also for two-photon photo-emission (2PPE) spectroscopy (see Section 12.4). These powerful measurement modes will give us unique capabilities for Fermi surface mapping at very low energies that can easily be extended to femtosecond time resolution.
- The construction and testing of our new experiment for spin-polarized Fermi surface mapping, which is designed to go eventually to the Surface and Interface Spectroscopy beamline of the Swiss Light Source, is progressing steadily. A sophisticated extraction electron optical system has been designed and is currently under construction (see Section 12.6). This experiment will permit the spin-resolved measurement of Fermi surfaces in magnetic nanostructures.
- We continued our collaboration with the surface chemistry group of Prof. J. R. Huber of the Physical Chemistry Department (P. Willmott, H. Spillmann) who have developed unique thin film preparation capabilities using pulsed reactive crossed-beam laser ablation. They have grown single crystalline films of zirconium carbonitrides ($\text{ZrC}_x\text{N}_{1-x}$) with the aim of correlating the hardness of these materials with their electronic structure as a function of the composition parameter x .

12.1 Fermi surfaces of the two-dimensional surface states on vicinal Cu(111)

The clean Cu(111) surface supports a free electron like Shockley-type surface state, with a maximum binding energy of $\sim 0.4\text{eV}$ at $\bar{\Gamma}$. This state arises as a consequence of the broken translational symmetry in the normal direction at the crystal surface. Its wave functions propagate parallel to the surface with a Fermi wave length of $\lambda_F \sim 3\text{nm}$ and fall off exponentially both towards the vacuum and towards the bulk and are thus quasi two-dimensional (2D).

We have continued our studies of the Shockley surface state on Cu(332) and Cu(221). Both surfaces are composed of (111) terraces bounded by mono-atomic steps running along $[\bar{1}\bar{1}0]$. An analysis of the LEED spot profiles reveals a rather broad terrace width distribution, in agreement with an STM study [2]. The photo-emission Fermi surface map of Cu(332) in Fig. 12.1a shows a slightly elliptical, i.e. anisotropic surface state contour with a strongly angle dependent line-shape in the momentum distribution curves (Fig. 12.1b-c). The anisotropy of both, the dispersion and the line-width is less pronounced in the case of Cu(221).

We have developed a model for the surface state line-shape that includes the effects of the terrace width distribution [3]. Extensive 2D fits showed, that the anisotropic line-width can be fully attributed to the spatial averaging of the photo-emission experiment. However, an isotropic reduction of the photo-hole lifetime with decreasing terrace length and a remaining anisotropy in the dispersion on Cu(332) are intrinsic properties of the 2D electron gas in the 1D step lattice. The latter is strong evidence for the super-lattice sensitivity of the

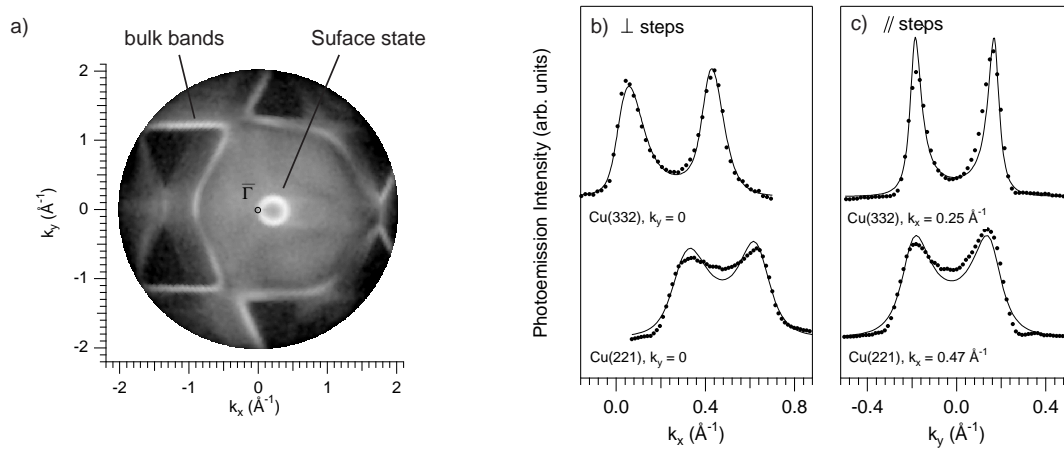


Figure 12.1: a) Fermi surface map from Cu(332). b)–c) Momentum distribution curves at the Fermi level from Cu(332) and Cu(221). The data are all shown to scale. The thin lines are results from two-dimensional fits, including the effect of finite surface order.

surface state. The reduced photo-hole lifetime on the other hand supports the scenario of a continuous surface state to surface resonance transition with increasing miscut away from the [111] direction, as it is expected from symmetry considerations.

12.2 Surface states and the stability of adsorbate periodicities: O/Mo(110)

In solid state physics, there is a lot of interest to understand materials properties and behaviour in relation to the shape and size of their Fermi surface. Quite interesting model systems can be found on metallic surfaces where complete Fermi surfaces can be mapped by photo-emission. A few years ago there was a study of an oxygen adsorbate phase on

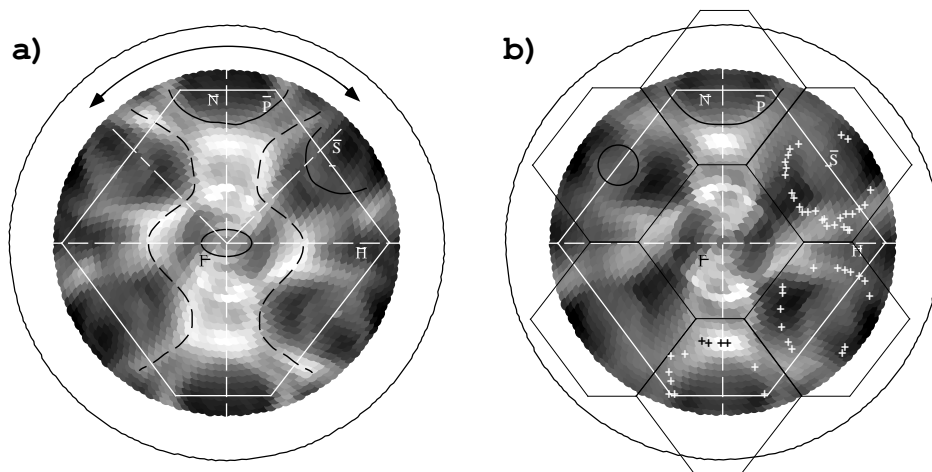


Figure 12.2: a) He I excited Fermi surface map for clean Mo(110). The (1×1) surface Brillouin zone is indicated by white lines. The hole pockets and the electron pocket are marked as full and dashed black curves, respectively. b) Fermi surface map for $p(2 \times 2)$ O/Mo(110). Here, the boundaries of the (2×2) surface Brillouin zones are added as black lines. Some of the earlier photo-emission data [4] are included as small crosses.

Mo(110), speculating that the high propensity of this system to form the (2x2) periodicity even at very low coverages is due to a *global Fermi surface nesting* [4]. This idea was supported by photo-emission data that indicated the presence of hole pockets centered at the \bar{N} and \bar{S} high symmetry points in the surface Brillouin zone that, though unrelated by the symmetry of the clean surface, create a perfect nesting scenario for a (2x2) superstructure due to their identical size and shape (see crosses in Fig. 12.2b).

This interpretation was recently challenged by new high-resolution electron energy loss measurements [5] that showed no indication for any softening of surface phonon modes around the \bar{N} point or the \bar{S} point for the p(2x2) phase that would be expected in this global nesting scenario. We have therefore redone the photo-emission experiment on this system, using our superior intensity mapping technique for tracking the Fermi surface contours [6]. In Fig. 12.2a, the measured contours from the clean Mo(110) surface are shown for reference. The Fermi surface map for the p(2x2) oxygen adsorbate phase in Fig. 12.2b gives no indication for the previously measured hole pockets (small white crosses) that have rendered this Fermi surface prone to nesting. In fact, there appear to be much more subtle changes to the surface states upon oxygen adsorption than for the case of hydrogen adsorption [7], where surface phonon softening was observed for two wave vectors that could clearly be related to nesting across Fermi surface sheets. The smaller influence of adsorbed oxygen on the surface states could be rationalized with the longer bond distance of the adsorbate to the Mo(110) top layer.

12.3 Tunneling across hexagonal boron nitride films on Ni(111)

in collaboration with G. Grad and P. Blaha, Institut für Physikalische und Theoretische Chemie, TU Wien

Hexagonal boron nitride (*h*-BN) is a wide band-gap insulator ($E_{gap} \approx 5$ eV) that can be grown as single layers on Ni(111) [8, 9]. It serves as an ultimately thin model system for the investigation of spin polarized tunneling junctions. In Fig. 12.3a the known atomic structure

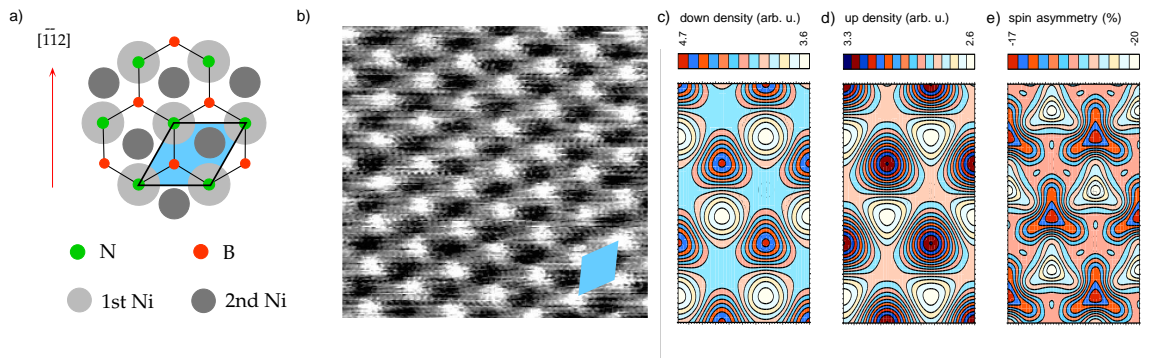


Figure 12.3: *h*-BN on Ni(111): a) Top view of the honeycomb structure of *h*-BN on Ni(111). The (1x1) unit cell is indicated. b) Atomically resolved STM current image ($V_{tip} = 4.8$ meV, $0.2 < I_t < 0.5$ nA). The (1x1) unit cell is indicated. c) Calculated spin up density of states at E_F , 2.17 Å above the N layer. d) calculated spin down density of states at E_F , 2.17 Å above the N layer. e) Spin asymmetry of c) and d).

is shown [9, 11, 10]. A single layer *h*-BN on Ni(111) is not thick enough to be insulating for electron transfer. This is seen from the fact that these surfaces can be imaged by scanning tunneling microscopy (STM) (see Fig. 12.3b) [9]. STM experiments showed atomically resolved images of *h*-BN/Ni(111). In the (1x1) unit cell ($a = 2.49\text{\AA}$) three distinct tunneling conductance levels were found. This translates into a charge density variation [12] that can be assigned to the images of three distinct sites: the nitrogen or top layer nickel site, the boron or *fcc* site, and the second layer nickel or *hcp* site. From our STM work it was not possible to identify the atomic species within the unit cell.

Density functional slab calculations for the *h*-BN/Ni(111) system solve this puzzle and give insight into the magnetism of this interface. In Fig. 12.3c the spin up (majority spin) density of states ρ_{\uparrow} at $E_F \pm 60\text{ meV}$, 2.17\AA above the top N-layer is shown. The calculations identify the bright spots of highest conductance as the nitrogen sites and the grey spots to boron sites. The density functional calculations were spin polarized and therefore a spin asymmetry $A = (\rho_{\uparrow} - \rho_{\downarrow})/(\rho_{\uparrow} + \rho_{\downarrow})$ can be plotted (see Fig. 12.3e). The average asymmetry is -18.5 %, i.e. minority electrons prevail, and the variation at a distance of 2.17\AA above the top layer is 3 %.

12.4 Interface states in a metal-insulator heterojunction

In the *h*-BN monolayer on Ni(111) system, still little is known about the electronic states close to the Fermi level, especially in the unoccupied region. Two-photon-photoemission (2PPE) allows one to access both, occupied and unoccupied states, along with providing femtosecond temporal resolution from of a pulsed laser beam. Despite the advantages of the laser light source, the analysis of 2PPE spectra is less straightforward since three states are generally involved in one transition appearing as peak in the 2PPE spectrum.

In Fig. 12.4a, the normal emission 2PPE spectrum of *h*-BN/Ni(111) is shown in comparison to that of the bare Ni(111) surface. The spectrum from the *h*-BN covered sample extends over a larger energy range than that of clean Ni(111) due to the reduced work function. We want to focus our attention here onto the most prominent feature near the Fermi energy. The “counterpart” in the Ni spectrum appears at slightly higher binding energy, shifted by about 200 meV and with much less intensity. The peak in the Ni spectrum arises from a $\bar{\Gamma}$ -surface state, which is spin split with occupation of only the majority spin states [13]. The huge intensity, however, of the peak in the *h*-BN spectrum gives evidence for the presence of an intermediate state in the 2PPE process since a slight tuning of the photon energy $h\nu$ causes a peak shift with $1 \times h\nu$ (see Fig. 12.4b). Preliminary analysis of the theoretical results shows this state to be an image potential state. This kind of state results from confinement of electrons between the crystal surface (band gap) and, on the vacuum side, the Coulomb potential of their own image charge in the crystal [14]. The energy of the hydrogen-like Rydberg series is tied, thereby, to the vacuum level as cut-off of the image potential and on the screening properties of the electrons in the crystal surface. From the 2PPE spectra one deduces a binding energy of roughly 600 meV as referred to the vacuum level. Full metallic screening as found e.g. on noble metal surfaces yields a maximum binding energy of $1/16\text{ Ry} = 850\text{ meV}$ for image potential states. The effective mass of this state, as estimated from dispersion plots along high-symmetry directions (Fig. 12.4c), is of the order of 0.5 times the free electron rest mass, thus smaller by a factor of 2 than the expected value for a free-electron-like image potential state. Further studies are necessary to determine the precise character of this state.

In order to verify the hypothesis of a strong intermediate state, 2PPE intensity maps have been recorded at fixed electron energy for various emission angles. One of these maps, taken at the 2P-Fermi energy, is displayed in Fig. 12.4d. The bright yellow ring should correspond

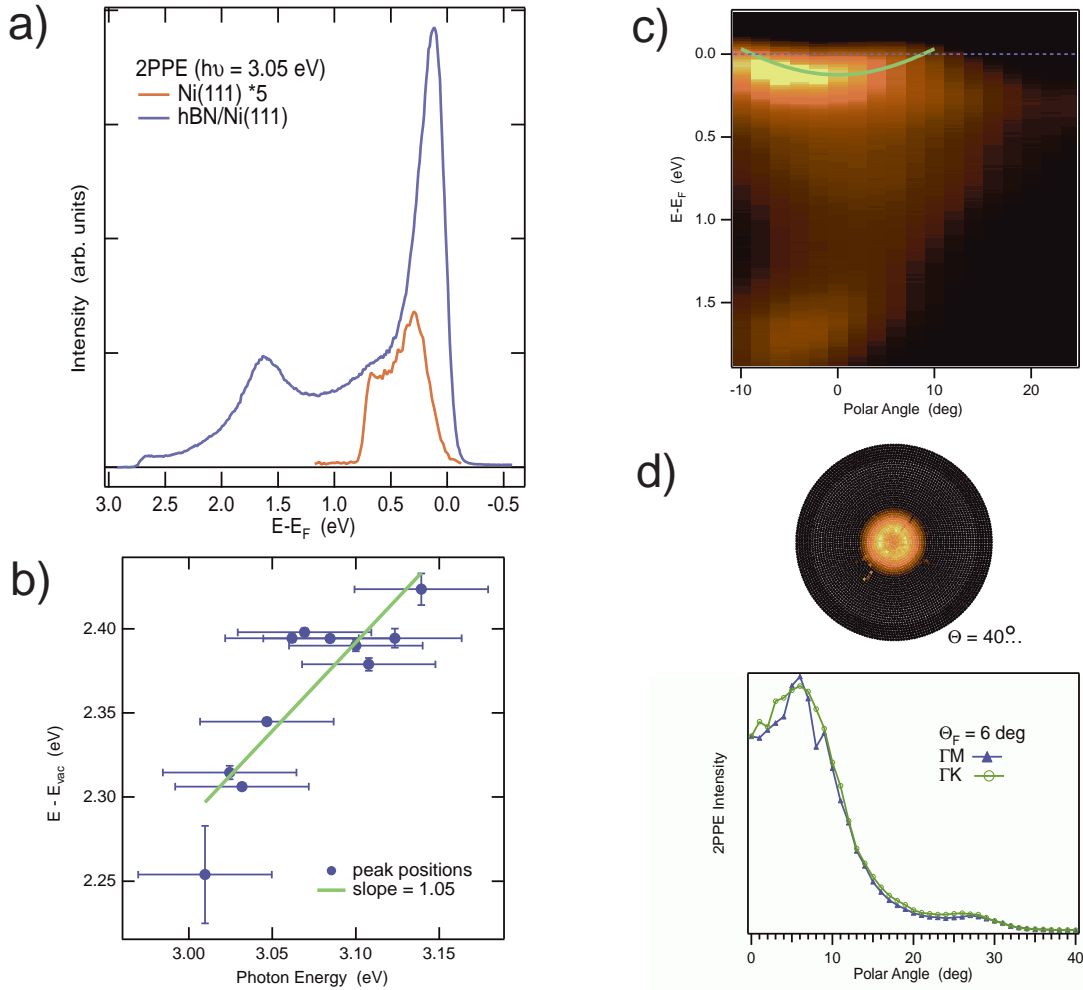


Figure 12.4: *Two-photon photoemission (2PPE) results from h-BN/Ni(111). a) Normal emission spectra ($h\nu = 3.1 \text{ eV}$) from h-BN/Ni compared to that from Ni(111); b) shift of the prominent peak position with photon energy; c) angle-resolved spectra as colour plot (yellow = high intensity), taken along $\Gamma\bar{M}$ of the substrate together with the measured dispersion of the interface state (green line); d) two-dimensional map of the 2PPE intensity at the Fermi energy (upper panel) and two intensity profiles along high symmetry directions (lower panel).*

to a momentum of 0.127 \AA^{-1} . In future experiments, this observed state can be used as a very sensitive probe of the dielectric properties of this interesting metal-insulator junction.

12.5 Co intercalation underneath hexagonal boron nitride films on Ni(111)

In order to study spin dependent tunneling, atomically well defined metal-insulator-metal structures have to be prepared. To produce a model system of a tunneling junction cobalt is evaporated on a mono-layer-thick hexagonal boron nitride (h-BN) film on a Ni(111) substrate [8, 9, 11]. STM measurements show that Co forms three-dimensional (3D) clusters at room temperature, while it prefers to grow in a more two-dimensional (2D) way at elevated temperature ($150 \text{ }^\circ\text{C}$). These two island types can coexist, as is seen in Fig. 12.5a. STM images give strong indications that intercalation of Co underneath the h-BN mono-layer is

responsible for the formation of different island types: defect lines, corrugated much less than the h -BN film thickness, are often found attached to the 2D islands (see Fig. 12.5a-b). These defects align to crystallographic directions and are related to the h -BN film: they can be seen on bare films but not on the clean Ni(111) substrate. From STM images showing sharp defect lines crossing 2D islands (as seen in Fig. 12.5b) it is concluded that these islands grow underneath the h -BN layer. This is consistent with missing forward scattering features in photo-electron diffraction patterns from the h -BN mono-layer with elevated-temperature deposits of Co.

Using the STM tip as a manipulator by working at small tunneling resistance, it is possible to remove the 3D Co clusters selectively one by one (see Fig. 12.5c). The 2D islands are not affected by this procedure and they are thus more strongly bound to the surface than the 3D clusters, again supporting the intercalation picture.

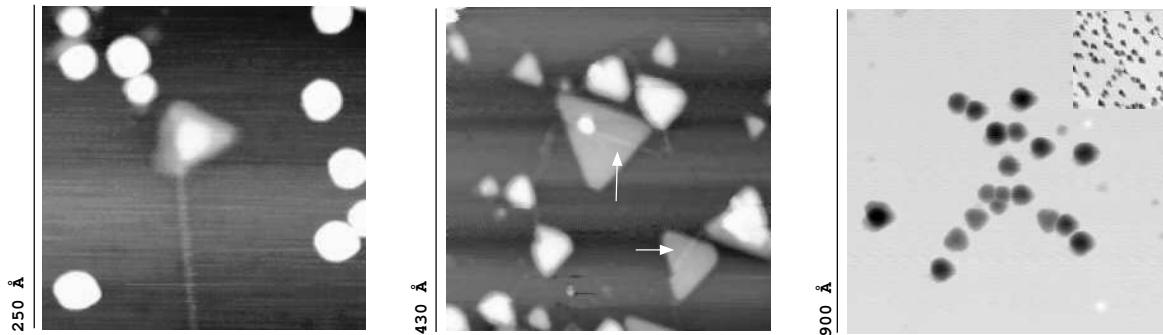


Figure 12.5: *STM images of Co on h -BN/Ni(111): Panel a) shows a two-dimensional triangular shaped island attached to a line defect coexisting with three dimensional Co clusters. In b) such defects are crossing two islands (marked by arrows). Panel c) (inverted gray scale) demonstrates the removal of three dimensional Co clusters by the STM tip (the inset represents the starting configuration)*

12.6 Status of COPHEE, the COmplete PHotoEmission Experiment

A new photo-electron spectrometer is being set-up featuring a full three-dimensional spin polarimeter, which makes it complete in the sense that all properties of the photoelectrons in the frame of reference of the sample crystal lattice can be measured. This apparatus is devoted to spin-resolved Fermi surface mapping using angle-resolved ultraviolet photo-electron spectroscopy. In this type of experiment, the sample and therefore also its magnetization direction are rotated over the full 2π solid angle above the crystal surface, thus requiring spin analysis in all three dimensions. After successful test operation using a He-lamp it is to be used as an end-station at the Surface and Interface Spectroscopy (SIS) beam-line of the new Swiss synchrotron radiation source (SLS) under construction at Paul Scherrer Institut, Villigen, or alternatively, at the Advanced Photo-emission Experiment (APE) beam-line at ELETTRA in Trieste.

UV-photoelectrons are energy and angle selected by a hemispherical analyzer (EA125 from Omicron Vakuumphysik GmbH) and then transported into a spin-polarimeter based on 60 keV Mott scattering (Mott detectors built by St. Petersburg Technical University [15]). The year 2000 was devoted to the design of the beam transport system, which leads the electrons from the EA125 exit slit to the two Mott detectors. In an electrostatic beam deflection system the spin-orientation in the laboratory frame remains constant and therefore two orthogonal polarimeters can determine the full three-dimensional spin-polarization

vector, since each Mott detector can intrinsically analyze the two components transverse to the respective incoming beam.

12.6.1 Electron optics

The electrons which travel at low pass energy (1... 10 eV) inside the analyzer are accelerated to 300 times the pass energy in a two-step extraction lens behind the analyzer exit slit (lens made by Omicron). They are deflected by 90° to gain space for the bulky polarimeter. A gate lens provides vacuum safety for the gold foils inside the polarimeter and acts as an Einzel lens for the electron beam. The beam is deflected 20° to the left or right by a parallel plate deflector, which is switched at 20... 0.1 Hz to allow quasi-simultaneous operation of the two detectors. A spherical end-deflector separates the two beams by $\pm 45^\circ$ for the required orthogonality. Inside the Mott detectors the electrons are accelerated to 60 keV by a spherical focusing field and detected by silicon diode detectors after back-scattering off an 80 nm gold foil. The lens elements and results of ray-tracing calculations are shown in Fig. 12.6.

The mechanical parts including the very demanding vacuum envelope are in production in the mechanical workshop. High voltage supplies such as the fast 2 kV polarity switch for quasi-simultaneous data acquisition have been manufactured by ISEG Spezialelektronik GmbH.

12.6.2 Data acquisition hard- and software

Besides controlling the various spectrometer devices (manipulator, energy analyzer, polarimeter optics, and detectors) photo-emission experiments at a synchrotron facility need to communicate with beam-line devices (storage ring, undulator, and monochromator). For this reason the SLS computing and control concepts are adopted in COPHEE. A VME system is the node for all electronic control and measurement signals of the spectrometer. It is operated by the Experimental Physics and Industrial Control System (EPICS) which provides a

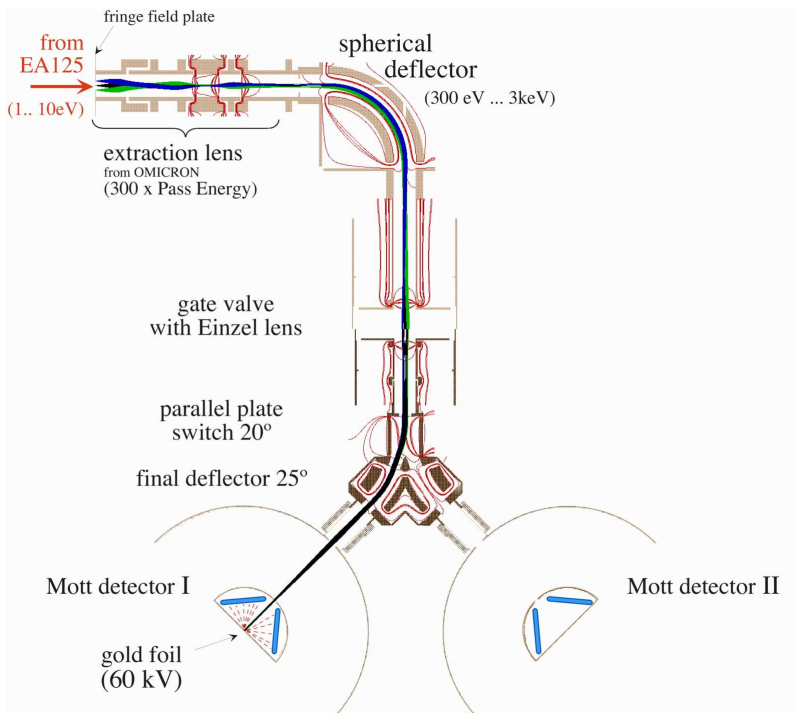


Figure 12.6: Visualization of the ray-tracing calculations made to design the COPHEE electron optics (calculations and graphics by SIMION [16], 3D polarimeter assembly rotated 90° for graphical clarity)

standardized and network-transparent interface to many different device types. Furthermore, fairly complex real-time tasks such as energy scans with synchronized detector readout are easily implemented on this level.

The high-level measurement control and the online data presentation for the sophisticated angle-scanned photo-emission experiments will be implemented in Delphi language on a remote personal computer. It is connected to the spectrometer simply via an Ethernet network using readily available interface software.

12.7 Near node photo-electron holography

Determining atomic structures at surfaces and interfaces is still a difficult but very important task. The more complex a system is, the more important it is to have direct methods that can provide a rough image of basic structural units. An angle scanned photo-electron diffraction experiment has all prerequisites for holography. The measured core-level photo-emission intensity is a coherent superposition of the directly emitted wave and the singly and multiply scattered waves. In the experimental realization of this idea several problems are encountered, caused by the strong and anisotropic nature of the electron-atom scattering amplitude and by multiple scattering effects. Near node photo-electron holography (NNPEH) [17] is a new approach to photo-electron holography that exploits the anisotropic nature of the electron source wave in order to minimize forward and multiple scattering effects. The idea has been successfully tested with an Al(111) single crystal in experiments at the synchrotron facility ELETTRA in Trieste, Italy [18]. Concurrently, a NNPEH experiment has been set up in our home lab. For unpolarized x-rays such as produced by a laboratory source, the near-node condition is met by having the electron escape direction very near the x-ray incidence direction, separated by only 10° to 20° . First results, again with an Al(111) single crystal, are presented in Fig. 12.7. In the holographic reconstruction (Fig. 12.7b) the six nearest neighbors of an Al atom within the (111) crystal plane are clearly resolved.

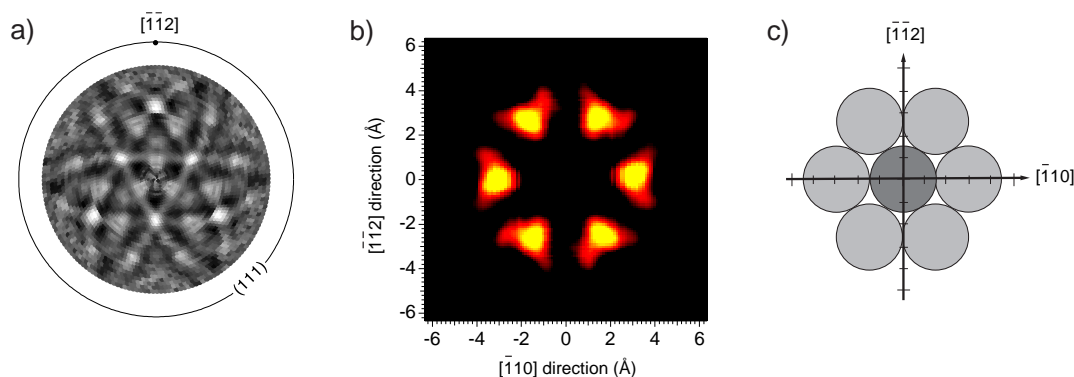


Figure 12.7: a) Stereographically projected experimental Al 2s ($E_{kin} = 1370\text{ eV}$) photo-electron diffraction pattern from an Al (111) single crystal. b) Corresponding holographic real space reconstruction of a plane parallel to the surface containing the emitter at the origin $(0, 0)$. The six nearest neighbors are clearly resolved at a distance of 3.2 \AA . Note that the photo-emitter is not imaged in photo-electron holography. c) Hard sphere model of a (111) plane of an aluminum crystal.

12.8 Surface Patterson functions from medium-energy electron diffraction

in collaboration with T. Abukawa, S. Kono, Tohoku University, Sendai, Japan

We have continued our project to develop a picosecond time-resolved electron diffraction experiment for studying surface dynamics. In the process we were facing the problem that the standard medium-energy electron diffraction (MEED) experiment did not yield the required mono-layer structural sensitivity. Recently, a Japanese group introduced an new structural tool based on multiple-energy, full three-dimensional diffraction images that can be Fourier transformed to yield Patterson functions very similar to those obtained from x-ray diffraction [19]. In a close collaboration with this group we have adopted this method, using our pulsed MEED electron gun. In a first test experiment we have successfully measured nearest neighbor bond vectors within a Ge(111) surface. In Fig. 12.8a a section through a three-dimensional data set of scattering intensities is shown. The experimental geometry, i.e. the incoming electron beam direction and the position of the two-dimensional detector determines which atoms can be imaged. The data set of Fig. 12.8a is sensitive to the geometry normal to the crystal surface. The planar section through the Patterson function in Fig. 12.8c displays clearly the nearest neighbour bond direction and bond length along the (111) direction. The extension of such experiments to picosecond time resolution is straightforward using a pump-probe approach.

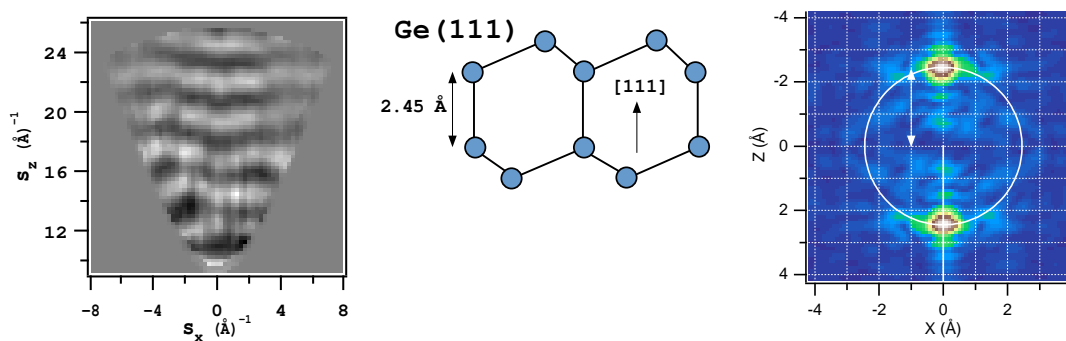


Figure 12.8: a) Normalized scattering intensities of electrons backscattered from a Ge(111) surface, plotted as a function of the scattering vector $\vec{s} = \vec{k}_f - \vec{k}_i$ where \vec{k}_f and \vec{k}_i are scattered and incoming electron wave vectors, respectively. b) Planar view of the Ge crystal structure, indicating the 2.45 \AA between nearest neighbor atoms along the (111) direction. Patterson function obtained from Fourier transforming a full three-dimensional set of scattering intensities. The white arrow indicates the bond distance along the (111) direction.

12.9 Construction of an electron gun for time resolved low-energy electron diffraction

A second option for enhancing the surface sensitivity of electron diffraction is to go to lower energies. The standard tool for structure determination in surface physics is low energy electron diffraction (LEED), where energies of typically 50 eV - 150 eV are used. However, it is a very demanding task to prepare picosecond pulses of electrons at such low energies. An miniaturized electron gun which produces ultra short and coherent (parallel and monochromatic) electron pulses with an expected time resolution of less than 5 ps has been developed in our lab.

Through the back side of the electron gun, femtosecond laser pulses (80 fs, 400 nm wavelength) are directed through a sapphire window onto a photo-cathode, which consists of an atomically flat and thin (~ 200 Å) gold film grown on a mica substrate. The laser beam is transmitted from behind through the mica plate and photoelectrons are emitted from the gold-vacuum interface by two-photon photo-emission. These electrons are accelerated to a kinetic energy of 100 eV over a distance of less than 100 μm from where they move in field free space towards the sample. The calculated temporal jitter within the electron pulses is less than 3 ps for a sample placed at a distance of 4 mm from the photo-cathode. The main contribution is due to the energy spread of the electrons, which has been optimized by choosing gold as cathode material. The vacuum part of the gun is shown in Fig. 12.9. The actual electron gun is in the tip of the metal cone, while the whole setup is much bigger for functionality.

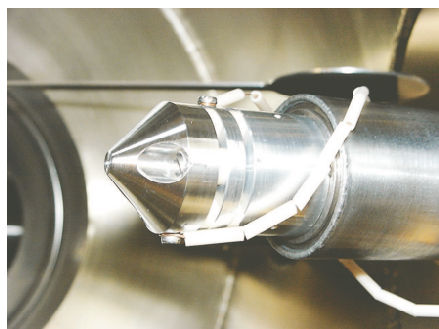


Figure 12.9: *The vacuum end of the picosecond low-energy electron gun.*

The gun has been designed, built and tested [20]. For this purpose, the electron beam has been directed onto a two-dimensional position-sensitive channel-plate detector, placed 65 mm away from the gun. From the spot size of the beam on the detector (Fig. 12.10) the divergence is calculated to be about 1.5° . In these tests, the following specifications could be

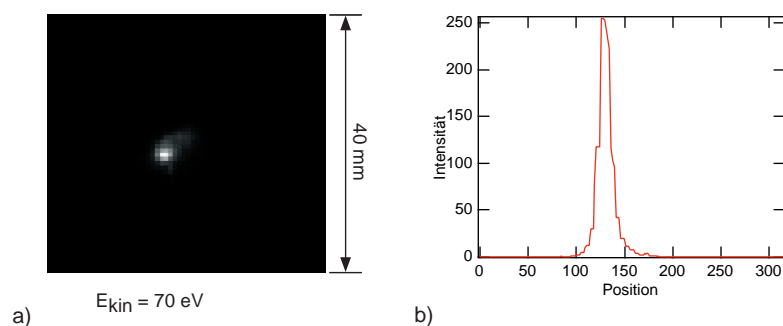


Figure 12.10: *a) The electron beam profile for an energy of 70 eV, measured with a two-dimensional detector placed at a distance of 65 mm from the electron gun. b) Beam cross section, from which the beam divergence of 1.5° was determined.*

demonstrated [20]: A very low electron current of about 2 fA was measured on the detector. The measured energy resolution is about 1.3 eV, a part of which is likely to be due to the resolution of the detector. With this energy spread, the time resolution should be less than 4 ps. The gun therefore meets the design criteria and, if the electron current can be increased by one or two orders of magnitude, the picosecond LEED experiment is within reach.

References

- [1] C. Cepek, R. Fasel, M. Sancrotti, T. Greber, J. Osterwalder, Phys. Rev. B 63, 125406 (2001).
- [2] A.R. Bachmann, A. Mugarza, J.E. Ortega, A. Nürmann, S. Speller, Phys. Rev. B, submitted
- [3] F. Baumberger, T. Greber, and J. Osterwalder, Phys. Rev. B, submitted
- [4] S. Dhar, K.E. Smith, S.D. Kevan, Phys. Rev. Lett. 73, 1448 (1994).
- [5] J. Kröger, S. Lehwald, H. Ibach, Phys. Rev. B 58, 1578 (1998).
- [6] J. Kröger, T. Greber, J. Osterwalder, Surf. Sci. 459, 173 (2000).
- [7] J. Kröger, T. Greber, J. Osterwalder, Phys. Rev. B 61, 14146 (2000).
- [8] A. Nagashima, N. Tejima, Y. Gamou, T. Kawai, and C. Oshima, Phys. Rev. B 51, 4606 (1995).
- [9] W. Auwärter, T.J. Kreutz, T. Greber, J. Osterwalder, Surf. Sci. 429, 229 (1999).
- [10] Y. Gamou, M. Terai, A. Nagashima, and C. Oshima, Sci. Rep. RITU, A 44, 211 (1997).
- [11] M. Muntwiler, W. Auwärter, F. Baumberger, M. Hoesch, T. Greber and J. Osterwalder, Surf. Sci. 472, 125 (2000).
- [12] J. Tersoff, D.R. Hamann, Phys. Rev. B 31, 805 (1985).
- [13] M. Donath, Surf. Sci. Rep. 20, 251 (1994).
- [14] T. Fauster, in *Electronic Surface and Interface States on Metallic Systems*, edited by E. Bertel and M. Donath (World Scientific, Singapore 1995), p. 171.
- [15] V.N. Petrov, M. Landolt, M.S. Galaktionov, B.V. Yushenkov, Rev. Sci. Instr. 68, 4385 (1997).
- [16] "SIMION 3D Version 6.0" by David A. Dahl 43ed ASMS Conference on Mass Spectrometry and Allied Topics, May 21-26 1995, Atlanta, Georgia, pg 717, <http://www.srv.net/klack/simion.html>
- [17] T. Greber, J. Osterwalder, Chem. Phys. Lett. 256, 653 (1996).
- [18] J. Wider, F. Baumberger, M. Sambì, R. Gotter, A. Verdini, F. Bruno, D. Cvetko, A. Morgante, T. Greber, J. Osterwalder, Phys. Rev. Lett. 86, 2337 (2001).
- [19] T. Abukawa, C.M. Wei, T. Hanano, S. Kono, Phys. Rev. Lett. 82, 335 (1999).
- [20] R. Karrer, *Bau einer Elektronenkanone für zeitaufgelöste Beugung mit langsamen Elektronen (LEED)*, Diplomarbeit Uni Zürich, 2000.

13 Physics of Biological Systems

Hans-Werner Fink, Cornel Andreoli, Conrad Escher (since February 2001)

13.1 Overview

Our overall motivation in studying the physics of biological systems can roughly be illustrated as follows:

- Biological systems are objects of condensed matter physics that exhibit unique properties. In comparison to inorganic materials, biological objects can exercise a number of dedicated functions. Both, their shapes and the associated functions, are governed by the same class of interactions that are known for a long time from gas-, liquid- or solid-state physics. However, what makes them unique despite all the similarities to classical physics objects, is their complexity. It manifests itself for example in the lack of symmetry if compared to crystals. On the other hand, the variety of shape and structural transitions within those systems are not just governed by random dynamics alone like in a fluid. Coming to grips with those fragile systems that react very sensitive to changes in their environment and that are capable of carrying out all sorts of surprising actions is a real challenge for physical sciences.
- In realizing the complexity of biological molecules, it might be a sensitive approach to start out by isolating individual systems. Our technique of low energy electron holography appears well suited to "look" at just a single species and we plan to push the resolution of this tool to arrive at detailed structural and electronic information on individual molecules.
- Our discovery that DNA molecules are electrical conductors, have led us to look at this molecule in an idealized way by treating it as a simple physical object and by disregarding its biological function completely. The only aspect that matters for this purpose is the fact that the DNA is long and thin. Furthermore, the chemistry of the DNA is well understood and the molecule is almost defect free in comparison to man-made structures on the nanometer-scale. To this end the DNA is a quantum wire and we plan to use this property to develop molecular electronic devices.

13.2 Interfacing bio-molecules to silicon structures

Recent experiments on DNA conductivity were done with molecules that had been deposited over an array of holes in a thin film. We thus had to rely on statistics to find a desirable configuration of molecules stretched over a certain hole. In order to fabricate devices, this seems an unsuitable approach and we thus have to develop ways to place the molecules at pre-defined sites on a silicon structure. There are several strategies to achieve this goal. One can use molecular recognition on a patterned device structure to have the molecules find their places in the liquid phase automatically. It is also feasible to use mechanical manipulation on a nanometer-scale to place them at the desired positions.

Another possibility is that, due to the electric charge of the DNA, it should be possible to use local electric fields on a device structure to stretch and trap the molecules and to thus bridge a specific site on a chip. Figure 13.1 illustrates how the arrangement of small areas on a chip with adjustable field strength can be achieved. We start out with a structure that has been fabricated for us by Clondia Chip technologies in Jena using optical lithography. Next, the fine structuring is done in our laboratory. To create two free standing wires over

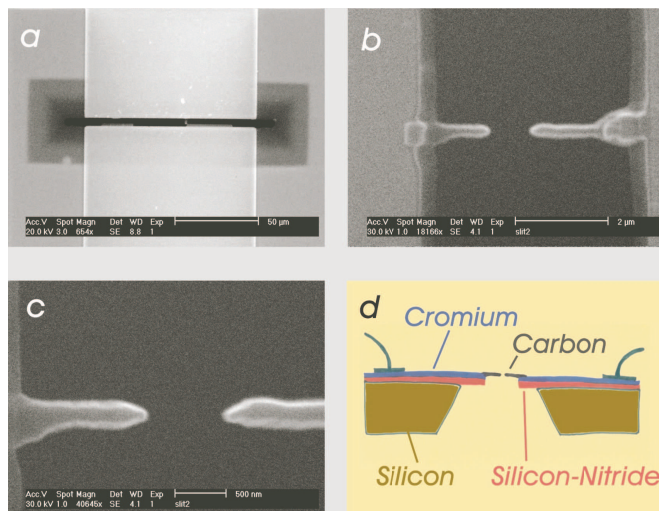


Figure 13.1:

a) Overall view of a silicon nitride membrane with an almost 5 micron wide and about 100 micron long slit and metal contacts at both sides.

b) On this structure we fabricated free standing wires facing each other to create a local electric field. Note that all the higher magnification images are rotated by 90 degrees compared to the SEM image in (a).

c) A closer look at this structure shows a gap width of about 700nm. The radius of curvature at the end of the wires is about 50nm.

d) Schematic side view of the overall structure.

a slit to which we can apply an electric potential to create a local electric field, we employ a 30 keV focused electron beam. The beam decomposes hydrocarbons along a line defined by the slow scanned electron beam. These preliminary studies, carried out in February 2001, seem encouraging since it was already possible to create gap sizes down to 30nm (not shown in the figure). This method thus holds promise for studying even smaller synthetic DNA molecules that can be synthesized to match the gap exactly. Studies to cover the carbon wires with gold and efforts to increase the writing speed to be able to routinely fabricate more complex structures, like multi-terminal devices, are currently in progress.

13.3 Mechanical manipulation of DNA molecules in the liquid phase

We are about to use (diploma thesis of C. Escher, who started in February 2001) optical techniques and local electric fields in a liquid to attach DNA molecules between two glass

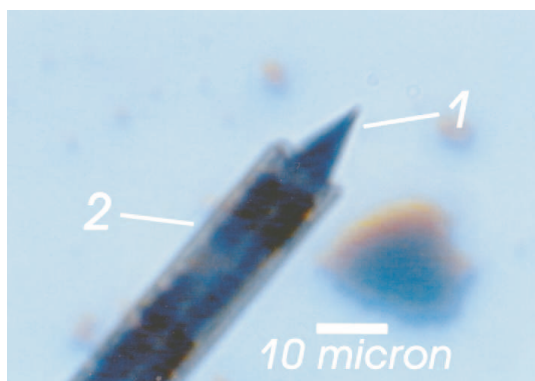


Figure 13.2: Gold tip (1) encapsulated into a glass capillary (2).

pipettes with a conducting gold wire inside. Electric fields of the order of 20 V/cm are applied in electrophoresis to move DNA molecules in solution. We plan to localize electric fields of this order to gap-structures which match the length of the chosen DNA molecules of several micrometer length. In order to be able to distinguish electronic current through the molecules from ionic current in the buffer solution it is necessary to minimize the exposed area of the

gold electrodes. In a first and preliminary experiment it has been possible to draw a glass capillary with a fine gold wire inside to a shape as shown in Fig. 13.2.

The purpose of this type of experiments is to be able to localize a molecule between the two electrodes in order to later mechanically move it to a desired place on a silicon structure. Furthermore it should be possible to explore the mechanism of conductivity in DNA by stretching the molecules or by changing the temperature of the surrounding liquid, just to name two of the various parameters that might effect conductivity. Eventually, we hope to achieve a fairly detailed insight into the conduction mechanism that should help us to relate to current theoretical models, like the polaron assisted hopping mechanism.

13.4 Structural biology of single proteins.

in collaboration with: Andreas Plückthun (Biochemistry Department, University of Zurich)

This effort is part of a National Center of Competence Research project on Nano-Science, headed by Hans-Joachim Güntherodt at the University of Basel. The goal is to obtain information on protein structures. In collaboration with Andreas Plückthun and his group in the biochemistry department, we are about to develop methods to prepare single proteins in such a way as to make them accessible to our LEEPS (Low Energy Electron Point Source) Microscope. We hope to be able to obtain high resolution electron holograms to derive structural information on an individual protein. A high resolution detector and new hologram reconstruction software will be available soon.

13.5 Field-ion microscopy and field-emission studies of single C60 clusters in tungsten tips.

This effort is closely related to the goal of obtaining ultimate resolution in holography with low energy electrons for structural analysis of bio-molecules. By using field ion microscopy techniques, we can characterize and shape a metal tip on the atomic scale. We have designed a dedicated field ion microscope, that is expected to be operational in summer 2001, to deposit single C60 clusters onto a metal tip that has prior been characterized on an atomic scale. The electronic structure of the C60 clusters and their bucky ball shape leads us to believe that such a structure will emit electrons with increased temporal and spatial coherence and in a larger angular regime. The theoretical 3-dimensional resolution in holography, not considering experimental aspects, is half the deBroglie wave length of the electrons. This would correspond, for the electrons we employ, to a theoretical limit of sub-atomic resolution. With this effort we hope to eventually make a significant step in resolution towards the theoretical limit, from the present 1 nm, which is not limited by the coherence of the source but by external disturbances.

Another aspect of this effort relates to surface science studies on C60 clusters carried out in the group of Jürg Osterwalder. We might be able to obtain complementary information by studying just a single adsorption event of an individual C60 cluster.

14 Computer Assisted Physics

P. F. Meier, E. Olbrich, S. Pliberšek, S. Renold, J. Schneider, Y. Shen, and E. Stoll
S. Dangel (until Dec. 00) and H.-R. Moser (until June 00)

In this report, we want to concentrate on the following research topics:

- Interpretation of the properties of high temperature superconductivity materials using spin-polarized theoretical methods
- Non-linear dynamical study with particular reference to time series analysis of electroencephalograms

In particular we selectively report on hyperfine interactions at oxygen nuclei in La_2CuO_4 (14.1.1), on the changes in the microscopic structure induced by dopants (14.1.2), and on local distortions in doped La_2CuO_4 (14.1.3). From the collaborations with two groups of the Medical Faculty we present results of a new analysis of sleep electroencephalograms (14.2).

14.1 Electronic structure of high- T_c materials

14.1.1 Transferred hyperfine fields

One explanation of the variant time dependencies of the nuclear–spin-lattice relaxation rates between planar ^{17}O and ^{63}Cu required that the antiferromagnetic fluctuations cancel at the oxygen site. However, this was not in accord with neutron scattering which showed that these fluctuations were incommensurate. This dichotomy led Zha, Barzykin and Pines (ZBP) [1] to propose that the transferred field at the ^{17}O covered an extensive region in the CuO_2 plane which included significant contributions from at least the next nearest neighbour (NNN) copper ions. This would compensate for the non-perfect cancellation of hyperfine field due to the incommensurability and thus reconcile the NMR and neutron scattering data.

It is not obvious how to test the ZBP proposition experimentally so we embarked on a project using our cluster models to see if we could confirm, or otherwise, the proposition. A whole range of clusters for simulation of the La_2CuO_4 system were studied so that the variation of the Fermi contact term $D(^{17}\text{O})$ could be analyzed in terms of the number n_{NN} of nearest neighbours (NN), and the number n_{NNN} , of next nearest neighbours. The simplest relation we could conceivably use is of the form

$$D(^{17}\text{O}) = c n_{\text{NN}} + c' n_{\text{NNN}}. \quad (14.1)$$

This was found to be quite adequate with the added significance that $c' \approx 0$ as can be seen in Fig. 14.1 where $D(^{17}\text{O})$ is plotted versus n_{NNN} for fixed $n_{\text{NN}} = 2$. This implies that

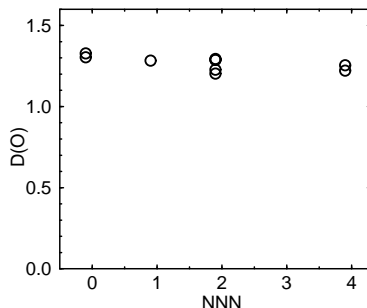


Figure 14.1: *Isotropic contact density at a planar oxygen nucleus as a function of the number of next nearest neighbor copper ions.*

there is no evidence for transferred hyperfine fields on the planar ^{17}O from the next nearest neighbour copper ions. This work does not support the ZBP proposal. It is possible that the dichotomy may be simply due to the difference in detection frequency of the NMR and neutron scattering experiments.

14.1.2 Influence of dopants on the electronic structure of high- T_c materials

Pure La_2CuO_4 is an insulator which becomes metallic and superconducting at low temperatures only by doping, either with excess oxygen or replacing some of the tri-valent lanthanum with bi-valent ions, such as Sr^{2+} .

The role of dopants in high T_c superconductors is generally seen as being limited to the introduction of hole carriers into the CuO_2 plane. This simplified assumption is partly driven by the lack of information on the local atomic and electronic structure around dopants. While experimental evidence favoring inhomogeneous charge distributions of the doped holes is still mounting, the role that dopants play in determining this inhomogeneous ground state, if any, is still unclear.

Conventional band structure calculations are not readily adaptable to studying disrupted periodic structures whereas such cases are more ideally suited for the cluster model. Therefore we can build on the confidence already established with La_2CuO_4 .

Previous work [2] has shown that the cluster model gives results for the electric field gradient, on-site and transferred fields for La_2CuO_4 which compare favourably with NMR experimental data. These more recent examples of the extensive studies carried out on La_2CuO_4 continue to demonstrate why we have increasing confidence in the applicability of the cluster method to model copper oxide high- T_c materials. The natural next step was to begin a study of the effects of doping. The idea that the dopant ions could cause a significant change in the local electronic structure of superconducting cuprates was first introduced in Ref. [4] where it was shown that the important changes in the local molecular orbitals (MOs) as induced by the dopant strontium or interstitial oxygen ions are reflected in the electric field gradient on the neighboring copper nuclei site. This enabled us to resolve a long-standing controversy concerning the interpretation of the nuclear quadrupole resonance spectra in doped La_2CuO_4 on which we briefly reported last year.

With cluster calculations, strontium doping is easily achieved since Sr^{2+} ions substitute some La^{3+} ions unambiguously (see Fig. 14.2) and in the following we compare the results obtained for the undoped system (same cluster as in Fig. 14.2 but with La instead of Sr) and the doped system.

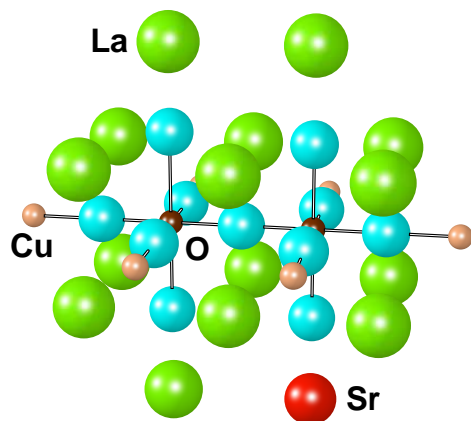


Figure 14.2: The $\text{Cu}_2\text{O}_{11}/\text{Cu}_6\text{SrLa}_{15}$ cluster. For the two central copper atoms (dark) and for the 11 oxygen atoms an all-electron calculation was performed. For the other 6 Cu (bright), Sr and 15 La atoms pseudo-potentials are used.

For both clusters, the lowest unoccupied molecular orbital (LUMO) is an anti-bonding combination of atomic orbitals with $3d_{x^2-y^2}$ on the copper atoms and $2p_\sigma$ on the oxygens. Of particular interest are the changes in the relative energy differences of the occupied molecular orbitals dominated by the copper d_{zx} , d_{yz} , and d_{xy} orbitals. Some of these calculated MOs are given diagrammatically in Fig. 14.3, where $\Delta E_{0,n}$ denotes the energy difference between the LUMO and the particular n^{th} MO.

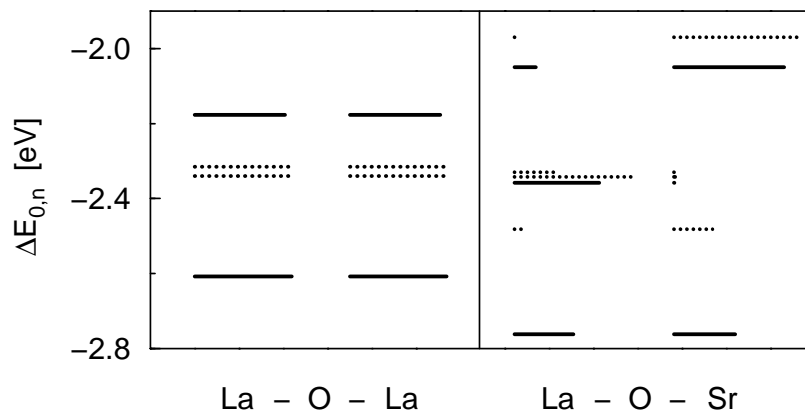


Figure 14.3: Energy differences between the LUMO and the highest occupied MOs in the clusters described in Fig. 14.1 with contributions from atomic $3d_{zx}$ orbitals (solid bars) and $3d_{yz}$ orbitals (dashed bars). The length of the bar is proportional to the square of the expansion coefficient of the MO into the corresponding atomic orbitals.

In the left panel the MOs are equally shared by the two Cu atoms as required by symmetry. There are two orbitals for each zx and yz symmetry because there are two Cu atoms. Note that both are anti-bonding linear combinations with O atomic orbitals. The bonding orbitals are deeper in energy and are not shown here. There is a considerable split in energy for the $3d_{zx}$ orbitals and the $3d_{yz}$ orbitals in the right panel of the figure where the symmetry is broken due to the presence of the Sr^{2+} . Since the d_{yz} orbital pair behaves qualitatively in the same way as the d_{zx} orbital pair we will concentrate on the d_{zx} orbital pair only. The one of lower energy is largely confined to the left site as shown in Fig. 14.4b whereas the higher energy one is localized on the right site as shown in Fig. 14.4c. This is not surprising and a

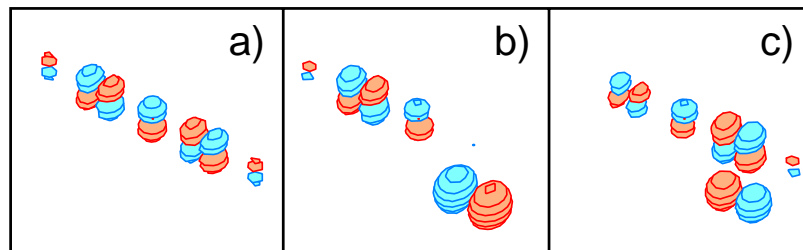


Figure 14.4: Three selected molecular orbitals with dominant $3d_{zx}$ character on the coppers. The red regions indicate negative sign. a) undoped and $\Delta E_{0,zx} = -2.18$ eV. b) with Sr and $\Delta E_{0,zx} = -2.36$ eV. c) with Sr and $\Delta E_{0,zx} = -2.05$ eV. Note the substantially extended $2p_x$ orbital on the apex oxygen atom between the Cu and the Sr atom.

number of rationalizations can be forwarded linking the origin to the proximity of the higher positive charge of the La^{3+} ion compared to the Sr^{2+} ion.

The additional splitting of the MOs in the right panel is due to different admixtures of $2p_z$ contributions from the apical oxygen that bridges the Cu site and the Sr. The MOs with $3d_{xy}$ character are not shown in Fig. 14.3 since they show no substantial difference between the doped and undoped clusters.

We thus find a rearrangement of the local electronic structure upon doping. This then involves a change in the spin-orbit contribution A_{so}^α to the hyperfine field which will influence the nuclear spin-lattice relaxation times. We estimate an increase in A_{so}^x and A_{so}^y of about 15 to 20 %.

14.1.3 Local distortions in doped La_2CuO_4

In recent years, the experiments that probe the local structure have indicated the presence of significant local distortions in high-temperature superconductors. These structural deformations were attributed to the inhomogeneous charge distributions of a stripe phase. First clear evidence of this behaviour was obtained when Bianconi et al. [5] performed Cu K -edge extended x-ray absorption fine structure (EXAFS) on $\text{La}_{1.85}\text{Sr}_{0.15}\text{CuO}_4$. They found a bimodal length distribution for both Cu-O(ap) and Cu-O(pl) distances. In particular, an anomalously short Cu-O(ap) bond length of 2.30 Å was observed and attributed to the CuO_6 octahedra in the presence of an additional, extrinsic hole. This proposal was investigated in our recent first principles study [6] in which the distance between the copper and the apical oxygen, O(ap), was calculated for a cluster model with two different charge states: for a $(\text{CuO}_6)^{10-}$ ion (model A) and for a $(\text{CuO}_6)^{9-}$ ion (model A^+). Model A simulated the copper environment away from dopant ions, extrinsic holes, or any other defects, whereas model A^+ differed from model A by the presence of an additional extrinsic hole. It was assumed that the extrinsic-intrinsic hole pair for model A^+ forms a singlet state. The dependence of the energy as a function of the Cu-O(ap) distance is shown in Fig. 14.5. Note that the equilibrium O(ap)

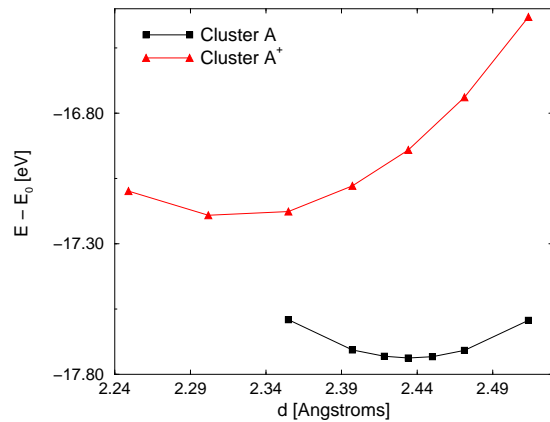


Figure 14.5: *Dependence of the ground-state energy on the Cu-O(ap) distance for model A and model A^+ .*

location in cluster model A is shifted by $\delta_z = +0.04$ Å from the initial position at $z = 2.40$ Å which is attributed to the finite size of the cluster used. From Fig. 14.5 it can be seen that a localized hole induces a contraction of the Cu-O(ap) bond length by 0.12 Å which is in excellent agreement with the EXAFS investigation which obtain an anomalous Cu-O(ap) distance that was shortened by 0.1 Å with respect to the normal crystallographic distance of 2.40 Å as observed in the parent La_2CuO_4 . The presented results of our study thus confirm the proposed interpretation for the observation of anomalous Cu-O(ap) distance in optimally doped La_2CuO_4 .

14.2 Time series analysis of EEG

In the last decade, the time-series analysis of electroencephalograms (EEGs) by means of methods derived from nonlinear dynamics has attracted increased attention [7]. Traditionally the EEG is characterized mainly by linear properties such as the spectral power in certain frequency ranges. In contrast, nonlinear measures focussed in particular on the dimensional complexity (DC) [8], a measure based on the correlation dimension D_2 . In this way a whole segment of an EEG is characterized by a single number. This amounts on the one hand to a strong data reduction, which is often very useful, and has on the other hand a plausible interpretation, i.e. the number of active degrees of freedom. The latter can also be interpreted as the degree of synchronization of the apparently high-dimensional neural dynamics. This interpretation is consistent with the estimates of the dimensional complexity in different psycho-physiological states from the EEG [9, 10] and the general ideas about the character of the neural dynamics in these states.

There is, however, clear evidence from the theory of nonlinear dynamics that the observed values of the dimensional complexity cannot simply be interpreted as dimensions of fractal attractors. Moreover, it was shown that surrogate time series of EEGs, i.e. time series, which resemble the linear properties of the original time series but are random otherwise, exhibit almost the same dimensional complexity as the original ones.

Starting from these findings we undertook a thorough investigation of the following two questions: Up to which extent does the dimensional complexity characterize only linear, i.e. spectral properties of the time series? And if so, which spectral properties are reflected in the dimensional complexity.

To demonstrate the simultaneous occurrence of both linear and nonlinear features in an EEG we investigated several all-night sleep EEGs. We obtained these data together with the sleep stage scores (REM, non-REM stages I, II, III, IV) from the Sleep Laboratory of the Institute of Pharmacology. We determined the correlation dimension D_2 using the Grassberger-Procaccia algorithm and the self-similarity exponent α by means of a detrended fluctuation analysis. The exponent α measures the persistence of a time series. Time series corresponding to values of α less than 1.5 have a tendency to turn back upon themselves. On the other hand, for α -values greater than 1.5, the time series has a tendency to be persistent in its progression in the direction in which it was moving. The latter property is known as persistence.

First, we analyzed 300 artifact-free EEG-segments of 1 minute duration, which were selected from four all-night sleep recordings, by applying the methods mentioned above. We divided the EEG-segments during sleep stage II into two subgroups: segments containing K-complexes and/or vertex waves were assigned to group II_B and those without such spikes to group II_A . In Fig. 14.6 we plotted the α -values on the ordinate against the D_2 -values on the abscissa. It is seen that during REM sleep (\circ) α is small and DC large. This is reversed during deep sleep (stages III/IV, \triangle). As concerns sleep stage II, the subgroup II_A follows the general trend between α and DC. The subgroup II_B , however, deviates. This indicates that the values of DC are much less affected by the occurrence of spikes in group II_B than the estimates of α . In general, it is evident that the α exponent can also distinguish different sleep stages. On the other hand, Fig. 14.6 makes clear that the α -values are negatively correlated with the estimated D_2 .

Furthermore, we calculated DC and α for non-overlapping consecutive 1 minute long epochs from all-night sleep EEG-recordings. An inverse covariation between DC and α was detected as is seen in Fig. 14.7, where the variations of DC and α are plotted. One sees that both time variations reflect the cyclic changes in sleep dynamics which coincide with

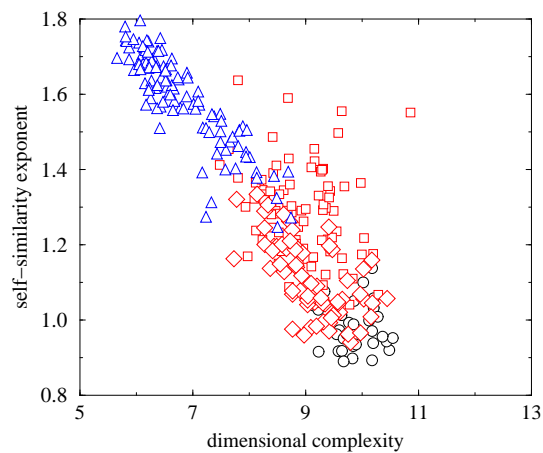


Figure 14.6: *Self-similarity exponent α vs. dimensional complexity D_2 .*

- \triangle : sleep stage III/IV
- \diamond : sleep stage group II_A
- \square : sleep stage group II_B
- \circ : REM sleep

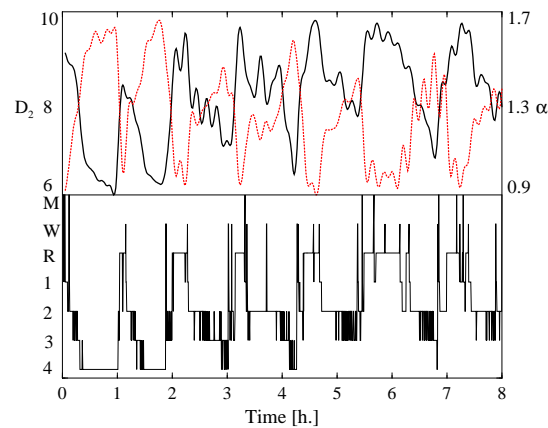


Figure 14.7: *The smoothed time courses of dimensional complexity D_2 (solid line in upper panel) and self-similarity α exponent (dotted line in upper panel) reflect the sleep stage scores (lower panel) and exhibit the inverse covariation.*

the sleep stage scores. The inverse covariation between DC and α and the fact that the DC-values of EEG-signals differ only slightly from those of surrogates led us to conclude that the DC measures mainly a linear property of EEG-signals – the persistence. Nevertheless, the deviations from this overall behaviour, as observed e.g. in sleep stage II, are valuable for further insights regarding the character of the EEG signals and will be the object of further research.

References

- [1] Y. Zha, V. Barzykin, and D. Pines, *Phys. Rev. B* **54**, 7561 (1996).
- [2] P. Hüsser, H. U. Suter, E. P. Stoll, and P. F. Meier, *Phys. Rev. B* **61**, 1567 (2000).
- [3] E. P. Stoll, S. Pliberšek, S. Renold, T. A. Claxton, and P. F. Meier *J. Supercond. Inc. Nov. Magn.* **13**, 971-975 (2000).
- [4] S. Pliberšek and P. F. Meier, *Europhys. Lett.* **50**, 789 (2000).
- [5] A. Bianconi et al., *Phys. Rev. Lett.* **76**, 3412 (1996).
- [6] S. Pliberšek, E. P. Stoll, and P. F. Meier, *Journal of Superconductivity* **13**, 921 (2000).
- [7] *CHAOS IN BRAIN ?*, edited by K. Lehnertz, J. Arnhold, P. Grassberger, and C.E. Elger, World Scientific, 1999.
- [8] W. S. Pritchard and D. W. Duke, *Int. J. Neuroscience* **67**, 31 (1992).
- [9] P. Achermann, R. Hartmann, A. Gunzinger, W. Guggenbühl, and A. A. Borbely, *European Journal of Neuroscience* **6**, 497 (1994).
- [10] K. Lehnertz and C. E. Elger, *Phys. Rev. Lett.* **80**, 5019 (1998).

15 Mechanical Workshop

B. Schmid, K. Bösiger, P. Treier, B. Wachter, B. Zaugg, A. Rochat, (apprentice) und Y. Steiger (apprentice)

During the past year the mechanical shops were mostly occupied with work for the different research projects described in this report. As a consequence orders from other institutes of the University of Zürich and from the outside made up for only a small part of the shop activity. More than 30 institutes make, however, use of the metal and other technical material supply stores maintained by the shop³.

Major projects which deserve mentioning are the following:

- H1-collaboration at DESY upgrade project (groups Straumann and Truöl, see Sect. 7): After the successful construction of a prototype for the new cylindrical proportional chamber (CIP) in 1999, the full five-layer detector was completed in January 2001. This project required more than 7800 man-hours, and the temporary employment of two DESY technicians during several months. The complexity and novelty of many techniques used in the construction forced us to make many dedicated tests. The successful completion was only possible with a considerable amount of patience and overtime of all persons involved. Figures 15.1 to 15.3 illustrate some of the construction steps. The items listed in Table 15.1 should provide a feeling for the size of the project.

Table 15.1: *Materials used in the CIP construction.*

Rohacell	25 m ² × 1.5 mm
Al-foil	32 m ² × 25 μm
Cathode foil (Cu pads)	12 m ² × 25 μm
Special high voltage connectors produced	240
Coaxial cables from cathode pad to signal connector	9000
Soldering connections	16680
Signal connectors soldering points	80 × 120
Anode wires	2400, 5.28 km, φ 25 μm
Araldit glue	10 kg
Total weight of chamber	35 kg

- Surface physics group (Group Osterwalder, see Section 12): Two bi-axial and one tri-axial goniometer, to be used in ultra-high vacuum for photoelectron diffraction were manufactured. A second project concerned a photocathode electron gun for time resolved electron diffraction (see Figures 15.6 to 15.8).

³For a catalogue see <http://www.physik.unizh.ch/groups/werkstatt/dienstleistung.html>



Figure 15.1: A Rohacell cylinder on its mandril is being prepared for polishing.



Figure 15.2: The grooves for the cables transmitting the cathode signals to the end flanges are filled with glue.



Figure 15.3: A completed detector cylinder is prepared for removal from the mandril.

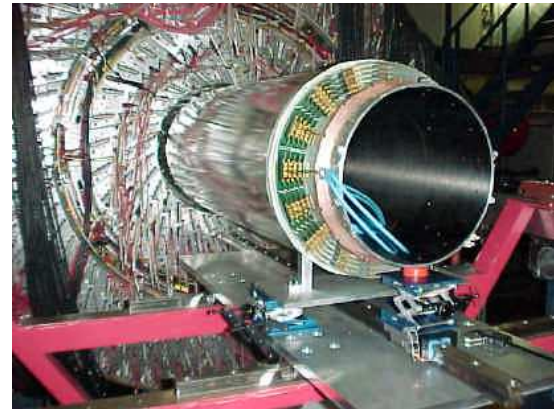


Figure 15.4: The new CIP is being mounted into the H1 central tracker.

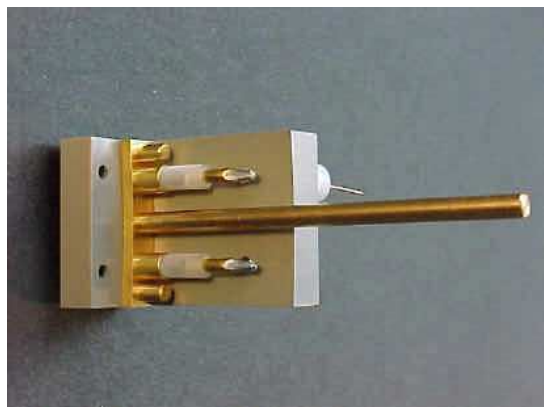


Figure 15.5: Special high-voltage connector.

Pictures from the
H1-collaboration
upgrade project.

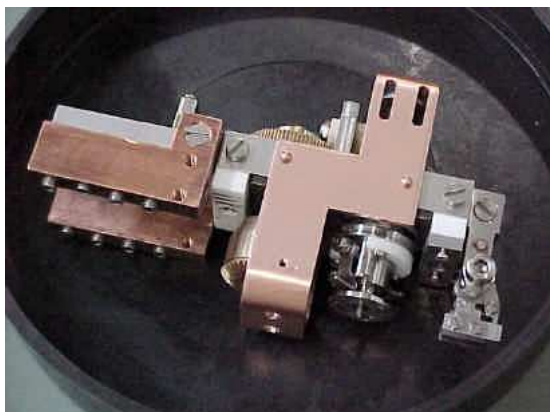


Figure 15.6: *Sample goniometer with five degrees of freedom for photoelectron diffraction - after construction.*

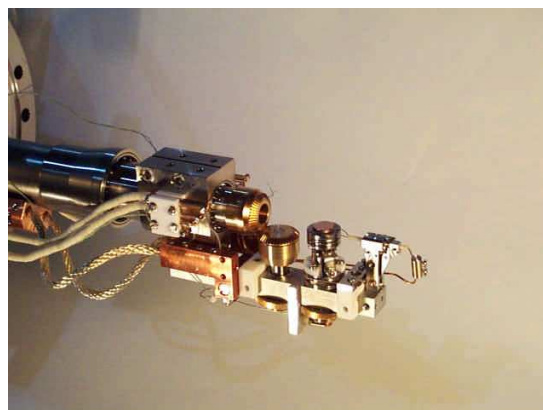


Figure 15.7: *Completed sample goniometer with five degrees of freedom for photoelectron diffraction - in position on the vacuum flange with supplies.*

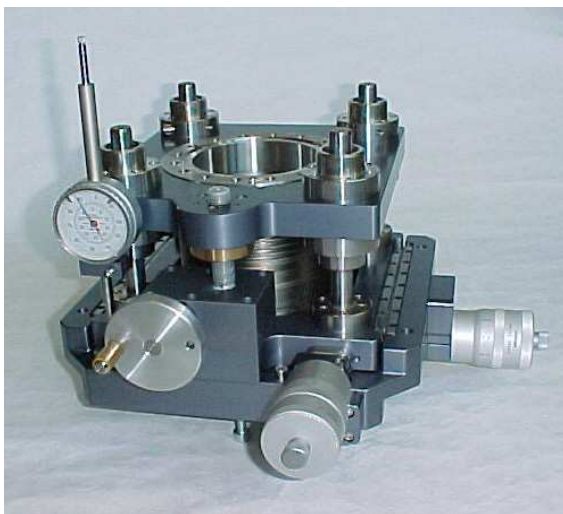


Figure 15.8: *Three axis positioning stage used in ultrahigh vacuum for the surface physics group.*

Pictures from projects
for the surface physics
group.

16 Publications

16.1 Research group of Prof. C. Amsler

Articles

- Test of $\bar{N}N$ potential models: Isospin relations in $\bar{p}d$ annihilations at rest and the search for quasinuclear bound states
A. Abele et al. (Crystal Barrel Collaboration)
Eur. Phys. Journal C 17 (2000) 583
- $\bar{p}p$ -annihilation into $\omega\pi^0$, $\omega\eta$ and $\omega\eta'$ at 600, 1200 and 1940 MeV/c
A. Abele et al. (Crystal Barrel Collaboration)
Eur. Phys. Journal C 12 (2000) 429
- Branching ratios for $\bar{p}p$ annihilation at rest into two-body final states
A. Abele et al. (Crystal Barrel Collaboration)
Nucl. Phys. A 679 (2001) 563
- Review of Particle Physics
D.E. Groom et al. (Particle Data Group)
Eur. Phys. Journal C 15 (2000) 1
- Particle Physics Booklet
D.E. Groom et al. (Particle Data Group)
Springer (2000)
- Hadron Spectroscopy
C.Amsler
Proc. of the XVth Particles and Nuclei International Conference (PANIC),
Nucl. Phys. A 663 (2000) 93c
- Proton-antiproton annihilation into 6γ and 7γ
C. Amsler
Proc. 8th Int. Conf. on Hadron Spectroscopy, Beijing (1999),
Nucl. Phys. A 675 (2000) 67c
- C. Regenfus
Pontecorvo reactions with strangeness production on deuterium
Proc. of the XVth Particles and Nuclei International Conference (PANIC),
Nucl. Phys. A 663 (2000) 577c

Articles in press

- Study of f_0 Decays into Four Neutral Pions
A. Abele et al. (Crystal Barrel Collaboration)
Eur. Phys. Journal C
- 4π -decays of scalar and vector mesons
A. Abele et al. (Crystal Barrel Collaboration)
Eur. Phys. Journal C
- A High Resolution Search for the Tensor Glueball Candidate $\xi(2230)$
A. Abele et al. (Crystal Barrel Collaboration)
Phys. Lett. B
- A high resolution silicon beam telescope
C. Amsler et al.
Nucl. Instr. Meth. in Physics Research A

- Temperature dependence of pure CsI scintillation light yield and decay time
C. Amsler et al.
Nucl. Instr. Meth. in Physics Research A
- Antihydrogen Production and Precision Spectroscopy with ATHENA / AD1
C. Amsler et al. (ATHENA Collaboration)
Proc. Hydrogen II Conf., Castiglione de Pescaia, Springer (2000)
- Proton-antiproton annihilation into $\pi^0\pi^0\pi^0$, $\pi^0\pi^0\eta$ and $\pi^0\eta\eta$ at 900 MeV/c
C. Amsler
Proc. of the Hirscheegg Workshop on Hadron Spectroscopy, 14 - 20 January 2001
- Lorentz-angle in irradiated silicon
R. Kaufmann and B. Henrich
Nucl. Instr. and Methods in Phys. Research A
- Performance of ultra-thin silicon detectors in a 5 MeV antiproton beam
P. Riedler
Proc. of the 9th Vienna Conference on Instrumentation, 19 - 23 February 2001
- Development of the ATHENA vertex detector
P. Riedler
Proc. Int. Conf. on the Intersections between Particle and Nuclear Physics,
Quebec City, 2000
- Detection of antihydrogen with a Si- μ -strip and CsI-crystal detector at
cryogenic temperature
C. Regenfus
Proc. of the XXXth Int. Conf. on High Energy Physics, Osaka,
27 July to 2 August 2000

Diploma and PhD theses

- Search for New Mesons in Proton-Antiproton Annihilation into $\omega\pi^0\pi^0$ and $\omega\eta\pi^0$
P. Giarritta
Dissertation, Universität Zürich (2000)
- Proton-Antiproton Annihilation into Three Pseudoscalar Mesons at 900 MeV/c
M. Heinzemann
Dissertation, Universität Zürich (2000)

Invited Lectures

- C. Amsler
Invited talk, Korean-Swiss Seminar on Particle Physics, Pohang, Republic of Korea,
25.7.00
"Particle Physics in Switzerland"
- C. Amsler
Invited talk, Korean-Swiss Seminar on Particle Physics, Pohang, Republic of Korea,
26.7.00
"Antihydrogen Production with ATHENA"
- C. Amsler
Invited talk, Hirscheegg Workshop on Hadron Spectroscopy, Hirscheegg, Austria, 18.1.01
"Proton-antiproton annihilation into $\pi^0\pi^0\pi^0$, $\pi^0\pi^0\eta$ and $\pi^0\eta\eta$ at 900 MeV/c"

- C. Regenfus
Invited talk, Korean-Swiss Seminar on Particle Physics, Pohang, Republic of Korea, 25.7.00
"Development of Silicon Pixel Detectors for CMS"
- C. Regenfus
Contributed talk, XXXth Int. Conf. on High Energy Physics, Osaka, 28.7.00
"Detection of antihydrogen with a Si-Microstrip and CsI-crystal detector"
- P. Riedler
Seminar, Cambridge University, 16.5.00
"Antihydrogen Production at ATHENA"
- P. Riedler
Development of the ATHENA vertex detector
Contributed talk, ICOHEPANS, Int. Conf. on High Energy Physics and Nuclear Structure, Quebec City, 3.6.00
"Development of the ATHENA vertex detector"
- P. Riedler
Contributed talk, 9th Vienna Conference on Instrumentation, 21.2.01
"Performance of ultra-thin silicon detectors in a 5 MeV antiproton beam"

ATHENA Collaboration:

C. Amsler, G. Bendiscioli, G. Bonomi, P. Bowe, M. Charlton, M. Collier, M. Doser, K. Fine, A. Fontana, M.C. Fujiwara, R. Funakoshi, J. Hangst, R.S. Hayano, H. Higaki, M. Holzschneider, W. Joffrain, L. Jorgensen, D. Kleppner, V. Lagomarsino, R. Landua, C. Lenz Cesar, D. Lindelöf, E. Lodi-Rizzini, M. Macri, G. Manuzio, M. Marchesotti, P. Montagna, H. Pruys, C. Regenfus, P. Riedler, A. Rotondi, G. Rouleau, P. Salvini, T. Speer, G. Testera, D.P. van der Werf, T. Watson, T. Yamazaki, Y. Yamazaki, A. Zenoni

CRYSTAL BARREL Collaboration (Authors may vary with publication):

A. Abele, J. Adomeit, C. Amsler, D.S. Armstrong, C.A. Baker, B.M. Barnett, C.J. Batty, M. Benayoun, A. Berdoz, R. Berlich, K. Beuchert, P. Birien, S. Bischoff, J. Bistirlich, P. Blüm, R. Bossingham, K. Braune, J. Brose, D.V. Bugg, T. Case, S.U. Chung, A.R. Cooper, O. Cramer, K.M. Crowe, T. Degener, H.P. Dietz, N. Djaoshvili, S. v. Dombrowski, M. Doser, W. Dünneweber, D. Engelhardt, M. Englert, M.A. Faessler, C. Felix, P. Giarritta, R. Hackmann, R.P. Haddock, F.H. Heinsius, M. Heinzelmann, M. Herz, N.P. Hessey, P. Hidas, C. Holzhausen, P. Illinger, D. Jamnik, H. Kalinowski, B. Kalteyer, B. Kämmele, P. Kammel, T. Kiel, J. Kisiel, E. Klempt, H. Koch, M. Kobel, C. Kolo, M. Kunze, M. Lakata, R. Landua, J. Lüdemann, H. Matthäy, R. McCrady, J.P. Merlo, J. Meier, C.A. Meyer, L. Montanet, A. Noble, R. Ouared, F. Ould-Saada, K. Peters, C. Pietra, C.N. Pinder, G. Pinter, S. Ravndal, C. Regenfus, J. Reißmann, S. Resag, W. Roethel, E. Schäfer, P. Schmidt, M. Schüttrumpf, I. Scott, R. Seibert, S. Spanier, H. Stöck, C. Straßburger, U. Strobusch, M. Suffert, U. Thoma, H. Thuemmel, M. Tischhäuser, D. Urner, C. Völcker, F. Walter, D. Walther, U. Wiedner, N. Winter, J. Zoll, B.S. Zou, Č. Zupančič.

Particle Data Group (2000):

D.E. Groom, M. Aguilar-Benitez, C. Amsler, R.M. Barnett, C.D. Carone, C. Caso, G. Conforto, O. Dahl, M. Doser, S. Eidelman, J.L. Feng, L. Gibbons, M. Goodman, C. Grab, A. Gurtu, K. Hagiwara, K.G. Hayes, J.J. Hernandez, K. Hikasa, K. Honscheid, C. Kolda,

M. Mangano, A. Manohar, A. Masoni, K. Mönig, H. Murayama, K. Nakamura, S. Navas, K. Olive, L. Pape, A. Piepke, M. Roos, M. Tanabashi, N.A. Tornqvist, T.G. Trippe, P. Vogel, C.G. Wohl, R.L. Workman, W.M. Yao, B. Armstrong, J.L. Casas Serradilla, B.B. Filimonov, P.S. Gee, S.B. Logowsky, F. Nicholson

16.2 Research group of Prof. R. Engfer

Diploma and PhD theses

- Suche nach der Myon-Elektron-Konversion $\mu^- \text{Au} \rightarrow e^- \text{Au}$ mit SINDRUM II
Georg Kurz
PhD thesis, Zürich University, 2001
- Suche nach der Leptonflavor verletzenden Myon-Elektron-Konversion in Gold: $\mu^- \text{Au} \rightarrow e^- \text{Au}$
Felix Rosenbaum
PhD thesis, Zürich University, 2001

Invited lectures

- P. Wintz
Status of $\mu \rightarrow e$ Conversion at PSI
Workshop on *New Initiatives in Lepton Flavor Violation and Neutrino Oscillations with Very Intense Muon and Neutrino Sources*, East-West Center, University of Hawaii, Honolulu, Hawaii, USA, October 2-6, 2000
- A. van der Schaaf
Rare muon decays
Plenary ECFA meeting, CERN, 23-23 October 2000
- A. van der Schaaf
Rare muon decays at a neutrino factory
IPPP Workshop on *Physics at a future Neutrino Factory*, Durham, UK, March 21-23, 2001

16.3 Research group of Prof. H.-W. Fink

Articles

- Hans-Werner Fink
Electrical conduction through DNA molecules,
In "Electronic properties of novel materials: Molecular Nanostructures"
American Institute of Physics
- Hans-Werner Fink
DNA and Conduction Electrons
Visions and Reflections Article in Cellular and Molecular Life Sciences 58 (2001) 1-3
Birkhäuser Verlag Basel

Invited Lectures

- Hans-Werner Fink
Physik mit kohärenten Elektronenwellen
Physikalische Gesellschaft Zürich, 13. 1. 2000

- Hans-Werner Fink
Electric Conduction through DNA Molecules
XIV International Winterschool on Electronic Properties of Novel Materials,
Kirchberg, Austria, 6. to 10. 3. 2000
- Hans-Werner Fink
Electric Conduction through DNA Molecules
March Meeting American Physical Society, Minneapolis, USA, 20 to 24. 3. 2000
- Hans-Werner Fink: American Physical Society Press conference on the possibilities of
DNA based electronics, Minneapolis, USA, 22. 3. 2000
- Hans-Werner Fink
Abbildung und Manipulation einzelner Moleküle mit Hilfe der Elektronenholografie
Kolloquium der Physikalischen Chemie der Universität Hannover, 29. 3. 2000
- Hans-Werner Fink
Abbildung und Manipulation einzelner Moleküle mit Hilfe der Elektronenholografie
Seminar der Physikalischen Chemie der Universität Zürich, 9. 6. 2000
- Hans-Werner Fink
DNA and Molecular Electronics
Physics Seminar of the CNRS Marseille, 4.5.2000
- Hans-Werner Fink
Transmission Holography for Imaging and Manipulating Individual Molecules
IUVSTA Workshop on Holography and other Direct Methods
Hong Kong, China, 14. to 18. 8. 2000
- Hans-Werner Fink
Coherent field electron sources and its applications
EUROFE 2000 European Field Emission Workshop
Segovia, Spain, 25. to 29. 9. 2000
- Hans-Werner Fink
Probing the Electrical Conductivity of Molecules
International Workshop on the Mesoscopic Physics
Monte Verita, Ascona, Switzerland, 8. to 13.10. 2000
- Hans-Werner Fink
A new tool to image and manipulate individual biomolecules
Pharmakologisches Seminar der Universität Zürich, 12. 12. 2000

16.4 Research group of Prof. H. Keller

Articles

- Recent experimental insights into HTSC materials
K.A. Müller
Physica C **341-348**, 11-18 (2000)
- D-XY critical behavior in cuprate superconductors
T. Schneider and J.M. Singer
Physica C **341-348**, 87-91 (2000)
- T. Schneider and J.M. Singer,
in: *Phase Transition Approach To High Temperature Superconductivity*,
Imperial College Press, London, 2000

- From phase separation to stripes
K.A. Müller
in: *Stripes and Related Phenomena*,
edited by Bianconi and Saini, Kluwer/Plenum Publishers, (New York, 2000) (pp. 1-8)
- Large isotope effect on the pseudogap in the high-temperature superconductor $\text{HoBa}_2\text{Cu}_4\text{O}_8$
D. Rubio Temprano, J. Mesot, S. Janssen, K. Conder, A. Furrer, H. Mutka, and K.A. Müller
Phys. Rev. Lett. **84**, 1990-1993 (2000)
- Large copper isotope effect on the pseudogap in the high-temperature superconductor $\text{HoBa}_2\text{Cu}_4\text{O}_8$
D. Rubio Temprano, J. Mesot, S. Janssen, K. Conder, A. Furrer, A. Sokolov, V. Trounov, S.M. Kazakov, J. Karpinski, and K.A. Müller
Eur. Phys. J. B **19**, 5-8 (2000)
- Magnetische Flusslinien in Hochtemperatur-Supraleitern
H. Keller
Vierteljahrsschrift der Naturforschenden Gesellschaft in Zürich, **145/4**, 153-160 (2000)
- Probing high-temperature superconductivity with positive muons
H. Keller
J. Supercond. **13**, 759-764 (2000)
- Where are we in HTSC?
K.A. Müller
J. Supercond. **13**, 863-866 (2000)
- Universal properties at the quantum superconductor-to-insulator transition of cuprates
T. Schneider and J.M. Singer,
J. Supercond. **13**, 789-791 (2000)
- Tilting mode relaxation and oxygen isotope effect in $\text{La}_{2-x}\text{Sr}_x\text{CuO}_4$ studied by electron paramagnetic resonance
A. Shengelaya, H. Keller, K.A. Müller, B.I. Kochelaev, and K. Conder
J. Supercond. **13**, 955-958 (2000)
- Doping dependence of the effective mass anisotropy and oxygen-isotope effect on the magnetic penetration depth: The role of lattice vibrations in high-temperature superconductivity
J. Hofer, K. Conder, T. Sasagawa, Guo-meng Zhao, T. Schneider, J. Karpinski, M. Willemin, H. Keller, and K. Kishio
J. Supercond. **13**, 963-969 (2000)
- Oxygen-isotope effect on the in-plane penetration depth in underdoped $\text{La}_{2-x}\text{Sr}_x\text{CuO}_4$ single crystals
J. Hofer, K. Conder, T. Sasagawa, Guo-meng Zhao, M. Willemin, H. Keller, and K. Kishio
Phys. Rev. Lett. **84**, 4192-4195 (2000)
- Torque magnetometry on single-crystal high temperature superconductors near the critical temperature: A scaling approach
J. Hofer, T. Schneider, J.M. Singer, M. Willemin, H. Keller, T. Sasagawa, K. Kishio, K. Conder, and J. Karpinski
Phys. Rev. B **62**, 631-639 (2000)

- Small-angle scattering from the vortex lattice in high- T_c and other superconductors
S.L. Lee, P.G. Kealey, E.M. Forgan, S.H. Lloyd, T.M. Riseman, D.McK. Paul, S.T. Johnson, Ch. Simon, C. Goupil, A. Pautrat, R. Cubitt, P. Schleger, C. Dewhurst, C.M. Aegerter, and C. Ager
Physica B **276-278**, 752-755 (2000)
- Charge degree of freedom and single-spin fluid model in $\text{YBa}_2\text{Cu}_4\text{O}_8$
A. Suter, M. Mali, J. Roos, and D. Brinkmann
Phys. Rev. Lett. **84**, 4938-4941 (2000)
- Exploring glasses on the microscopic level by NMR: $x\text{LiF} \cdot (1-x)\text{LiPO}_3$
D. Brinkmann, S. Berger, and J. Roos
Proceedings of the 7th Conference of the Asian Society for Solid State Ionics, Fuzhou, China, 29 Nov. - 4 Dec. 2000, in: *Solid State Ionics, Materials and Devices*, edited by B.V.R. Chowdari and Wenji Wang, World Scientific (Singapore, New Jersey, London, Hong Kong, 2000) (pp. 167-176)
- Muon-spin rotation study of the magnetic correlations in $\text{La}_{2-x}\text{Ca}_{1+x}\text{Cu}_2\text{O}_{6+d}$ superconductors
P.W. Klamut, B. Dabrowski, R. Dybziński, Z. Bukowski, A. Shengelaya, R. Khasanov, S. Döttinger, and H. Keller
J. Appl. Phys. **87**, 5558-5560 (2000)
- Anisotropy of the magnetization discontinuity at the vortex-lattice melting in untwinned $\text{YBa}_2\text{Cu}_3\text{O}_{7-\delta}$
A. Schilling, M. Willemin, C. Rossel, H. Keller, R. A. Fisher, N. E. Phillips, U. Welp, W. K. Kwok, R. J. Olsson, and G. W. Crabtree,
Phys. Rev. B **61**, 3592-3603 (2000)
- Oxygen isotope effects in the manganates and cuprates studied by electron paramagnetic resonance
A. Shengelaya, Guo-meng Zhao, H. Keller, K.A. Müller, and K. Conder
in: *New Developments in High Temperature Superconductivity*, ed. J. Klamut *et al.*, Lecture notes in physics (Springer-Verlag, 2000) (pp. 91-99)
- Strong oxygen-isotope effect on the intrinsic resistivity in the ferromagnetic state of manganites
G.M. Zhao, D.J. Kang, W. Prellier, M. Rajeswari, H. Keller, T. Venkatesan, and R.L. Greene
Phys. Rev. B (Rapid Communications) **63**, R60402-60405 (2001)
- Unusual electrical transport mechanism in the ferromagnetic state of the magnetoresistive manganites
G.M. Zhao, H. Keller, and W. Prellier
J. Phys.: Condens. Matter **12**, L361-366 (2000)
- Double-exchange and the cause of the ferromagnetism in doped manganites
G.M. Zhao
Phys. Rev. B **62**, 11 639-11 643 (2000)
- Large oxygen-isotope effect in $\text{Sr}_{0.4}\text{K}_{0.6}\text{BiO}_3$: evidence for phonon-mediated superconductivity
G.M. Zhao, K. Conder, M. Angst, S.M. Kazakov, J. Karpinski, M. Maciejewski, C. Bougerol, J.S. Pshirkov, and E.V. Antipov
Phys. Rev. B (Rapid Communications) **62**, R11 977-11 980 (2000)

- Evidence for the immobile bipolaron formation in the paramagnetic state of the magnetoresistive manganites
G.M. Zhao, Y.S. Wang, D.J. Kang, W. Prellier, M. Rajeswari, H. Keller, T. Venkatesan, C.W. Chu, and R.L. Greene
Phys. Rev. B (Rapid Communications) **62**, R11 949-11 952 (2000)
- Electrical transport in the ferromagnetic state of manganites: Small polaron metallic conduction at low temperatures
G.M. Zhao, V. Smolyaninova, W. Prellier, and H. Keller
Phys. Rev. Lett. **84**, 6086-6089 (2000)
- Argon annealing of the oxygen-isotope exchanged manganite $\text{La}_{0.8}\text{Ca}_{0.2}\text{MnO}_{3+y}$
G.M. Zhao, K. Conder, H. Keller, and K.A. Müller
Phys. Rev. B **62**, 5334-5334 (2000)

Articles in press

- Vortex-lattice melting in $\text{YBa}_2\text{Cu}_3\text{O}_{7-\delta}$ for $H//ab$
A. Schilling, U. Welp, W.K. Kwok, and G.W. Crabtree
Phys. Rev. B
- Tilting mode relaxation in the electron paramagnetic resonance of isotope substituted $\text{La}_{2-x}\text{Sr}_x\text{CuO}_4$: Mn^{2+}
A. Shengelaya, H. Keller, K.A. Müller, B.I. Kochelaev, and K. Conder
Phys. Rev. B
- Bulk experimental evidence of half-metallic ferromagnetism in doped manganites
G.M. Zhao, H. Keller, W. Prellier, and D.J. Kang
Phys. Rev. B

Diploma and PhD theses

- Studies of Intrinsic Magnetic Properties of High Temperature Superconductors by Means of Torque Magnetometry
Jürg Hofer
Dissertation, Physik-Institut, Universität Zürich, 2000
- Bestimmung der Sensitivitäten von Empfangsspulen in der Magnetresonanz-Bildgebung
Philipp Roggwiller
Diplomarbeit, Institut für Biomedizinische Technik der UNI und ETH Zürich, 2000

Conference reports

- Low-energy charge fluctuations in the presence of the pseudo spin gap in $\text{YBa}_2\text{Cu}_4\text{O}_8$
A. Suter, M. Mali, J. Roos, and D. Brinkmann
Physica C **341-348**, 2167-2168 (2000)
- Chain charge fluctuations in $\text{YBa}_2\text{Cu}_4\text{O}_8$ detected via apex oxygen nuclear quadrupolar relaxation
M. Mali, A. Suter, J. Roos, D. Brinkmann, H. Keller, and J. Karpinski
Physica C **341-348**, 2169-2170 (2000)
- EPR of $\text{YBa}_2\text{Cu}_3\text{O}_{6+y}$: models of paramagnetic centers with $g \approx 4.2$
R. Eremina, M. Eremin, M. Gafurov, V. Ivanshin, I. Kurkin, S. Kurzin, H. Keller, and M. Gutmann
Physica B **284-288**, 917-918 (2000)

- Charge fluctuations in the high- T_c superconductor $\text{YBa}_2\text{Cu}_4\text{O}_8$ observed by ^{17}O NMR
J. Roos, M. Mali, A. Suter, D. Brinkmann, and H. Keller
30th Congress AMPERE on Magnetic Resonance and Related Phenomena, Lisbon, Portugal, 23-28 July, 2000
- Anisotropy of the magnetization discontinuity at the vortex-lattice melting in untwinned $\text{YBa}_2\text{Cu}_3\text{O}_{7-\delta}$
A. Schilling
Gordon Research Conference on Superconductivity, Ventura, CA (USA), 13 February, 2000

Invited Lectures

- H. Keller
Probing high-temperature superconductivity with muons
Conference on *Major Trends in Superconductivity in the New Millennium*
Klosters, Switzerland, 31 March-6 April, 2000
- T. Schneider
Universal properties at the quantum superconductor-to-insulator transition of cuprates
Conference on *Major Trends in Superconductivity in the New Millennium*
Klosters, Switzerland, 31 March-6 April, 2000
- J. Hofer
Oxygen-isotope effect on the magnetic penetration depth in underdoped $\text{La}_{2-x}\text{Sr}_x\text{CuO}_4$
Symposium on *Itinerant and Localized States in HTSC*
Klosters, Switzerland, 6-10 April, 2000
- Guo-meng Zhao
Experimental constraints on the physics of cuprates and manganites
Symposium on *Itinerant and Localized States in HTSC*
Klosters, Switzerland, 6-10 April, 2000
- A. Shengelaya
Tilting mode relaxation and oxygen isotope effect in $\text{La}_{2-x}\text{Sr}_x\text{CuO}_4$ studied by electron paramagnetic resonance
Symposium on *Itinerant and Localized States in HTSC*
Klosters, Switzerland, 6-10 April, 2000
- Guo-meng Zhao
Unconventional isotope effects in manganites and cuprates
Department of Physics, Montana State University, USA, 17 April, 2000
- A. Schilling
Superconducting ceramics: materials of atoms, matter of vortices
Universität Karlsruhe, Germany, 18 May, 2000
- Guo-meng Zhao
Experimental constraints on the physics of cuprates and manganites
Department of Physics, University of Geneva, Switzerland, 23 May, 2000
- H. Keller
Vortexmaterie und Myonen in Hochtemperatur-Supraleitern
Universität Augsburg, Germany, 19 June, 2000

- H. Keller
Probing high-temperature superconductivity with muons
Trends in Condensed Matter Physics
Monte Verità, Ascona, Switzerland, 3-8 September, 2000
- A. Schilling
Phase transitions and thermodynamic data of vortex matter in $\text{YBa}_2\text{Cu}_3\text{O}_{7-\delta}$
Trends in Condensed Matter Physics
Monte Verità, Ascona, Switzerland, 3-8 September, 2000
- J. Roos
High-pressure solid state NMR/NQR investigations.
AMPERE Summer School: *Applications of Magnetic Resonance in Novel Materials*,
Nafplion, Greece, 3-9 September, 2000
- Guo-meng Zhao
Experimental constraints on the physics of cuprates and manganites
Second International Summer School on Strongly Correlated Systems, Debrecen, Hun-
gary, 4-9 September, 2000
- A. Schilling
Phase transitions in vortex matter
Physikalisch-Chemisches Institut der Universität Zürich, 11 January, 2001
- Guo-meng Zhao
Experimental constraints on the physics of cuprates
Texas Center for Superconductivity at the University of Houston, USA, 23 January,
2001
- Guo-meng Zhao
Unconventional isotope effects in the high-temperature cuprate superconductors and
colossal magnetoresistive manganites
University of South Carolina, Columbia, USA, 25 January, 2001
- H. Keller
Oxygen-isotope effect on the magnetic penetration depth in cuprate superconductors
Workshop on the Phase Diagram of High-Temperature Superconducting Copper Oxides
Max-Planck Institut Stuttgart, Germany, 5-7 March, 2001
- M. Mali
Oxygen isotope effect of the spin pseudogap in $\text{YBa}_2\text{Cu}_4\text{O}_8$ as determined by NMR
Workshop on the Phase Diagram of High-Temperature Superconducting Copper Oxides
Max-Planck Institut Stuttgart, Germany, 5-7 March, 2001

16.5 Research group of Prof. P. F. Meier

Articles

- Cluster Calculations of the Hyperfine Interactions in Superconducting Copper Com-
pounds
P. F. Meier, T. A. Claxton, P. Hüsser, S. Pliberšek, and E. P. Stoll
Z. Naturf., **55 a**, 247-255 (2000)
- First-principles Calculations of Hyperfine Interactions in La_2CuO_4
P. Hüsser, H. U. Suter, E. P. Stoll, and P.F. Meier
Phys. Rev. B **61**, 1567-1579 (2000)

- Electronic Structure of Barium Hexaboride
S. Massidda, R. Monnier, and E. Stoll
Eur. Phys. J. B **17**, 645-649 (2000)
- First Principles Investigation of Local Distortions in Doped La_2CuO_4
S. Pliberšek, E. P. Stoll, and P. F. Meier
J. Supercond. Inc. Nov. Magn. **13**, 921-923 (2000)
- Influence of Spin-Orbit Couplings to Nuclear Spin-Lattice Relaxation Rates in Sr-doped La_2CuO_4
E. P. Stoll, S. Pliberšek, S. Renold, T. A. Claxton, and P. F. Meier
J. Supercond. Inc. Nov. Magn. **13**, 971-975 (2000)
- Interpretation of Nuclear Quadrupole Resonance Spectra in doped La_2CuO_4
S. Pliberšek and P. F. Meier
Europhys. Lett. **50**, 789-795 (2000)
- Quasiparticle Diffusion in Tantalum using Superconducting Tunnel Junctions
T. Nussbaumer, P. Lerch, E. Kirk, A. Zehnder, R. Füchslin, P. F. Meier, and H. R. Ott
Phys. Rev. B **61**, 9719-9728 (2000)
- Local Estimates for Entropy Densities in Coupled Map Lattices
E. Olbrich, R. Hegger, and H. Kantz
Phys. Rev. Lett. **84**, 2132-2135 (2000)
- Coarse Grained Dynamical Entropies – Investigation of High-entropic Dynamical Systems
H. Kantz and E. Olbrich
Physica A **280**, 34-48 (2000)
- Chaos or Noise: Difficulties of a Distinction
M. Cencini, M. Falcioni, H. Kantz, E. Olbrich, and A. Vulpiani
Phys. Rev. E **62**, 427-437 (2000)
- Record Breaking Optimization Results – Using the Ruin & Recreate Principle
G. Schrimpf, J. Schneider, H. Stamm-Wilbrandt, and G. Dueck
J. Comp. Phys. **159**, 139-171 (2000)
- The Influence of Trucks on Traffic Flow – An Investigation on the Nagel-Schreckenberg-model
A. Ebersbach, J. Schneider, I. Morgenstern, and R. Hammwöhner
Int. J. Mod. Phys. C **11**, 837-842 (2000)
- Optimization of Production Planning Problems – A Case Study for Assembly Lines
J. Schneider, J. Britze, A. Ebersbach, I. Morgenstern, and M. Puchta
Int. J. Mod. Phys. C **11**, 949-972 (2000)

Articles in press

- Reconstruction of the Parameter Spaces of Dynamical Systems
S. Güttler, H. Kantz, and E. Olbrich
Phys. Rev. E
- Optimization of the Time-dependent Traveling Salesman Problem with Monte Carlo Methods
J. Bentner, G. Bauer, G. M. Obermair, I. Morgenstern, and J. Schneider
Phys. Rev. E

Invited Lectures

- H. R. Moser
"Electroencephalograms in Epilepsy: Complexity Analysis and Seizure Prediction within the Framework of Lyapunov Theory"
Invited talk, The Physics of Low Dimensions, Oaxaca (Mexico), 17.1.2000
- S. Pliberšek
"Changes in the Electronic Structure of La_2CuO_4 induced by Strontium"
APS March Meeting 2000, Minneapolis, 22. 3. 2000
- E. Olbrich
"Characterizing extensive chaos by means of local observations"
Seminarvortrag, Max-Planck-Institut für Mathematik der Naturwissenschaften, Leipzig, 10.5.2000
- J. Schneider
"Modern Optimization Techniques for Spin Glasses"
Seminar talk dedicated to the 100th anniversary of Ernst Ising's birthday, Univ. of Cologne, 15.6.2000
- E. P. Stoll
"Virtual Endoscopy: a new method for the early detection of colon cancer and for defining the size and shape of aortic stents based on a collaboration between medicine, computer science and physics"
Invited talk, IBM Forschungslabor Rüschlikon, 30.8.2000
- J. Schneider
"Methoden der statistischen Physik zur Optimierung von Produktionslinien"
Vorlesung mit Übungen, WE-Heraus-Ferienkurs für Physik, Univ. of Chemnitz (Germany), 2.10.2000
- E. Olbrich
"Das Konzept der dimensionalen Komplexität zur Charakterisierung von EEG's"
Seminarvortrag, Klinik für Epileptologie, Univ. of Bonn, 30.10.2000
- E. Olbrich
"What can be learned from EEG by nonlinear time series analysis?"
Seminarvortrag, Max-Planck-Institut für Physik komplexer Systeme, Dresden, 5.12.2000
- P. F. Meier
"Ab initio Calculations of Hyperfine Properties in Superconductors" Arizona State Univ., Tempe, Arizona, 6. 11. 2000
- P. F. Meier
"New Interpretation of NMR Data on Cuprates"
Third Internat. Conf. on New Theories, Discoveries and Applications of Superconductors, Honolulu, 18. 1. 2001
- P. F. Meier
"New Interpretation of NMR Data on Cuprates"
Workshop on the Phase Diagram of Cuprates, MPI Stuttgart, 5. 1. 2001

16.6 Research group of Prof. J. Osterwalder

Articles

- Electronic structure of K doped C_{60} monolayers on Ag(001)
C. Cepek, M. Sancrotti, T. Greber, J. Osterwalder
Surf. Sci. 454-456 (2000) 467-471
- Angle-resolved photoemission study of clean and hydrogen saturated Mo(110)
J. Kröger, T. Greber, J. Osterwalder
Phys. Rev. B 61 (2000) 14146-14156
- Full hemispherical photoelectron diffraction and Fermi surface mapping
J. Osterwalder, T. Greber, E. Wetli, J. Wider, H.-J. Neff
Prog. Surf. Sci. 64 (2000) 65-87
- Fermi surface contours of p(2x2) O/Mo(110): an angle-resolved photoelectron spectroscopy study
J. Kröger, T. Greber, J. Osterwalder
Surf. Sci. 459 (2000) 173-182
- Step-induced one-dimensional surface state on Cu(332)
F. Baumberger, T. Greber, J. Osterwalder
Phys. Rev. B 62 (2000) 15431-15434
- Doping-dependent electronic structure of cuprates studied using angle-resolved photoemission
P. Schwaller, T. Greber, P. Aebi, J. M. Singer, H. Berger, L. Forro, J. Osterwalder
Europhys. J. B 18 (2000) 215-225
- The photoemission Fermi edge as a sample thermometer
J. Kröger, T. Greber, T. J. Kreutz, J. Osterwalder
J. Electron Spectrosc. Relat. Phenom. 113 (2001) 241-251
- Determining adsorbate structures from substrate emission x-ray photoelectron diffraction
M. Muntwiler, W. Auwärter, F. Baumberger, M. Hoesch, T. Greber, J. Osterwalder
Surf. Sci. 472 (2001) 125-132
- Atomically resolved images from near-node photoelectron holography experiments on Al(111)
J. Wider, F. Baumberger, M. Sambì, R. Gotter, A. Verdini, F. Bruno, D. Cvetko, A. Morgante, T. Greber, J. Osterwalder
Phys. Rev. Lett. 86 (2001) 2337-2340

Articles in press

- Surface states on clean and adsorbate-covered metal surfaces
J. Osterwalder, T. Greber, J. Kröger, J. Wider, H.-J. Neff, F. Baumberger
M. Hoesch, W. Auwärter, R. Fasel, P. Aebi
Proceedings of the *Workshop on Physics in Low Dimensions*, Oaxaca, Mexico, (Plenum Press, 2001)
- Influence of an atomic grating on a magnetic Fermi surface
T. Greber, W. Auwärter, J. Osterwalder
Proceedings of the *Workshop on Physics in Low Dimensions*, Oaxaca, Mexico, (Plenum Press, 2001)

- Electronic and atomic structure of the Cu/Si(111) ‘quasi-5x5’ overlayer
M. De Santis, M. Muntwiler, J. Osterwalder, G. Rossi, F. Sirotti, A. Stuck,
L. Schlapbach
Surf. Sci. (2001)
- Coexisting inequivalent orientations of C₆₀ on Ag(001)
C. Cepek, R. Fasel, M. Sancrotti, T. Greber, J. Osterwalder
Phys. Rev. B (2001)
- Correlation effects and magnetism in 3d transition metals
J. Osterwalder
J. Electron Spectrosc. Relat. Phenom. (2001)
- Temperature-dependent Fermi gap opening in the c(6x2)-C₆₀/Ag(001) two-dimensional superstructure
C. Cepek, I. Vobornik, A. Goldoni, E. Magnano, G. Selvaggi, J. Kröger, G. Panaccione,
G. Rossi, M. Sancrotti
Phys. Rev. Lett. (2001)
- Probing the electronic states of band ferromagnets with photoemission
T. Greber
Invited chapter, Heraeus Workshop on ‘Ground-State and Finite-Temperature Band Ferromagnetism’, Berlin Wandlitz, Springer Verlag (2001)

Diploma and PhD Theses

- C₆₀ interaction with metals and semiconductors
Cinzia Cepek
Ph. D. Thesis, Physik-Institut, Universität Zürich, 2000
- Bau einer Elektronenkanone für zeitaufgelöste Beugung mit langsamen Elektronen
Reto Karrer
Diploma Thesis, Physik-Institut, Universität Zürich, 2000

Conference reports

- Near node photoelectron holography: first proof-of-principle experiments
J. Wider
European Physical Society - Condensed Matter Division Meeting (EPS-CMD-18), Montreux, 13.3.00
- Influence of a single layer insulator on a ferromagnetic substrate: h-BN on Ni(111)
T. Greber
European Physical Society - Condensed Matter Division Meeting (EPS-CMD-18), Montreux, 16.3.00
- Co clusters on h-BN/Ni(111): interface atomic structure analysis with XPD and STM
M. Muntwiler, W. Auwärter, T. Greber, J. Osterwalder (Poster)
European Physical Society - Condensed Matter Division Meeting (EPS-CMD-18), Montreux, 16.3.00
- One-dimensional Shockley surface state resonances on Cu(332)
F. Baumberger, T. Greber, J. Osterwalder (Poster)
European Physical Society - Condensed Matter Division Meeting (EPS-CMD-18), Montreux, 16.3.00

- One- and two-dimensional surface states on vicinal Cu(111)
F. Baumberger
12th Symposium on Surface Science, Kananaskis Village, Canada, 18.3.00
- Fermi-surface contours of H/Mo(110)
J. Kröger
March Meeting of the American Physical Society, Minneapolis, USA, 23.3.00
- Fermi-Flächen von Oberflächenzuständen auf H/Mo(110)
J. Kröger
Frühjahrstagung der Deutschen Physikalischen Gesellschaft, Regensburg, 29.3.00
- One- and two-dimensional surface states on vicinal Cu(111)
F. Baumberger
19th European Conference on Surface Science, Madrid, Spain, 8.9.00
- Co on h-BN/Ni(111): a sharp metal-insulator-metal junction?
W. Auwärter, M. Muntwiler, T. Greber, J. Osterwalder (Poster)
19th European Conference on Surface Science, Madrid, Spain, 8.9.00
- The electronic structure of itinerant ferromagnets: correlation effects and future experiments
J. Osterwalder
Japanese-Swiss Seminar on ‘Spectroscopy of Novel Materials with Highly Brilliant Synchrotron Radiation’, Nikko, Japan, 2.10.00
- A nanometer-sized magnetic tunneling junction: Co/h-BN/Ni(111)
M. Muntwiler (Poster) 4th Hasliberg Workshop on Nanoscience, Hasliberg, 19.10.00
- Status of COPHEE, the COmplete PHotoEmission Experiment
M. Hoesch (Poster) 3rd SLS Workshop on Synchrotron Radiation, Les Diablerets, 19.10.00
- Quantized electrons in ultrathin Ag films on Si(001) surfaces
I. Matsuda (Poster) 3rd SLS Workshop on Synchrotron Radiation, Les Diablerets, 19.10.00
- Photoemission from Bi(111): comparison of synchrotron and home lab studies
M. Hengsberger (Poster, short talk (Poster Prize))
3rd SLS Workshop on Synchrotron Radiation, Les Diablerets, 19.10.00
- Imaging atom sites with near node photoelectron holography
T. Greber (Poster)
3rd SLS Workshop on Synchrotron Radiation, Les Diablerets, 19.10.00
- Partial densities of states measured with polarized x-rays
F. Baumberger (Poster)
3rd SLS Workshop on Synchrotron Radiation, Les Diablerets, 19.10.00

Invited Lectures

- F. Baumberger
One-dimensional Shockley surface state resonances on stepped Cu(111) as measured by photoelectron spectroscopy
Condensed Matter Physics Seminar, Kansas State University, Manhattan, Kansas, USA, 13.3.00

- T. Greber
Exploiting the orientation of the light polarization in x-ray photoelectron spectroscopy (XPS) and diffraction (XPD): From symmetry breaking, s partial densities of states to near node photoelectron holography
Workshop on the 'ALOISA' beamline, Istituto Nazionale della Fisica della Materia, Genova, Italy, 17.4.00
- J. Osterwalder
Electronic states near the Fermi energy in 3d ferromagnets and interfaces
Seminar, Department of Physics, University of Modena, Italy, 25.5.00
- T. Greber
Strukturbestimmung mit winkelgerasterter Photoelektronenbeugung: von der Projektion eines Kristalls bis zur Holographie mit atomarer Auflösung
Festkörperseminar der ETHZ, 25.5.00
- T. Greber
Exploring surface states and magnetic tunneling junctions with photoemission
Seminar de la Matiere Condensee, EPFL, 16.6.00
- J. Osterwalder
High-resolution photoemission study of the discommensurate (5.55x5.55)-Cu:Si(111) surface layer
International Workshop on Electron Spectroscopies and Strongly Correlated Electron Systems, Avila, Spain, 10.7.00
- J. Osterwalder
Surface structure from photoelectron diffraction: fingerprinting, holography and structural refinement
26th IUVESTA Workshop on Surface Holography and Other Direct Methods, Hong Kong, 15.8.00
- M. Hoesch
COPHEE, the COmplete PHotoEmission Experiment
National Synchrotron Light Source Lunchtime Seminar, Brookhaven National Laboratory, Upton, NY, USA, 25.8.00
- M. Hoesch
Photoemission from oriented orbitals
Seminar, Environmental Molecular Sciences Laboratory, Pacific Northwest National Laboratory, Richland, WA, USA, 8.9.00
- J. Osterwalder
Photoelectron diffraction and band structure mapping
Low-Energy Electron Microscopy (LEEM-2) Workshop, Paris, 27.9.00
- J. Osterwalder
The electronic structure of itinerant ferromagnets: correlation effects and future experiments
Seminar, Nara Institute of Science and Technology, Nara, Japan, 5.10.00
- T. Greber
Photoemission around the Fermi level of band ferromagnets
Heraeus Workshop on 'Ground-State and Finite-Temperature Band Ferromagnetism', Berlin Wandlitz, 5.10.00

- T. Greber
Hexagonal boron nitride on nickel (111): a spin-selective tunneling junction?
Lunch Seminar, Technische Chemie, Technische Universität Wien, 9.10.00
- T. Greber
Experiments at ELETTRA: from near node photoelectron holography to Fermi surfaces
in three dimensions
3rd SLS Workshop on Synchrotron Radiation, Les Diablerets, 17.10.00
- T. Greber
Photoelektronenbeugung: Holographie mit atomarer Auflösung
Physik-Kolloquium, Universität Marburg, 3.11.00
- T. Greber
Untersuchung der Grenzfläche zwischen einem Bandferromagneten und einem Isolator
Physik-Kolloquium, Universität Düsseldorf, 9.11.00
- J. Osterwalder
Valence band photoemission and Fermi surface mapping
6 hours of Lecture, School on Synchrotron Radiation, ICTP Trieste, Italy,
29.11.00 - 4.12.00
- T. Greber
Untersuchung von Oberflächenzuständen und einer magnetischen Tunnelbarriere mit
winkelaufgelöster Photoemission
Physik-Seminar, Technische Universität München, 26.1.01

16.7 Research group of Prof. U. Straumann (for H1 publications see group of Prof. P. Truöl, Sec. 16.8)

Articles

- Measurement of CP-Violating Asymmetries in B0 Decays to CP Eigenstates
B. Aubert et al. (BABAR Collaboration) , Phys. Rev. Lett. 86 (2001), 2515
- Hoffnung für die Gravitationskonstante
St. Schramminger
Physikalische Blätter **56** (2000) Nr. 9 pp. 15-16 .

LHCb notes

- A triple GEM detector with two-dimensional readout
M. Ziegler, P. Sievers and U. Straumann
hep-ex/0007007 and LHCb internal note LHCb-2000-056, July 2000
- LHCb Calorimeter, technical design report
The LHCb Collaboration
CERN/LHCC/2000-036, Sep. 6, 2000
- LHCb RICH, technical design report
The LHCb Collaboration
CERN/LHCC/2000-037, Sep. 7, 2000
- A Possible Layout of an Inner Tracker Silicon Detector
O. Steinkamp
LHCb-2000-109, November 2000

- Space Requirements and z Positions for Tracking Stations
O. Steinkamp
LHCb-2000-108, November 2000

Conference reports

- R. Bernet, B. Aubert *et al.*
14 contributed papers to the BABAR conference, July 2000.
SLAC-PUB-8526...SLAC-PUB-8540 (BABAR-CONF-00-01...BABAR-CONF-00-16)
- A triple GEM detector with two-dimensional readout
M. Ziegler, P. Sievers and U. Straumann
Proceedings of the International Conference on Imaging Techniques in the borderlands of High Energy Physics, Astrophysics, Nuclear Physics, Medicine and Biology (Imaging 2000), 28 June - 1 July 2000, Stockholm, submitted to Nucl. Instr. and Meth.
- First Level Trigger for H1, using the latest FPGA generation
M. Urban, J. Becker, A. Rausch and U. Straumann
Proceedings of the 6th Workshop on Electronics for LHC Experiments 11-15 September 2000, Cracow, Poland.
- Determination of the Gravitational Constant Using a Beam Balance
St. Schlamminger, E. Holzschuh, W. Kündig
Conference Digest, Conference on Precision Electromagnetic Measurements 2000, Sydney, May 14 - 19, 2000, pp. 693-694 .
- Determination of the Gravitational Constant Using a Beam Balance
St. Schlamminger, E. Holzschuh, W. Kündig
to be published in the Conference Proceedings of the 9th Marcel Grossmann Meeting, Rome, July 3 - 7 2000.

Invited Lectures

- Inner Tracking of LHCb
U. Straumann, Seminarvortrag, DESY, 15. März 2000
- LHCb tracking system
O. Steinkamp,
International symposium "LHC physics and detectors"
JINR, Dubna, Russian Federation, June 28-30, 2000
- Determination of the Gravitational Constant Using a Beam Balance
St. Schlamminger, E. Holzschuh, W. Kündig
Seminar, Physik Institut, Universität Konstanz, June 16th 2000.
- Neuere Bestimmungen der Gravitationskonstanten
St. Schlamminger
Physikalisches Kolloquium, Fachbereich Physik, Universität Kaiserslautern, January 29th 2001.

Diploma and PhD Theses

- Entwurf und Bau einer Frontend-Steuerung für das CIP-Upgrade Projekt für H1 bei HERA
Achim Vollhardt
Diplomarbeit, Heidelberg und Zürich, Januar 2001

- The Data Acquisition and Control System for a Fast Trigger at H1
Jan Becker
Diplomarbeit, Heidelberg und Zürich, November 2000
- Ein schneller Trigger für H1 bei HERA
Max Urban
Diplomarbeit, Heidelberg und Zürich, Mai 2000.

16.8 Research group of Prof. P. Truöl (incl. H1 publications of group Prof. U. Straumann)

Articles

- Di-jet Event Rates in Deep-Inelastic Scattering at HERA
H1-Collaboration**, C. Adloff *et al.*
DESY 98 – 076
The European Physical Journal **C13** (2000), 415 - 426
- Measurement of Dijet Cross Sections in Low Q^2 and the Extraction of an Effective Parton Density for the Virtual Photon
H1-Collaboration**, C. Adloff *et al.*
DESY 98 – 205
The European Physical Journal **C13** (2000), 397 -414
- $K^+ \rightarrow \pi^+ \mu^- \mu^+$ in E865 at BNL
E865 Collaboration†, Julia A. Thompson *et al.*
hep-ex 9904026
Proc. 17th Int. Workshop on Weak Interactions and Neutrinos (WIN 99), Cape Town, South Africa (January 1999), eds. A. Dominguez, R.D. Viollier (World Scientific, Singapore 2000), p. 540 - 544.
- Elastic Electroproduction of ρ Mesons at HERA
H1-Collaboration**, C. Adloff *et al.*
DESY 99 – 10
The European Physical Journal **C13** (2000), 371 - 396
- Measurement of Neutral and Charged Current Cross Sections in Positron-Proton Collisions at Large Momentum Transfer
H1-Collaboration**, C. Adloff *et al.*
DESY 99 – 107, hep-ex 9908059
The European Physical Journal **C13** (2000), 609 - 639
- A New Measurement of the Rare Decay $K^+ \rightarrow \pi^+ \mu^+ \mu^-$
E865-Collaboration†, H. Ma *et al.*
hep-ex 9910047
Physical Review Letters **84** (2000), 2580 - 2583
- Investigation of Power Corrections Event Shape Variables Measured in Deep-Inelastic Scattering
H1-Collaboration**, C. Adloff *et al.*
DESY 99 – 193, hep-ex 9912052
The European Physical Journal **C14** (2000), 255 - 269; addendum ibidem **C18** (2000), 417 - 419.

- The H1 Silicon Vertex Detector
D. Pitzl, O. Behnke, M. Biddulph, K. Bösiger, R. Eichler, W. Erdmann, K. Gabathuler, J. Gassner, W.J. Haynes, R. Horisberger, M. Kausch, M. Lindström, H. Niggli, G. Noyes, P. Pollet, S. Steiner, S. Streuli, K. Szeker, and P. Truöl
hep-ex 0002044
Nuclear Instruments and Methods in Physics Research **A454** (2000), 334 - 349.
- Search for Compositeness, Leptoquarks and Large Extra Dimensions in eq Contact Interactions at HERA
H1-Collaboration**, C. Adloff *et al.*
DESY 00 – 027, hep-ex 0003002
Physics Letters **B479** (2000), 358 - 370
- Measurement of Di-jet Cross Sections in Photoproduction and Photon Structure
H1-Collaboration**, C. Adloff *et al.*
DESY 00 – 035, hep-ex 0003011
Physics Letters **B483** (2000), 36 - 48
- Elastic Photoproduction of J/Ψ - and Y -Mesons at HERA
H1-Collaboration**, C. Adloff *et al.*
DESY 00 – 037, hep-ex 0003020
Physics Letters **B483** (2000), 23 - 35
- Elastic Φ -Meson Production at HERA
H1-Collaboration**, C. Adloff *et al.*
DESY 00 – 070, hep-ex 0005010
Physics Letters **B483** (2000), 360 - 372
- An Improved Limit on the Rate of the Decay $K^+ \rightarrow \pi^+ \mu^+ e^-$
E865-Collaboration[†], R. Appel *et al.*
hep-ex 0005016
Physical Review Letters **85** (2000), 2450 - 2453
- Search for Lepton Flavor Violation in K^+ Decays into a Charged Pion and Two Leptons
E865-Collaboration[†], R. Appel *et al.*
hep-ex 0006003
Physical Review Letters **85** (2000), 2877 - 2880.
- Inclusive Photoproduction of Neutral Pions in the Photon Hemisphere at HERA
H1-Collaboration**, C. Adloff *et al.*
DESY 00 – 085, hep-ex 0006017
The European Physical Journal **C18** (2000), 293 - 302.
- A Search for Excited Fermions at HERA
H1-Collaboration**, C. Adloff *et al.*
DESY 00 – 102, hep-ex 0007035
The European Physical Journal **C17** (2000), 567 - 581

Articles in Print

- Di-jet Production in Charged and Neutral Current ep Interactions at High Q^2
H1-Collaboration**, C. Adloff *et al.*
DESY 00 – 143, hep-ex 0010016
The European Physical Journal **C** (2001), in print.

- Measurement and QCD Analysis of Jet Cross Sections in Deep-Inelastic Positron-Proton Collisions at \sqrt{s} of 300 GeV
H1-Collaboration**, C. Adloff *et al.*
DESY 00 – 145, hep-ex 0010054
The European Physical Journal **C** (2001), in print.
- Diffractive Jet-Production in Deep-Inelastic e^+p Collisions at HERA
H1-Collaboration**, C. Adloff *et al.*
DESY 00 – 174, hep-ex 0012051
The European Physical Journal **C** (2001), in print.
- Deep-Inelastic Inclusive ep Scattering at Low x and a Measurement of α_s
H1-Collaboration**, C. Adloff *et al.*
DESY 00 – 181, hep-ex 0012053
submitted to The European Physical Journal **C**
- Measurements of Neutral and Charged Current Cross Sections in Electron-proton Collisions at High Q^2 at HERA
H1-Collaboration**, C. Adloff *et al.*
DESY 00 – 187, hep-ex 0012052
The European Physical Journal **C** (2001), in print.
- A Large Acceptance, High Resolution Detector for Rare K^+ -decay Experiments
E865-Collaboration[†], R. Appel *et al.*
Nuclear Instruments and Methods in Physics Research (2001), in print.
- Searches at HERA for Squarks in R-Parity Violating Supersymmetry
H1-Collaboration**, C. Adloff *et al.*
DESY 01 – 021, hep-ex 0102050
submitted to The European Physical Journal **C** (2001)
- Open Charm and Beauty Production at HERA
F. Sefkow
Proc. 30th International Conference on High Energy Physics (ICHEP 2000), Osaka, Japan, July 2000
hep-ex 0011034
- New Results on Rare and Forbidden Semileptonic K^+ Decays
P. Truöl
HQ2K, 5th International Workshop on Heavy Quarks at Fixed Target, Centro Brasileiro de Pesquisas Fisicas, Rio de Janeiro, Brazil, October 2000
hep-ex 0012012
Proc. ed. A. Reis, Frascati Physics Series (2001)

Conference reports

- Test der Quantenchromodynamik in inklusiver ep -Streuung mit dem H1 Detektor
R. Wallny
DPG Frühjahrstagung 2000 - Teilchenphysik, Dresden, Germany, March 21 - 24, 2000
- Messung von Beauty-Produktion bei HERA mit dem H1-Vertexdetektor
J. Kroseberg
DPG Frühjahrstagung 2000 - Teilchenphysik, Dresden, Germany, March 21 - 24, 2000
- Messung von Beauty-Produktion bei HERA
J. Kroseberg
DPG Frühjahrstagung 2001 - Teilchenphysik, Bonn, 26. - 29. März 2001

Invited Lectures

- Open Charm and Beauty Production at HERA
F. Sefkow
30th International Conference on High Energy Physics (ICHEP 2000), Osaka, Japan, July 2000
- New Results on Rare and Forbidden Semileptonic K^+ Decays
P. Truöl
HQ2K, 5th International Workshop on Heavy Quarks at Fixed Target, Centro Brasileiro de Pesquisas Fisicas, Rio de Janeiro, Brazil, October 2000

Diploma and PhD Theses

- A Measurement of Diffractive Charm Production at HERA
Stefan Hengstmann
Dissertation, Physik-Institut, Universität Zürich, December 2000
- Contributions to the Development of Microstrip Gas Chambers (MSGC) for the HERA-*B* Experiment
Thomas Walter
Dissertation, Physik-Institut, Universität Zürich, February 2001

† E865-collaboration:

R. Appel^{8,6}, G.S. Atoyan^{2,8}, B. Bassaleck⁵, D.N. Brown⁶, D.R. Bergman⁸, N. Cheung⁶, S. Dhawan⁸, H. Do⁸, J. Egger³, S. Eilerts⁵, C. Felder^{1,6}, H. Fischer⁵, M. Gach⁶, W.D. Herold³, V.V. Isakov^{2,8}, H. Kaspar³, D. Kraus⁶, D. Lazarus¹, L. Leipuner¹, J. Lowe⁵, J. Lozano⁸, H. Ma¹, W. Majid⁸, W. Menzel⁴, S. Pislak^{7,8}, A.A. Poblaguev^{2,8}, A.L. Proskurjakow², P. Rehak¹, P. Robmann⁷, A. Sher⁷, A. Sher⁶, R. Stotzer⁵, J.A. Thompson⁶, P. Truöl^{7,8}, H. Weyer^{4,3}, M.E. Zeller⁸

³ Paul Scherrer Institut, Villigen

⁷ Physik-Institut der Universität Zürich, Zürich

** H1-collaboration (status of February 2001, the actual author list may differ from paper to paper somewhat):

C. Adloff³³, V. Andreev²⁴, B. Andrieu²⁷, T. Anthonis⁴, V. Arkadov³⁵, A. Astvatsatourov³⁵, A. Babaev²³, J. Bähr³⁵, P. Baranov²⁴, E. Barrelet²⁸, W. Bartel¹⁰, P. Bate²¹, A. Beglarian³⁴, O. Behnke¹³, C. Beier¹⁴, A. Belousov²⁴, T. Benisch¹⁰, Ch. Berger¹, T. Berndt¹⁴, J.C. Bizot²⁶, V. Boudry²⁷, W. Braunschweig¹, V. Brisson²⁶, H.-B. Bröker², D.P. Brown¹¹, W. Brückner¹², D. Bruncko¹⁶, J. Bürger¹⁰, F.W. Büsler¹¹, A. Bunyatyan^{12,34}, A. Burrage¹⁸, G. Buschhorn²⁵, A.J. Campbell¹⁰, J. Cao²⁶, T. Carli²⁵, S. Caron¹, D. Clarke⁵, B. Clerbaux⁴, C. Collard⁴, J.G. Contreras^{7,41}, Y.R. Coppens³, J.A. Coughlan⁵, M.-C. Cousinou²², B.E. Cox²¹, G. Cozzika⁹, J. Cvach²⁹, J.B. Dainton¹⁸, W.D. Dau¹⁵, K. Daum^{33,39}, M. Davidsson²⁰, B. Delcourt²⁶, N. Delerue²², R. Demirchyan³⁴, A. De Roeck^{10,43}, E.A. De Wolf⁴, C. Diaconu²², J. Dingfelder¹³, P. Dixon¹⁹, V. Dodonov¹², J.D. Dowell³, A. Drutskoi²³, A. Dubak²⁵, C. Duprel², G. Eckerlin¹⁰, D. Eckstein³⁵, V. Efremenko²³, S. Egli³², R. Eichler³⁶, F. Eisele¹³, E. Eisenhandler¹⁹, M. Ellerbrock¹³, E. Elsen¹⁰, M. Erdmann^{10,40,e}, W. Erdmann³⁶, P.J.W. Faulkner³, L. Favart⁴, A. Fedotov²³, R. Felst¹⁰, J. Ferencei¹⁰, S. Ferron²⁷, M. Fleischer¹⁰, Y.H. Fleming³, G. Flügge², A. Fomenko²⁴, I. Foresti³⁷, J. Formánek³⁰, J.M. Foster²¹, G. Franke¹⁰, E. Gabathuler¹⁸, K. Gabathuler³², J. Garvey³, J. Gassner³², J. Gayler¹⁰, R. Gerhards¹⁰, C. Gerlich¹³, S. Ghazaryan^{4,34}, L. Goerlich⁶, N. Gogitidze²⁴, M. Goldberg²⁸, C. Goodwin³, C. Grab³⁶, H. Grässler², T. Greenshaw¹⁸, G. Grindhammer²⁵, T. Hadig¹³, D. Haidt¹⁰, L. Hajduk⁶, W.J. Haynes⁵, B. Heinemann¹⁸, G. Heinzelmann¹¹, R.C.W. Henderson¹⁷, S. Hengstmann³⁷, H. Henschel³⁵, R. Heremans⁴, G. Herrera^{7,41}, I. Herynek²⁹, M. Hildebrandt³⁷, M. Hilgers³⁶, K.H. Hiller³⁵, J. Hladký²⁹, P. Höting², D. Hoffmann²², R. Horisberger³², S. Hurling¹⁰,

M. Ibbotson²¹, Ç. İşsever⁷, M. Jacquet²⁶, M. Jaffre²⁶, L. Janauschek²⁵, D.M. Jansen¹², X. Janssen⁴, V. Jemanov¹¹, L. Jönsson²⁰, D.P. Johnson⁴, M.A.S. Jones¹⁸, H. Jung^{20,10}, H.K. Kästli³⁶, D. Kant¹⁹, M. Kapichine⁸, M. Karlsson²⁰, O. Karschnick¹¹, F. Keil¹⁴, N. Keller³⁷, J. Kennedy¹⁸, I.R. Kenyon³, S. Kermiche²², C. Kiesling²⁵, P. Kjellberg²⁰, M. Klein³⁵, C. Kleinwort¹⁰, T. Kluge¹, G. Knies¹⁰, B. Koblitz²⁵, S.D. Kolya²¹, V. Korbel¹⁰, P. Kostka³⁵, S.K. Kotelnikov²⁴, R. Koutouev¹², A. Koutov⁸, H. Krehbiel¹⁰, J. Kroseberg³⁷, K. Krüger¹⁰, A. Küpper³³, T. Kuhr¹¹, T. Kurča^{25,16}, R. Lahmann¹⁰, D. Lamb³, M.P.J. Landon¹⁹, W. Lange³⁵, T. Laštovička³⁵, P. Laycock¹⁸, E. Lebailly²⁶, A. Lebedev²⁴, B. Leißner¹, R. Lemrani¹⁰, V. Lendermann⁷, S. Levonian¹⁰, M. Lindstroem²⁰, B. List³⁶, E. Lobodzinska^{10,6}, B. Lobodzinski^{6,10}, A. Loginov²³, N. Loktionova²⁴, V. Lubimov²³, S. Lüders³⁶, D. Lüke^{7,10}, L. Lytkin¹², N. Magnussen³³, H. Mahlke-Krüger¹⁰, N. Malden²¹, E. Malinovski²⁴, I. Malinovski²⁴, R. Maraček²⁵, P. Marage⁴, J. Marks¹³, R. Marshall²¹, H.-U. Martyn¹, J. Martyniak⁶, S.J. Maxfield¹⁸, D. Meer³⁶, A. Mehta¹⁸, K. Meier¹⁴, P. Merkel¹⁰, A.B. Meyer¹¹, H. Meyer³³, J. Meyer¹⁰, P.-O. Meyer², S. Mikocki⁶, D. Milstead¹⁸, T. Mkrtchyan³⁴, R. Mohr²⁵, S. Mohrdieck¹¹, M.N. Mondragon⁷, F. Moreau²⁷, A. Morozov⁸, J.V. Morris⁵, K. Müller³⁷, P. Murin^{16,42}, V. Nagovizin²³, B. Naroska¹¹, J. Naumann⁷, Th. Naumann³⁵, G. Nellen²⁵, P.R. Newman³, T.C. Nicholls⁵, F. Niebergall¹¹, C. Niebuhr¹⁰, O. Nix¹⁴, G. Nowak⁶, J.E. Olsson¹⁰, D. Ozerov²³, V. Panassik⁸, C. Pascaud²⁶, G.D. Patel¹⁸, M. Peez²², E. Perez⁹, J.P. Phillips¹⁸, D. Pitzl¹⁰, R. Pöschl²⁶, I. Potachnikova¹², B. Povh¹², K. Rabbertz¹, G. Rädcl²⁷, J. Rauschenberger¹¹, P. Reimer²⁹, B. Reisert²⁵, D. Reyna¹⁰, S. Riess¹¹, C. Risler²⁵, E. Rizvi³, P. Robmann³⁷, R. Roosen⁴, A. Rostovtsev²³, C. Royon⁹, S. Rusakov²⁴, K. Rybicki⁶, D.P.C. Sankey⁵, J. Scheins¹, F.-P. Schilling¹³, P. Schleper¹⁰, D. Schmidt³³, D. Schmidt¹⁰, S. Schmitt¹⁰, M. Schneider²², L. Schoeffel⁹, A. Schöning³⁶, T. Schörner²⁵, V. Schröder¹⁰, H.-C. Schultz-Coulon⁷, C. Schwanenberger¹⁰, K. Sedlák²⁹, F. Sefkow³⁷, V. Shekelyan²⁵, I. Sheviakov²⁴, L.N. Shtarkov²⁴, Y. Sirois²⁷, T. Sloan¹⁷, P. Smirnov²⁴, V. Solochenko^{23,†}, Y. Soloviev²⁴, D. South²¹, V. Spaskov⁸, A. Specka²⁷, H. Spitzer¹¹, R. Stamen⁷, B. Stella³¹, J. Stiewe¹⁴, U. Straumann³⁷, M. Swart¹⁴, M. Taševský²⁹, V. Tchernyshov²³, S. Tchetchelnitski²³, G. Thompson¹⁹, P.D. Thompson³, N. Tobien¹⁰, D. Traynor¹⁹, P. Trüöl³⁷, G. Tsipolitis^{10,38}, I. Tsurin³⁵, J. Turnau⁶, J.E. Turney¹⁹, E. Tzamariudaki²⁵, S. Udluft²⁵, A. Usik²⁴, S. Valkár³⁰, A. Valkárová³⁰, C. Vallée²², P. Van Mechelen⁴, S. Vassiliev⁸, Y. Vazdik²⁴, A. Vichnevski⁸, K. Wacker⁷, R. Wallny³⁷, B. Waugh²¹, G. Weber¹¹, M. Weber¹⁴, D. Wegener⁷, M. Werner¹³, N. Werner³⁷, G. White¹⁷, S. Wiesand³³, T. Wilksen¹⁰, M. Winde³⁵, G.-G. Winter¹⁰, Ch. Wissing⁷, M. Wobisch², H. Wollatz¹⁰, E. Wünsch¹⁰, A.C. Wyatt²¹, J. Žáček³⁰, J. Zálesák³⁰, Z. Zhang²⁶, A. Zhokin²³, F. Zomer²⁶, J. Zsembery⁹, and M. zur Nedden¹⁰

³² Paul Scherrer Institut, Villigen

³⁶ Institut für Teilchenphysik, ETH, Zürich

³⁷ Physik-Institut der Universität Zürich, Zürich